DEFOREMATION AND DISLOCATION TEM IMAGE SIMULATION IN $L1_0$-FEPD

by

Amal A. Al Ghaferi

BE, United Arab Emirates University, 2000

Submitted to the Graduate Faculty of

School of Engineering in partial fulfillment

of the requirements for the degree of

Doctor of Philosophy

University of Pittsburgh

2006

UNIVERSITY OF PITTSBURGH

SCHOOL OF ENGINEERING

This dissertation was presented

by

Amal A. Al Ghaferi

It was defended on

December, 4 , 2006

and approved by

Dr. John A. Barnard, Professor, Department of Mechanical Engineering and Materials Science

Anthony J. DeArdo, Professor, Department of Mechanical Engineering and Materials Science

Ian Nettleship, Associate Professor, Department of Mechanical Engineering and Materials Science

Jean R. Blachère, Associate Professor Emeritus, Department of Mechanical Engineering and Materials Science

Dr. J.M.K. Wiezorek, Associate Professor , Department of Mechanical Engineering and Materials Science, Dissertation Director

DEFORMATION AND DISLOCATIONS TEM IMAGES SIMULATION OF $L1_0$ FEPD

Amal A. Al Ghaferi, PhD

University of Pittsburgh, 2006

A yield strength anomaly has been observed in intermetallic $L1_0$-ordered FePd alloys between about 300-700K. However, previous work did not provide clear explanations regarding the microstructural or mechanistic origins for this observation. FePd and γ-TiAl have the same crystal sturtucre. YSA was studied intensively in γ-TiAl system and its origin was related for the dislocation fine structure. In TiAl, the dissociation of the superdislocation [10-1] play an important role in the YSA phenomena and the existence of Yoo torque promote dissociated shockly partial to cross slip to another slip plane. This forms KW lock which is the reason of YSA in TiAl.

The Elastic Constants of the tetragonal $L1_0$ phases describe the intrinsic elastic properties of the $L1_0$-FePd .Details of the dislocations fine structure, such as the details of dissociations and decompositions of dislocations and the relevant planar fault energies, are determined by the elastic constants , including the elastic interactions between partials dislocations and the effect of the Yoo torque. The elastic constants are required for the computer image simulations of WBDF TEM images of narrowly dissociated dislocation configurations. Elastic constants were calculated for FePd and were compared to Elastic constants of γ-TiAl and FePt.

Dislocations TEM Image Simulation will provide contrast guidance for experimental studies in both FePd and FePt. Experimental TEM studies of the fine structure require extensive tilting of the thin crystal section within the magnetic field of the objective lens of the TEM

instrument and are difficult to perform for the hard ferromagnetic FePd and FePt intermetallics since magnetic effects of the sample material on the electrons used for imaging lead to complicated artifacts in images upon tilting through significant angles. Hence, image simulations may assist in identifying appropriate imaging conditions under which significant and relevant differences in the dislocation image contrast may be expected for the dislocations in the two different intermetallics.

This study builds the fundamental basic in the research of the origin of the YSA in FePd. Although the origin of YSA in $L1_0$ FePd has not been identified but the basic intrinsic elastic properties, i.e. elastic constants, has been measured experimentally for the fist time and these elastic constants were used in dislocations TEM image simulation .

TABLE OF CONTENTS

LIST OF TABLES

LIST OF FIGURES

PREFACE

First and foremost thanks to Allah, the creator of all things, for giving me the strength and ability to conduct this study.

I would like to acknowledge, with sincere gratitude, the roles played by those persons who assisted in making this dissertation a worthwhile experience. My profound thanks and appreciation to my academic advisor Professor J.M.K Wiezorek for his patience, guidance, excellent and efficient supervision, valuable advice, suggestions, and encouragement.

I would like also to express my gratitude to the other committee members for their beneficial criticism and valuable suggestions. Great thanks are due to Dr. John A. Barnard for his valuable comments and suggestions. A special thank you also goes to Dr.Jean R. Blachère for his willingness to help anytime and to answer any question. Dr. Ian Nettleship will be always remembered for his helpful comments and great suggestions. Other special thanks are due to Dr. Anthony J. DeArdo for his help and support with work on this dissertation and during my graduate studies.

I would like to express my gratitude to my employer, United Arab Emirates University (UAEU), for sponsoring my graduate studies. Also I would like to thank Janine Carlock for her editing assistance.

Special thanks go to my friends in Pittsburgh for their care, support and help during my PhD studies.

My deepest regards to my parents for their continuous sacrifices, for their loving guidance, and for teaching me the importance of education and encouraging me to continue my education in the USA far away from my homeland UAE. Great thanks my brother Dr. Hamad and my sister Muna for their love, support, encouragement and readiness to help. All the love to my nieces Lateefa, Noura , Al Maha and Al Reem and to my nephews Mohammed and Abdulla.

1.0 INTRODUCTION

Some intermetallics offer combinations of properties that render them of interest for applications in aerospace, ground transport systems and information technology devices. For example, ferromagnetic FePd, FePt, CoPt and MnAl exhibit very large magnetocrystalline anisotropy. This qualifies them as candidate materials for magnetic data storage devices and other permanent magnet applications. Other binary intermetallic phases such as Ni_3Al, NiAl and TiAl, exhibit interesting mechanical properties at high temperature and reasonable oxidation resistance. Hence, intermetallic phases and alloys based on them are of technological relevance for power generation and conversion applications. The properties of intermetallics are usually directly related to their chemically ordered crystal structures. The ordered arrangements of the constituent atoms in the crystal lattices affect intrinsic properties such as point defect and dislocation behavior and thereby also influence engineering performance. Hence, apart from their tangible technological relevance, intermetallics also offer opportunities for basic scientific study.Binary intermetallics of the type A_mB_n (where m and n are integers) are stable near the relevant stoichiometric compositions.. Often a critical transition temperature, T_c, exists in the solid state between ordered and disordered phases. Ordering usually lower symmetry of the order phase than the symmetery disordered phase. Strong interatomic bonds between the two elemental constituents of these materials result in their attractive high temperature properties but have also been associated with their most undesirable property, which is their brittleness at low

temperature. TiAl is one intermetallic that exhibit the ordered tetragonal $L1_0$ structure. It has been studied over the past two decades because, with its low density and interesting mechanical and reasonable oxidation properties at elevated temperatures, it is attractive for applications in heat engines. The attractive elevated temperature mechanical strength of TiAl-based intermetallics is associated with a so-called yield strength anomaly (YSA), an increase or retention of the yield stress with increasing temperature between 20˚C to about 700-800˚C.

Other intermetallics with the $L1_0$ structure include the archetypical CuAu-I, CoPt, FePt and FePd. While the last three are of technological interest essentially because of their magnetic properties, some mechanical property investigations have also been performed for CuAu, FePt and FePd. The $L1_0$-ordered CuAu-I and FePt do not show an anomalous increase in yield stress with temperature. However, for the FePd system, an anomalous increase in yield stress with temperature has been reported[1]-[2]. Hence, it appears that some of the $L1_0$-intermetallics exhibit a yield strength anomaly (YSA), while others do not.

More research is needed to investigate the yield strength in the FePd system in order to elucidate the origin(s) of the reported YSA and to compare it with the YSA and its origins in the isostructural TiAl system. In order to develop the understanding of the YSA origins in FePd , it is required to grow $L1_0$-FePd alloys with controlled microstructures . A controlled plastic deformation test should be performed to these alloys at room temperature and high temperature. After the deformation tests intensive TEM study should be held for the deformed FePd samples. Dislocations find structure will be determined by the TEM study and this will results in the details of the dislocations fine structure at different temperatures. At this point the researcher should be able to compare and contrast the dislocations fine structure at room temperature with the dislocations fine structure at high temperature. Image simulation software should be used to

establish dislocations contrast guide for the different type of dislocation in FePd. Comparing the dislocations TEM images with the dislocations simulated images will result in finding the stacking faults energies of different stacking faults in FePd system. This study was able to establish the basis of the research of YSA in FePd, It determines the elastic constants of FePd which were not determined experimentally before. These elastic constants are important input parameters in images simulation software. This study used Cu-Four image simulation software to simulate different types of dislocations in FePd system. A dislocations contrast guide was established for different type of dislocation in FePd system.

2.0 BACKGROUND

2.1 YIELD STRESS ANOMALIES

A yield stress anomaly (YSA) is a phenomenon associated with the observation of an anomalous increase or retention (plateau) of the yield stress with increasing temperature in an intermediate temperature range3. Typical ductile metals that deform by dislocation glide at lower to intermediate temperatures at typical strain rates show a monotonic decrease of the yield stress with increasing temperature, which is the normal yield stress behavior. YSA's are observed in ordered intermetallics alloys4, disordered solid solution alloys, e.g. Cu(Al) 5, in some steels 6 and in pure metals like beryllium, titanium and zirconium.7 YSA's are considered important because they help to maintain good mechanical properties, e.g. resistance to plastic deformation, at high temperature. The plasticity of metallic materials is typically accomplished by dislocation motion, and a YSA is usually linked to details of the dislocation properties and their glide behavior, which can be studied by TEM.

It is difficult to identify a general reason for a YSA because the multitude of systems that exhibit them require a range of possible and differing explanations. The following remarks will illustrate this point:

- YSA's do not specifically involve only the properties and behavior of superdislocations in ordered intermetallics. YSA's are indeed observed in disordered alloys like Cu(Al), and in steel and pure metals like beryllium, titanium and zirconium in prismatic slip. Also, YSA's are found in intermetallics, in which only ordinary dislocations are activated, e.g CoTi. [8]
- YSA's are observed in some intermetallics on slip systems involving ordinary dislocations and superdislocation, e.g. TiAl and β-CuZn. For example, in β-CuZn, deformation experiments in pure shear have shown that YSA's in <111>{112} and <111> {110} slip systems involving <111> superdislocations and <100>{010} slip systems involving <100> ordinary dislocations are active in the same temperature range.
- YSA's can be observed in the case where the same superdislocations are gliding in different planes, e.g. in β-CuZn <111> superdislocations in {112} and {110} planes, and in Ni_3Al <110> superdislocation in {111} and {001}[9].
- YSA's have been related also to phase transitions in some cases, e.g., in Cu_3Au, where the yield stress increases up to the order-disordered transition temperature and then sharply decreases[10].

Hence it is clear that there is no simple unified mechanism to provide a possible common interpretation of the YSA. Much of the previous research studied the YSA in $L1_2$ systems, of which Ni_3Al is the most prevalent, presumably because of the important role of the $L1_2$-ordered Ni_3Al based gamma'-phases for the excellent high-temperature mechanical properties of the commercially relevant Ni-base superalloys[11]. The following section will describe the current understanding of the YSA in the L12 ordered intermetallic systems.

2.1.1 YSA in $L1_2$ System

2.1.1.1 Ni_3Al

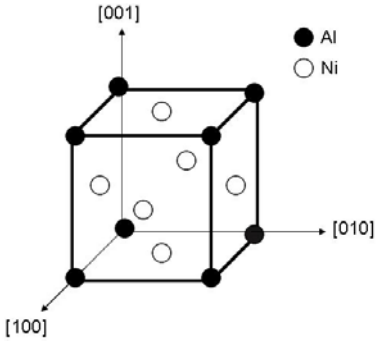

Figure 1: $L1_2$ Structure of Ni_3Al

Figure 1 shows the atomic arrangement of the $L1_2$ structure with an A_3B composition. The similarity to the FCC metals is clear from this unit cell depiction. In the intermetallic $L1_2$ superlattice compounds, slip occurs on both {111} and {001} planes. Based on a hard sphere model and geometrical considerations, three possible planar faults on {111} have been considered in the literature. These are the antiphase boundary (APB), superlattice intrinsic stacking fault (SISF), and complex stacking fault (CSF).

In Ni_3Al, the plastic deformation is governed by gliding superdislocations. These superdislocations can dissociate into various superpartials based on relative energies of the possible planar faults[12]. The dislocation dissociation schemes observed on {111} planes in Ni_3Al are of the APB type, e.g for (111) and a superdislocation with Burgers vector b=[-101]:

$$[-101] \Rightarrow \tfrac{1}{2}[-101] + \text{APB} + \tfrac{1}{2}[-101] \quad \text{(a)}$$

$$\Rightarrow \tfrac{1}{6}[-1-12] + \text{CSF} + \tfrac{1}{6}[-211] + \text{APB} + \tfrac{1}{6}[-1-12] + \text{CSF} + \tfrac{1}{6}[-211] \quad \text{(b)}$$

In Ni_3Al superdislocations are usually dissociated according to scheme (a) at ambient temperature, while scheme (b) has been observed in Ni_3Al deformed at elevated temperature.

On {111}, superdislocations are not stable and have a tendency to cross slip onto {100} planes at temperatures above 70K. The dislocation dissociation on {100} is of the APB type, e.g. for (010):

$$[-101] \Rightarrow \tfrac{1}{2}[-101] + \text{APB} + \tfrac{1}{2}[-101] \quad \text{(c)}$$

Paidar et al[13] proposed a dislocation model using computer simulations to describe possible origins for the YSA in Ni_3Al. Their theoretical work showed that for the {111} planes, screw type superdislocations that dissociate into superpartials according to scheme (a) have planar cores and are always glissile. For the {100} planes, screw type superdislocations that dissociate according to equation (c) have nonplanar cores and become sessile. This prediction of dislocation core structures in Ni_3Al has been confirmed by Crimp[14], Sun and Hazzledine[15] using high resolution transmission electron microscopy (HRTEM) experiments.

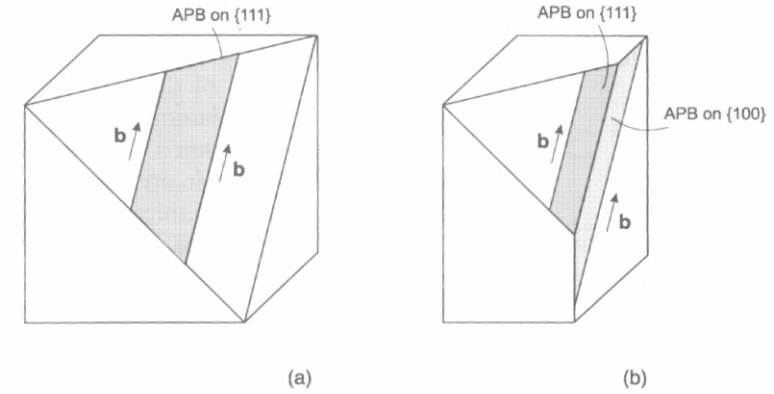

Figure 2: Schematic drawing of a) Screw superpartial pair with APB on a {111} plane. b) Cross slip onto a {100} plane, starting the formation of Kear-Wilsdorf lock.

Ni_3Al shows a strong YSA, reportedly starting at a temperature as low as 70K[16]. Above this temperature, the yield strength (σ_y) increases with increasing temperature until a peak is reached, followed by a (σ_y) decrease with further increases in temperature. Both the peak strength temperature and its magnitude depend on crystal orientation and the sense of applied stresses (either tension or compression). The instability of <101> screw superdislocations on {111} is considered to be the reason for the YSA behavior[13 to 15]. At temperatures above 70K, with the assistance of thermal activation, <101> screw superdislocations have the tendency to cross slip along their screw segments from {111} to {010} and become less mobile. APB energy anisotropy and elastic anisotropy have been identified as the driving forces for the cross-slip from octahedral to cube planes for plasticity facilitating glide dislocations with **b** = <101>.[17]

The cross-slip model was developed quantitatively by Takeuchi and Kuramoto [18] and Lall, Chin and Pope[19] and then further refined by Paidar, Pope and Vitek[20]. It is generally referred to now as the PPV model.

In the PPV model, the cross slip process is thermally activated and the number of cross slip pinning (CSP) points (Figure 3) increases as the temperature increases, resulting in an increase in the resistance to <110> {111} slip. The yield strength decreases again when glide in the cube slip system <110>{100} becomes feasible. The PPV model was modified by Yoo[21], who included a torque term derived from consideration of elastic anisotropy. Yoo has shown that cross slip pinning will occur only when

$$[3A/(A+2)]/[\gamma_1/\gamma_0] > \sqrt{3} \quad (1)$$

Where $A = 2C_{44}/(C_{11}-C_{12})$ - Zener's ratio of elastic anisotropy, γ_1 is the APB energy in {111} and γ_0 is the APB energy in {100}.

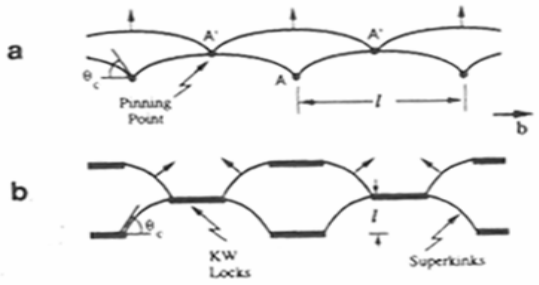

Figure 3: Illustrations of successive positions for a superdislocation moving on the (111) plane by (a) bowing between cross-slip-pining (CSP) points as envisioned in the CSP models and (b) lateral motion of superkinks between Kear-Wilsdorf (KW) locks as envisioned in the superkink models.

Application of this result (1) to Ni_3Al shows that γ_1/γ_0 is equal to between 1.1 and 1.4. The Zener anisotropy factor, which is not sensitive to temperature, was calculated to be 3.3 for Ni_3Al . Setting A=3.3 and γ_1/γ_0 =1.2, the condition for the yield strength anomaly is well satisfied for Ni_3Al. Thus the torque term derived from elastic anisotropy plays a major role in the cross-slip-pinning (CSP) process and the YSA observed in Ni_3Al.

The PPV model with the additional torque term developed by Yoo has been used to successfully explain many aspects of the yield and flow phenomena in Ni_3Al, including the strong orientation dependence of the yield strength and tension-compression asymmetry.

2.1.2 YSA in $L1_0$ Systems:

2.1.2.1 γ-TiAl The binary intermetallic phase γ-TiAl exhibits the $L1_0$ structure, which can be described as an ordered tetragonal structure with layered stacking of alternate pure Ti and pure Al layers in (002) planes (Figure 4). Using the conventional unit cell shown in Figure 5, the kinship to the fcc-structure of a disordered solid solution is apparent, and the tetragonality of the $L1_0$-structure of γ-TiAl, c/a, has a value of about 1.020[22], depending on exact composition. The tetragonal lattice of γ-TiAl is stable up to the melting temperature, T_m, equal to 1480°C for the compositions near 50at.% Ti. Figure 5 is a phase diagram of a Ti-Al System.

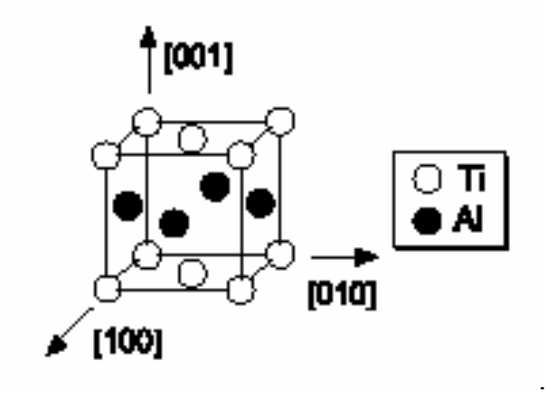

Figure 4: $L1_0$ Structure of TiAl

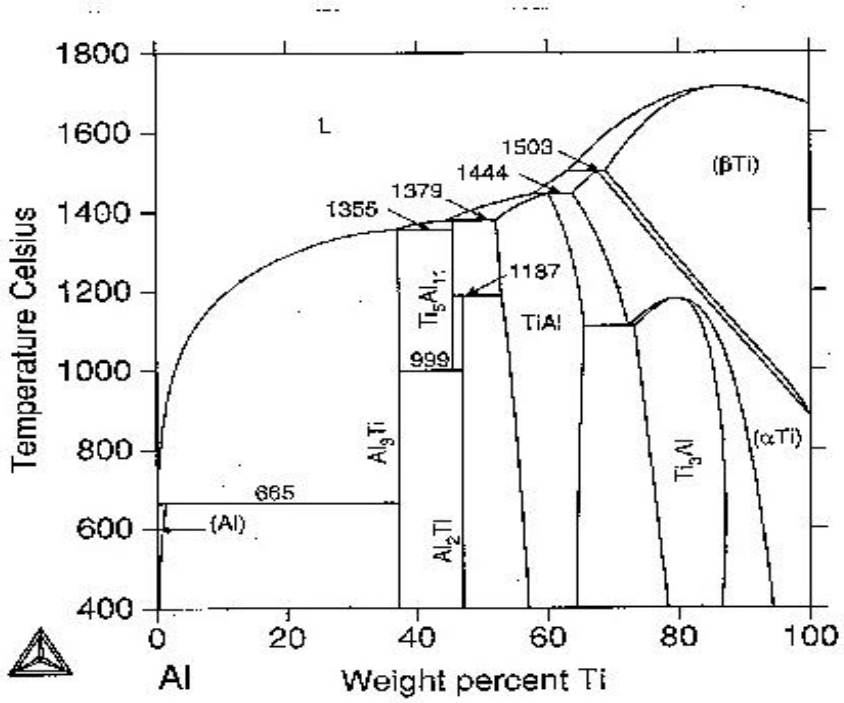

Figure 5: Ti-Al Phase Diagram

The plastic deformation of γ-TiAl is chiefly accomplished by slip and twinning involving {111} planes of the conventional unit cell (Figure 4). The atomic stacking sequence and the relevant fault vectors on the (111) plane of the $L1_0$ structure are shown in Figure 6.

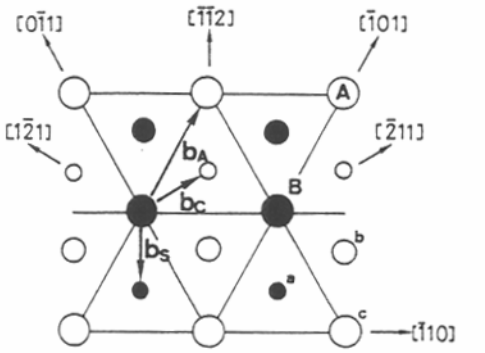

Figure 6: Atomic arrangement of (111) planes in TiAl and other $L1_0$ phases

Three major types of unit or perfect dislocations that are glissile in the octahedral planes of TiAl exist which involve in increasing length Burgers vectors of type ½<110>, referred to as ordinary dislocations (OD) as they have an equivalent in the related disordered and hypothetical FCC structure; type ½<112>, referred to as twinning superdislocations (TD); and type <101>, referred to as superdislocations (SD). The two types of superdislocations with Burgers vectors of <011> and <112>/2 can undergo various dissociations into superpartial and partial dislocations and the associated planar faults. Note that the crystallographic form of <011> includes ±[101], ±[011], ±[01-1] and ±[10-1] only. The directions ±[110] and ±[1-10] belong to the form <110> and are crystallographically not equivalent to those of the form <101>. Similarly, <112> is crystallographically distinct from <211>, and [001] is crystallographically distinct from <100> in this tetragonal crystal structure. The ordinary dislocations (OD) have a Burgers vector of ½<110>. This type of dislocation may be generated by independent sources or by glide-decomposition reactions such as

$$[01\bar{1}] \leftrightarrow [11\bar{2}]/2 + [\bar{1}10]/2 \quad (2)$$

Both source operation and glide-decomposition of superdislocations may affect the number densities of ordinary dislocations.

The ordinary dislocation is expected to dissociate into a pair of Shockley partials, with Burgers vectors of $b_1 = \left[\bar{2}11\right]/6$ and $b_2 = \left[\bar{1}2\bar{1}\right]/6$ bounding a strip of CSF,

$$[\bar{1}10]/2 \rightarrow [\bar{2}11]/6 + CSF + [\bar{1}2\bar{1}]/6 \quad (3)$$

Superdislocations with a Burgers vector of $[01\bar{1}]$ can dissociate in two ways, either four-fold or two-fold. The four-fold dissociation consist of two sets of $b_3 = [11\bar{2}]/6$ and $b_4 = [\bar{1}2\bar{1}]/6$ Shockley partials:

$$[01\bar{1}] \rightarrow [11\bar{2}]/6 + SISF + [\bar{1}2\bar{1}]/6 + APB + [11\bar{2}]/6 + CSF + [\bar{1}2\bar{1}]/6 \quad (4)$$

The two-fold dissociation comprises a pair of superpartials with parallel Burgers vectors and an APB:

$$[01\bar{1}] \rightarrow 1/2[01\bar{1}] + APB + 1/2[01\bar{1}] \quad (5)$$

Compared to the situation of the fourfold dissociation of superdislocations in $L1_2$ intermetallics (see previous section), here for the tetragonal L1o intermetallics, the fourfold dissociation of the superdislocaitons on the octahedral planes is asymmetric (equation (4)). Hence, depending on the sign of the resolved shear stress (RSS), the dissociated dislocation in (4) has different types of

leading partials and planar fault configurations. This has important implications for the cross slip behavior.

The twinning-type superdislocations $[11\bar{2}]/2$ exhibit three-fold dissociation according to

$$[11\bar{2}]/2 \rightarrow [11\bar{2}]/6 + SISF + [112]/6 + SISF + [1\bar{1}2]/6 \quad (6)$$

All of these dissociation reactions are feasible regarding elastic line energy arguments based on 'Frank's Rule', while the likely decomposition reactions are neutral regarding line energy considerations. The planar fault energies of TiAl have been determined theoretically and experimentally. The hierarchy of planar- fault energies was found to be $E_{CSF}>E_{APB}>E_{SISF}\sim E_{SESF}$[23].

γ-TiAl is one of the intermetallics which exhibits a YSA. Zupan and Hemker[24] showed that for Al-rich single crystalline γ-TiAl, the temperature of the anomalous yield stress peak and the direction of the tension/compression asymmetry depend on the crystal orientation. Also the tensile yield strength was measured to be higher compared to the compressive yield strength for [010] and [-110] crystal orientations. For loading along the [001] direction, Hemker's group found that the compressive yield strength is higher.

The similarity of L1o and $L1_2$ structures and the dominant role of superdislocation activity during plasticity suggest that the yield strength anomaly in both γ-TiAl and Ni_3Al may arise from a common, or at least a similar, origin. Non-planar sessile configurations for superdislocations in γ-TiAl were proposed by Greenbergh[25]. The stability of the core configurations and the mechanisms for the glisslile to sessile transformation must be understood

in order to link the proposed dislocation barriers to yielding. This may be accomplished by identification of the details of the fine structures of the relevant dislocations.

Woodward[26]-[27] has performed calculations of non-planar 'locked' dislocation configurations in γ-TiAl which indicate that acute angle 'roof-type' barriers have the largest thermodynamic driving force to form with the total energy for the sessile cross-slipped configuration being significantly lower than the glissile planar configuration. In these calculations, a KW- type lock, similar to that responsible for the YSA in Ni_3Al , has an energetic driving force less than half of the $L1_0$-structure specific 'roof-type' barriers. Hemker [28] and Wang [29] observed the acute angle dislocation core structure using high resolution electron microscopy (HREM).

Mixed character Shockley partial dislocations must recombine into a superpartial of pure screw character in order to cross slip. Bonneville and Escaig [30] showed that the resolved shear stress on a dissociated FCC dislocation will either force the two partial dislocations apart, inhibiting cross slip, or force them together, promoting cross slip. Schmid's law has been modified to incorporate "Escaig forces". Paidar et al. [31] have predicted the orientation dependence and tension/compression asymmetry of the critical resolved shear stress (CRSS) in Ni_3Al. Also the force balance between the partial dislocations in the framework of anisotropic elasticity has been clarified by Yoo[32] . Yoo showed that out-of-plane forces produce a torque that pushes the dislocation off the octahedral glide plane. This force is known as the "Yoo Torque"; it is pronounced for materials with high elastic anisotropy and has been shown to be a significant factor in determining the cross slip frequency of dislocations in Ni_3Al. Considering the dissociated superdislocation configuration (4) and using the codes of Yoo and Fu[33], calculations show the stress on the superpartial in TiAl to be approximately 300-600 MPa depending on the

SISF and APB energies. Hence, the magnitude of the stresses associated with the Yoo Torque is substantially larger, more than three times, than the typical resolved shear stress (RSS) on the cross slip planes primary slip system dislocations in TiAl. The large magnitude of the Yoo torque compared to the RSS significantly increases its effect on the cross-slip locking of superdislocations, and like the RSS, promotes the formation of the low energy 'roof type' barrier through cross-slip of the trailing CSF dissociated superpartial dislocations in each of the hard orientations for tension and compression along principal crystal axes such as [001], [010] and [-110]. Here the hard orientations refer to loading axis directions which exhibit an increased amount of required shear stress to induce plastic yielding relative to the soft orientations. The hard orientations are $[001]_{compression}$, $[010]_{tension}$,$[-110]_{tension}$ and have have been determined by experiment [34].

The direction that a dislocation glides depends on the sense of the applied load. The slip systems with the maximum resolved shear stress for each of the three orientations ([001], [010] and [-110]), have been analyzed to determine the direction the dislocation travels on the slip plane and the leading stacking fault as a function of applied load.

Figure 7 schematically shows dissociated superdislocations for the three primary slip systems for the three different loading axes. These superdislocations are represented using Thompson notation[35].

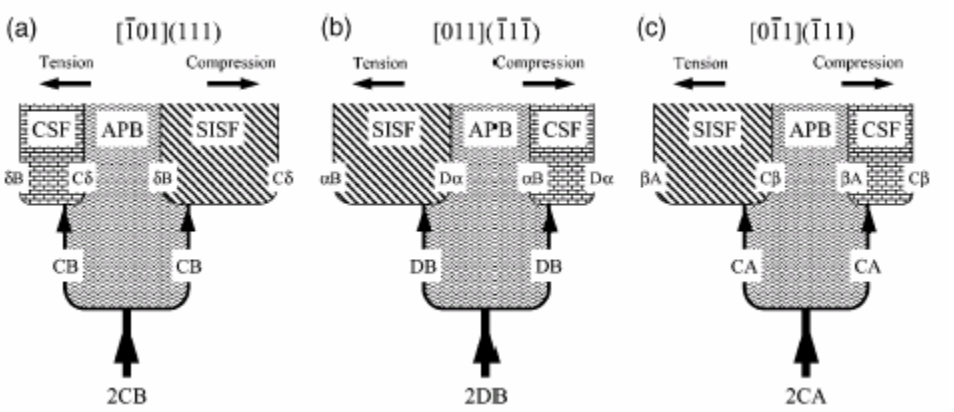

Figure 7 :Schematic drawing of the crystallographic dissociation of superdislocations associated with loading axes (a)[0 0 1], (b)[0 1 0] and (c)[-1 1 0].

Hence, the dissociation reaction of a superdislocation with a Burgers vector of b = [-101] on (111), [011] on (-11-1) and [0-11] on (-111) equivalent to that described in (4) can be expressed in terms of Thompson notation as follows:

[-101] => 1/6[-211] + CSF + 1/6 [-1-12]+ APB+ 1/6 [-211] + SISF + 1/6 [-1-12]

2CB => δB + CSF + Cδ + APB+ δD + SISF + Cδ

[011] =>1/6[-112] + SISF + 1/6[121] + APB + 1/6 [-112] +CSF + 1/6[121]

2DB => αB + SISF + Dα +APB+ αB +CSF+ Dα

[0-11] =>1/6[1-12]+ SISF+1/6[-1-21] + APB + 1/6[1-12]+CSF + 1/6 [-1-21]

2CA => βA +SISF+ Cβ + APB + βA + CSF + Cβ

For the [001] loading orientation, a tensile shear stress drives the superdislocation 2CD of the primary slip system to the left in the diagram of Figure 7a, while a compression moves the same dislocation to the right. Hence for [001]-loading the active superdislocations are gliding with the CSF dissociated superpartial leading in tension and the SISF dissociated superpartial leading in compression. Figures 7b and 7c also represent the directions of motion for superdislocations of the primary slip systems for the loading orientation being near [010] and [-110].

It is found that the tension/compression asymmetry is the same for [010] and [-110] but in the opposite sense for [001], which is consistent with the description of dislocation motion outlined schematically in Figure 7. In all cases the yield strength is lowest when the CSF leads the gliding dislocation and the highest when the SISF dissociated superpartial leads.

This indicates that the constriction and cross slip of the leading superpartial dislocation does not have a strong influence on the YSA. Since constriction and cross-slip of the leading SISF dissociated superpartial is unlikely. The formation of roof-type barriers may in fact be governed by the cross-slip of the trailing CSF dissociated superpartial. The width of the CSF is much less than that of SISF.

Figure 8 shows the critical resolved shear stress (CRSS) values for the three conditions where the CSF trails, i.e. for compression along $[001]_c$, and tension along $[010]_T$ and $[-110]_T$. The flow strength for each of these conditions was found to be higher than for their tensile or compressive counterparts. Clearly, the flow-stress data of these hard orientations collapse to a single curve. This indicates that Schmid's law is obeyed when asymmetry of superdislocation motion is accounted for. Figure 8 shows that the anomalous yielding peaks occur at about the same temperature for these "hard" orientations, which points to the activity of a single thermally

activated mechanism, presumably the cross-slip locking of superdislocations by the formation of roof-type barriers.

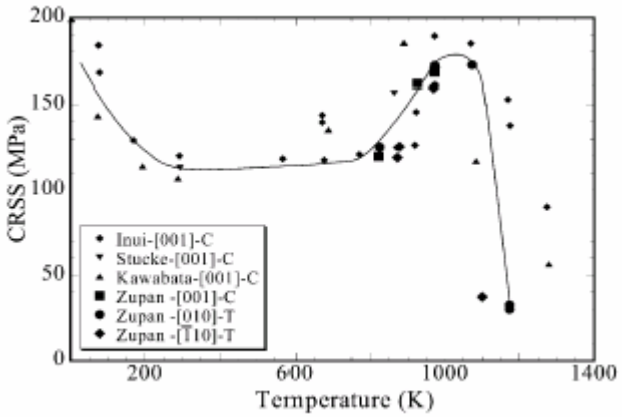

Figure 8: Plot of the CRSS for the hard directions. The data for these directions converge to a single CRSS and have the same peak temperature for the flow strength anomaly.

Figure 9 shows the CRSS values for the conditions where the CSF lead, $[001]_T$, $[010]_C$ and $[-110]_C$. In these soft orientations the CRSS values, the flow stresses do not collapse to a single curve. The magnitude of the flow strength anomaly is approximately the same, but the peak temperature for [010] is lower than for [001] and [-110]. This indicates that the thermal activation barrier for cross-slip is lower for the near [010] loading axis orientation than for the other two orientations. The overall strength is lower than for the hard orientations and the [010] loading orientation behaves differently than the other two orientations. These observations indicate that an obstacle other than roof-type barriers may be responsible for the yield strength anomaly for the soft orientations.[36]

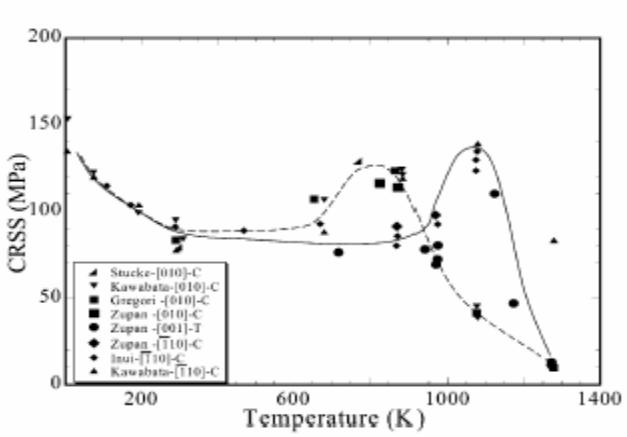

Figure 9: The CRSS for the three weak orientations. This data does not converge to a single CRSS. The peak temperature of the anomaly for the [0 1 0] orientation was measured to be much lower than that of the [0 0 1] and [_1 1 0] loading axes.

To study the effect of resolved shear stresses, Figure 10 shows the planar geometry for the [-101](111) slip system that would be active for [001] loading axis orientations. Figure 10 shows the direction of the resolved shear stresses (RSS) for the primary and secondary octahedral slip planes. Under compressive loading the dislocation glides to the right, and the RSS on the secondary octahedral plane acts to drive back cross-slip of the CSF into an acute angle roof-type barrier, Figure 10c, which is in agreement with Woodward's prediction and Gregori's ,Wang's, Hemker's experimental observations of superdislocations in γ-TiAl[37] . In case of tensile loading, the dislocations moves to the left and the RSS on the secondary octahedral system promotes the formation of high energy non-planar configuration with a CSF located on the cross slip plane, Figure 10b. The formation of "roof-type" barriers is also favored for [010] and [-110] tensile loading. The fact that the resolved shear stress promotes cross-slip of the trailing CSF dissociated superparital dislocations is in agreement with weak-beam TEM observations of Gregori and Veyssiere[38].

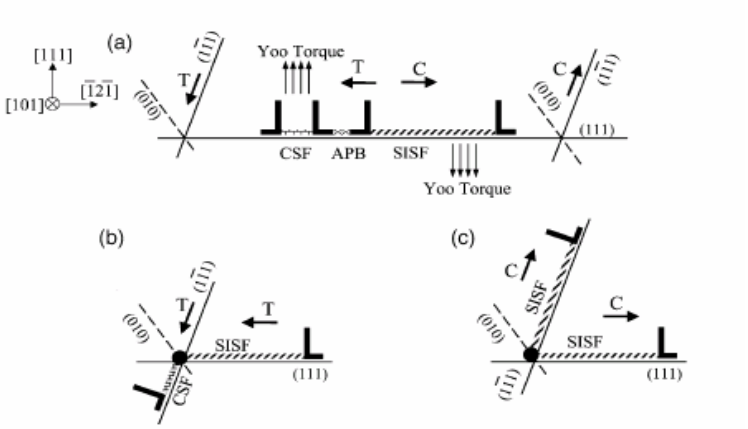

Figure 10 : Schematic of a [1 $\bar{1}$ 01] superdislocation gliding on the (1 1 1) plane displaying the motion of the dislocation when the crystal is loaded in tension or compression for orientations near [0 0 1]. Under a compressive load, the trailing CSF dissociated superpartial dislocations can cross-slip on to a second octahedral plane forming an acute angle "roof-type" barrier.

The anisotropic interaction forces on dissociated screw dislocation in γ-TiAl were calculated by Yoo and Fu[39]. In figure 10, which depicts the [-101](111) slip system, the tangential force from crystal anisotropy pushes the CSF dissociated superpartial off the slip plane in the [111] direction, normal to the (111) glide plane. The stress on the superpartial is calculated using the codes of Yoo and Fu to have a magnitude of approximately 300-600 MPa depending on the SISF and APB energies. This magnitude of stress is larger, by more than three times, than the RSS on the cross slip plane. Comparing Yoo torque values for γ-TiAl with Ni_3Al one finds that they are of similar magnitude. For Ni_3Al the Yoo torque is 540 MPa[40] . However, the yield strength of Ni_3Al is much higher than for TiAl and the level of RSS during plastic loading are comparable to the torque stress for Ni_3Al. In γ-TiAl the very large magnitude of the Yoo torque compared to the RSS significantly increases its effect on the cross-slip locking of superdislocations.

The Yoo torque promotes the formation of the low energy "roof-type" barrier through cross-slip of the trailing CSF dissociated superpartial dislocation in each of the hard orientations in TiAl Figure 10c. This supports the idea of the formation of roof-type barriers leading to anomalous yielding in γ-TiAl. For the soft loading orientations the Yoo torque acts against the RSS and appears to lead to the formation of alternative, unidentified but less formidable, barriers[41].

In conclusion, given that the Yoo torque is much higher than the secondary slip system RSS and the small effect of Escaig forces it appears reasonable to rationalize that the cross-slip locking of the trailing CSF dissociated superpartial is responsible for the YSA in the hard orientation loading geometries for TiAl when <101>{11-1} slip systems are active.

2.1.2.2 FEPT FePt is one of the compounds that have L10 structure. Figure 11 shows the phase diagram of Fe-Pt system42 and indicates that stoichiometric FePt solidifies into a disordered face centered cubic fcc phase from the melt and transforms into a tetragonal ordered L10 phase near 1573 K. The order-disorder transformation takes place at a very high temperature. In ordered FePt, the constituent Fe and Pt atoms are disposed in alternative layers of {002} planes. The high order-disorder transition temperature of 1573 K of FePt allows for investigations of deformation behavior at high temperatures.

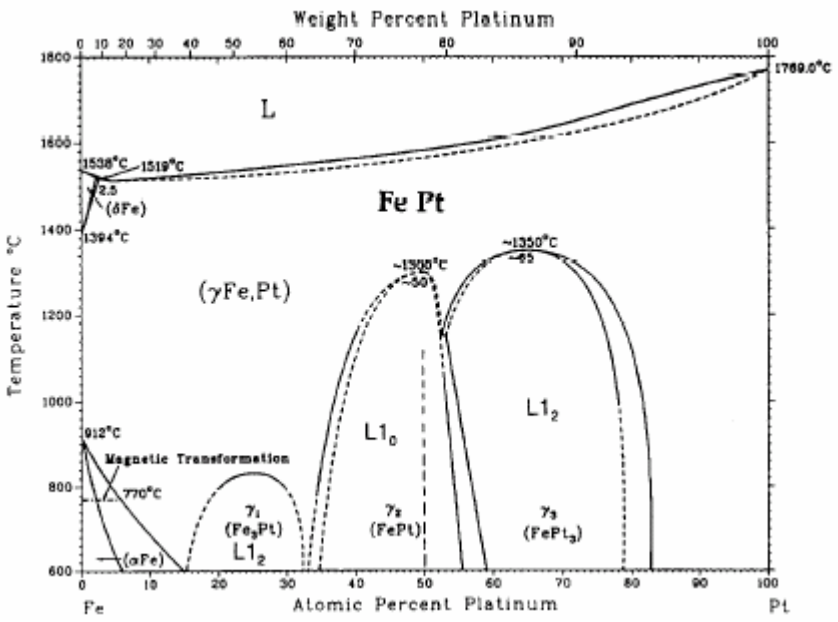

Figure 11 : Binary phase diagram of Fe-Pt.

Whang, Feng and Gao [43] investigated the deformation behavior of FePt through compression deformation at temperatures up to 1073K. Figure 12 shows the temperature dependence of the yield stress (0.2% offset) from room temperature (RT) to 1073K. The decay in yield stress with increasing temperature is moderate from RT to 1073, indicating that here is no anomalous hardening or YSA in FePt, which is in contrast to the case of the isostructural TiAl .

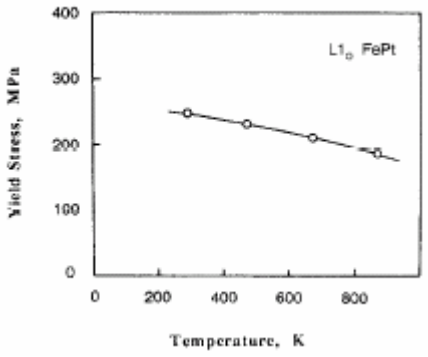

Figure 12: Plot of yield stress vs. temperature in FePt.

The investigations of the deformation structures by transmission electron microscopy (TEM) showed that the main deformation mechanisms are slip and twinning on octahedral planes. Also, researchers had observed predominant superdislocations with Burgers vector of the type [101] in the specimens compressively deformed at 77K[44], In addition, a significant amount of ordinary dislocations with Burgers vector ½[110] and superdislocations with Burgers vector ½[112] were also observed at 77K.The weak beam TEM images of the superdislocation with Burgers vector [101] showed no sign of self-dissociation, which is the converse to the case of [101] superdislocations in $L1_0$ type TiAl.

At room temperature an increased amount of ordinary dislocation activity was observed. Further increase in deformation temperature to 873K and 1073K resulted in further increased ordinary dislocation activity and density.

The magnitude of the yield strength of both FePt and TiAl at RT is similar. But at high temperature, the yield strength of FePt decreases in monotonic fashion, showing negative temperature dependence, i.e. a normal temperature dependence of the yield stress, while TiAl exhibits anomalous temperature dependence of the yield stress.

Whang et al[45] suggested that below RT, the large yield stress appears to be associated with high Peierls stress and the difficulty of nucleating ordinary dislocations. Furthermore, the reported low density of ordinary dislocations in FePt at low temperature indicates that the Peierls stress increases more significantly for ordinary dislocations than for superdislocations at these decreasing temperatures.

The differences in the fine structures and the general characteristics of the dislocation substructures after deformation may explain the discrepancy between the deformation mode of FePt and that of TiAl. First, ordinary dislocations and twins govern the deformation in FePt at

RT and 673K. Second, at RT and 673K, the ordinary dislocations were curved without any other special character, while in TiAl the ordinary dislocations lines at RT were straight implying the existence of a high Peierls stress. But at high temperature the ordinary dislocations lines in TiAl alloys become curved. In FePt, the superdislocations b=[101] show neither self-dissociation nor cross slip onto cube planes at RT and 673K, although it is possible that the dissociation or cross slip width might be too small to be identified by weak-beam dark field TEM. Hence, the fine structure of the glide dislocations is consistent with the absence of the YSA in FePt.

2.2 FEPD BACKGROUND

2.2.1 Crystal Structure and dislocations

Figure 13 shows the binary phase diagram of the Fe-Pd system, which is very similar to that of FePt system (Figure 11). FePd of equatomic composition is the focus of this study and shows a stable fcc (γ) phase at high temperature and the tetragonal $L1_0$ ordered ($\gamma 1$) phase at temperatures lower than about 647^{o}C (Tc=920 K).

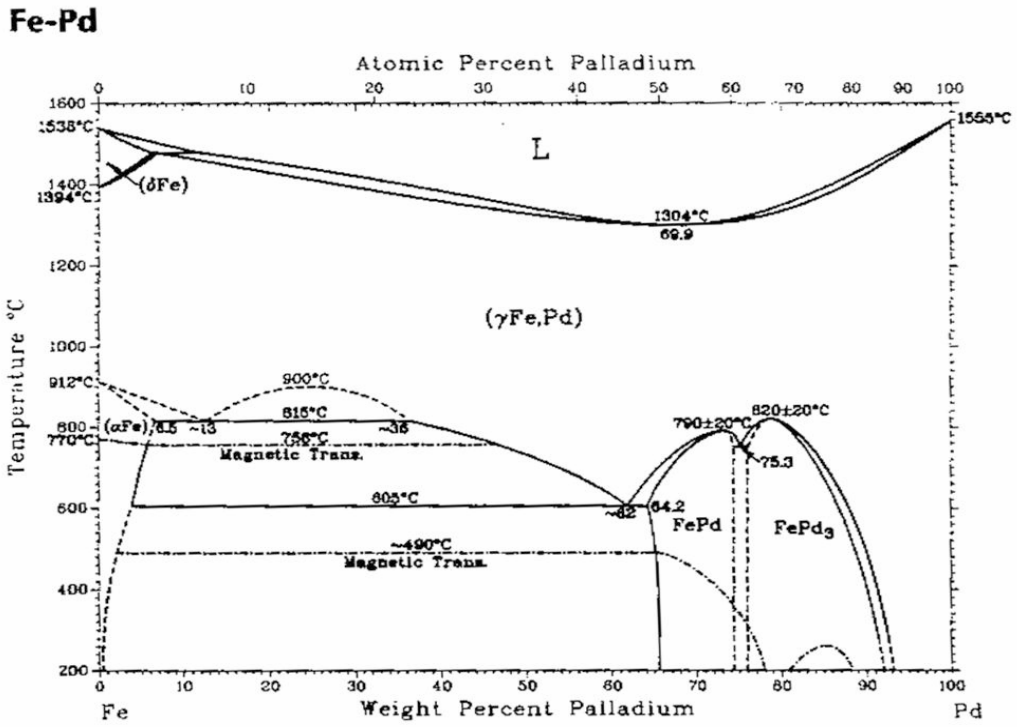

Figure 13: Fe-Pd phase diagram**.**

The order-disorder transformation of equiatomic FePd is considered to be a neostructural transformation. This means that the ordering process results in a change in the crystal structure (i.e. cubic $\rightarrow$ tetragonal). The neostructural transformation is accompanied by small lattice distortions, which are anisotropic, producing a more complicated mode and morphology of transformation. The misfits between the parent phase and the product phase are asymmetric and the resultant microstructures are a composite of the various nonequivalent habit or orientation variants of the uniaxial tetragonal product that forms from the highly symmetric fcc parent

phase. Hence, these microstructures contain transformation induced twins, and are known as strain-accommodating polytwin structures.

According to the FePd phase diagram, the equatomic alloy should transform completely from disordered γ(A1) to ordered γ1($L1_0$) at temperature $<T_c$ ~620°C. The γ phase has a fcc structure (Figure 14a), while the γ1 phase has a tetragonal superlattice structure ($L1_0$) (Figure 14b). In the tetragonal $L1_0$ phase, the alternating (002) planes contain only Fe atoms or Pd atoms, producing a chemically ordered structure.

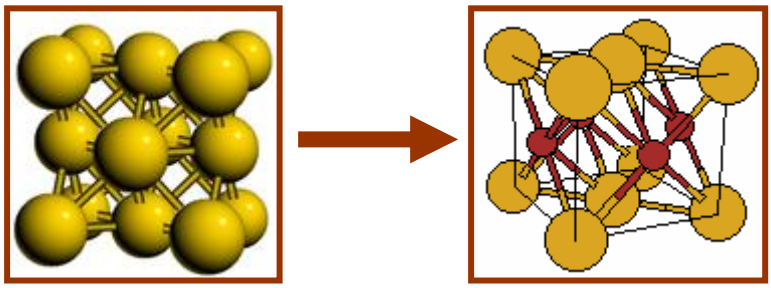

a b

Figure 14: a. FCC structure (γ phase) b. $L1_0$ structure (γ1 phase)

The ordering process leads to a contraction in the [001] direction (c-axis) and an expansion along the [100] and [010] directions, which may be considered to be associated with the difference in the size of the two atom species and gives rise to slight tetragonality. The tetragonal ordered structure has an equilibrium axial ratio (c/a) of approximately 0.966[46 47]. As a result, a considerable amount of elastic strain and misfit energy results during the process of ordering. One of the major differences between FePd and TiAl is the deviation of the c/a ratio from unity. In TiAl, the $L1_0$ structure has c/a >1 (c/a=1.015[48]), while most other $L1_0$ intermetallics with some exceptions (TiHg and HgZr) form with c/a ratio less than unity. [49]

One of the most general features associated with ordered systems is a lowering of symmetry upon ordering from the high temperature disordered phase from which it transforms. As a result of this change in symmetry, the periodicity of the lattice increases along the slip directions. Therefore, the dislocation that is perfect in the disordered structure will not be perfect in the ordered structure. The perfect dislocation in the ordered phase will have a Burgers vector twice the length of that in the disordered phase and is called a "superlattice" dislocation or superdislocation for short.

Marcinkowski, Brown and Fisher[50], in 1961, were the first to speculate on the possible dislocation configurations in $L1_0$ system. To illustrate the details of dislocations structure in $L1_0$ system, TiAl can be taken as an example since it was studied extensively in the last two decades.

Regarding the possible perfect unit dislocations and their possible dissociations into imperfect partial dislocation the situation in g1-FePd is crystallographically identical to the details described in the previous section on TiAl. Hence, in FePd also three different unit dislcatons, the ordinary dislocation (OD) b=1/2 <110>, the superdislcation (SD) b=<101> and the twin dislocations (TD), b =3x 1/6 <112> = ½<112> . The following dissociation schemes or reactions are feasible based on elastic line energy considerations, are reasonable to consider and identical to those described for TiAl (e.g. reactions (3)-(6)):

OD's may dissociate into Shockley partials bounding a CSF ribbon,

$$\frac{1}{2}\left[\bar{1}10\right] \rightarrow \frac{1}{6}\left[\bar{2}11\right] + CSF + \frac{1}{6}\left[\bar{1}2\bar{1}\right] \qquad (7)$$

Depending on the details of the absolute values and the hierarchy of the energies of the different planar faults, the <011> superdislocation can dissociate asymmetrically and fourfold,

$$[01\bar{1}] \rightarrow \frac{1}{6}\left[1\,1\bar{2}\right] + SISF + \frac{1}{6}\left[\bar{1}2\bar{1}\right] + APB + \frac{1}{6}\left[1\,1\bar{2}\right] + CSF + \frac{1}{6}\left[\bar{1}2\bar{1}\right] \quad (8)$$

or two-fold and symmetrically into two superpartials,

$$[01\bar{1}] \rightarrow 1/2[01\bar{1}] + APB + 1/2[01\bar{1}] \quad (9)$$

The three-fold dissociation of ½ [11-2] superdislocation involves two stacking faults

$$\frac{1}{2}\left[1\,1\bar{2}\right] \rightarrow \frac{1}{6}\left[1\,1\bar{2}\right] + SESF + \frac{1}{6}\left[1\,1\bar{2}\right] + SISF + \frac{1}{6}\left[1\,1\bar{2}\right] \quad (10)$$

Unlike for TiAl , the details of the planar fault energies and the hierarchy of the planar fault energies in the {111} planes of FePd are not known. Thus, the preference for any of the dissociation reactions described in equations or relations (7) to (10) and the width of the planar faults ribbons remain to be addressed. However, assuming purely hard-sphere models and violations of nearest neighbor and next nearest neighbor bond across the respective fault planes, i.e. using a purely geometric approach, predicts a hierarchy of planar fault energies as E_{CSF}> E_{APB}>E_{SISF} for the {111} plane.

Wiezorek and Xu [51] have studied the room temperature deformed polytwin $L1_0$ ordered FePd by TEM. They compared the dislocation structures present in samples that had experienced different amounts of plastic tensile strain at room temperature and concluded that twinning and ordinary dislocation are complementary deformation modes. These two complementary modes must be active at yielding in different twin variants that constitute a polytwinned (PT) grain in the polycrystalline aggregate because they are required to propagate plastic shear and slip across the dodecahedral PT interfaces. A model for the most likely shear transfer process of ordinary dislocation glide and for twinning across the PT-interfaces has been proposed[52]. The basic predictions of the purely crystallographically derived models for shear transfer of OD and TD across the PT interfaces in PT-polycrystalline $L1_0$-FePd have been confirmed by experimental

TEM observations[53]. The transfer of mechanical twinning shear across the PT interfaces is favorable regarding elastic line energy and produces gliding OD's and residual Burgers vector content in the form of sessile superpartials, which in pairs constitute mobile SD's. However, the transfer of OD's across the PT interfaces is energetically not favorable and associated with an energy penalty. Therefore, transfer of OD's across the PT interfaces can be considered to be associated with an obstacle strength, while the transfer of mechanical twins is relatively easy. The twin transfer process observed in [55] and predicted in [56] is energetically down-hill and results in glissile OD's and SD's. Thus, observation of all three types of perfect unit dislocations in deformed PT-polycrystals of $L1_0$-FePd does not allow for direct conclusions regarding the ease of their glide activation and accordingly regarding a hierarchy of their critical resolved shear stresses, which are predicted to be different for octahedral glide of OD's ,SD's and TD's or mechanical twinning. This clearly complicates attempts to identify reasons for the YSA observed for FePd when polycrystalline polytwinned FePd is used. The transfer of mechanical twins across the PT interfaces is energetically downhill. Hence, the PT interfaces are not strong obstacles for the propagation of mechanical twins through a PT-grain of gamma1-FePd. However, for both transfer of ordinary dislocations or the <101>-superdislocations PT interfaces are strong obstacles because they must change Burgers vectors via a boundary reaction which always produces residual Burgers vector content that is not glissile in the relevant {111} planes and will become sessile debris deposited at the PT interfaces. This debris represents additional obstacles for subsequent transfer of OD's and SD's across the PT interfaces. The Obstacle strength of PT interfaces regarding transfer of OD's and SD's will increase as the debris content increase in the interface. If thermally assisted motion of dislocations (climb) becomes significant or possible then it might become easier for the gliding dislocations to overcome the barriers

represented by the original PT interfaces and the dislocation debris produced by previous transfer reactions or processes. Alternatively, the boundary reaction that transforms the Burgers vector of the incident glide dislocation (e.g. OD in the matrix PT-lamella) to the Burgers vector of the dislocation that can glide in the receiving or twin-PT-lamella may become more difficult as temperature increases from room temperature in an intermediate range because the PT interface, a {011} plane, becomes sufficiently attractive for non-planar configurations of the incident and/or debris dislocations. Hence, elevated temperature may decrease or increase the barrier strength of the PT interfaces. This would lead potentially to a positive temperature dependence of the yield stress for an intermediate range of temperatures or simply to a negative temperature dependence of the yield stress. At sufficiently high temperature (e.g. at about T/TM >0.45 or so), the polytwin structures in FePd may actually coarsen under the influence of the applied mechanical stress and the elevated temperature, thereby reducing the yield stress. Hence, presence of the polytwin interfaces clearly complicates a basic study of the temperature dependence of the yield stress and possible origins of the previously reported YSA in FePd.

3.0 MOTIVATION

A yield strength anomaly (YSA) has been observed in $L1_0$-ordered FePd between about 300-700K. However, previous work has not provided clear explanations regarding the microstructural or mechanistic origins for this observation.

In order to develop a better understanding of the YSA in a $L1_0$-ordered FePd system, which typically has been related to dislocation fine structure details in other intermetallics that exhibit a YSA, the elastic constants need to be measured. The elastic constants of FePd should be compared to those of the isostructural FePt, which does not show YSA, and TiAl, which does.

TEM is typically used for investigation of the dislocation fine structure. Quantitative and reliable interpretation of TEM dislocation images requires image contrast simulations to allow comparison with experimental observations. TEM Image Simulation for Ordinary Dislocations, Twin Dislocations and Superdislocations can be performed for both FePd and FePt, as long as the elastic constants are known. Image Simulation will provide contrast guidance for experimental studies in both FePd and FePt. Experimental TEM studies of the fine structure require extensive tilting of the thin crystal section within the magnetic field of the objective lens of the TEM instrument and are difficult to perform for the hard ferromagnetic FePd and FePt intermetallics since magnetic effects of the sample material on the electrons used for imaging lead to complicated artifacts in images upon tilting through significant angles. Hence, image

simulations may assist in identifying appropriate imaging conditions under which significant and relevant differences in the dislocation image contrast may be expected for the dislocations in the two different intermetallics.

Previous work on in FePd was not sufficiently detailed and the origin of the apparent YSA remains unexplained. Although the work performed here cannot be expected to result in a direct explanation of the YSA in the $L1_0$ FePd system, it represents an important initial step in attempts to develop a better understanding of the origins of the YSA in FePd.

4.0 OBJECTIVES

The objectives of this study are:

To determine the elastic constants of FePd and compare them to the elastic constants of FePt and TiAl.

To perform plastic deformation experiments to introduce dislocations into FePd in a controlled manner suitable for experimental study by TEM.

To perform TEM Image Simulation for different types of dislocations expected in FePd and FePt.

The following paragraphs describe objectives 1 and 3 in a little more detail:

To determine the elastic constants of FePd and compare them to the elastic constants of FePt and TiAl :

Elastic constants describe the intrinsic properties of the material. Details of the dislocations fine structure, such as the details of dissociations and the decomposition of dislocations and the relevant planar fault energies are determined by the elastic constants. The elastic interactions (repulsion, attraction) between partial dislocations that participate in the dissociations and decompositions of unit dislocation can be computed using anisotropic continuum elasticity theory if the elastic constants, dislocation line direction and Burgers vector are known. Knowing

the elastic constants of FePd and comparing them with those of FePt and TiAl will build a basic understanding of the origin of the differences in plastic behavior.

To perform plastic deformation experiments to introduce dislocations into FePd in a controlled manner suitable for experimental study by TEM:

Plastic deformation can be introduced to FePd sample with a mechanical compression test. The mechanical compression test can performed till the yield point of FePd sample. Yield Stress value can be determined. Intensive TEM study can results in a conclusion about the active slip systems in FePd sample and active dislocation type.

TEM Image Simulation for different type of dislocation in FePd and FePt :

The image simulation of Ordinary Dislocations (OD), Twin Dislocations (TD) and Super Dislocations for both FePd and FePt will build a contrast guidance for the dislocations contrast in different dislocations. Optimal Weak Beam Dark Field imaging conditions will be established for FePd based on simulations. This will assist in identification of experimental TEM procedures suitable for the identification of relevant details of the dislocation images.

5.0 THEORY AND EXPERIMENTS

5.1 GROWTH AND PROPERTIES OF SINGLE CRYSTALS OF FEPD (PARTLY PUBLISHED IN ACTA MATERIALIA 54 (2006) 881-889)

5.1.1 Fabrication of $L1_0$-FePd single crystals

Equiatomic FePd undergoes an order-disorder transition at about 923K from disordered FCC to an ordered $L1_0$ phase. There are three variants of the ordered phase since the symmetry of the ordered phase is lower than that of the disordered phase. In the absence of any external fields all three variants form with an equal probability, resulting in a {101}-plane conjugated or poly-twinned structure.

The application of an external field, mechanical stress or a magnetic field during the ordering process is expected to lead to the l formation of a single favorably oriented variant in preference to the other two possible variants. For example, Yermakov and Maykov[54] concluded that a mono-variant structure was realized for a single crystal specimen ordered under a compressive stress. External fields certainly modify the orientation variant structure of the ordered phase.

Tanaka et al.[55] studied the effect of external stress and a magnetic field on the formation of microstructure of FePd alloys.

Tanaka's group studied the effect of a compressive stress field as follows:

- Figure 15 shows the two schemes of heat treatments:
  - Slow cooling across the order-disorder transition temperature T_t
  - Isothermal annealing.

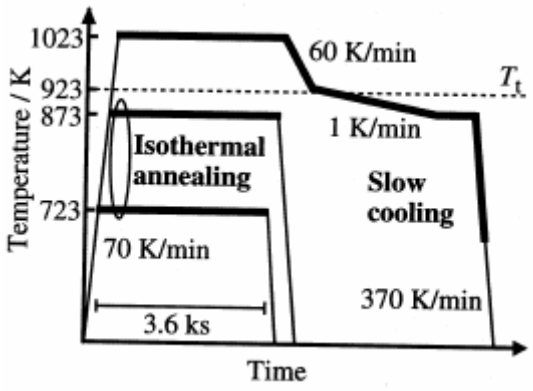

Figure 15: Heat-treatment diagram for ordering under compressive stress. Thick lines indicate the application of the compressive stress.[56]

- Figure 16 shows the volume fractions of the three variants that for stresses of 10MPa and 20MPa, the specimen was completely ordered with only one type of variant.

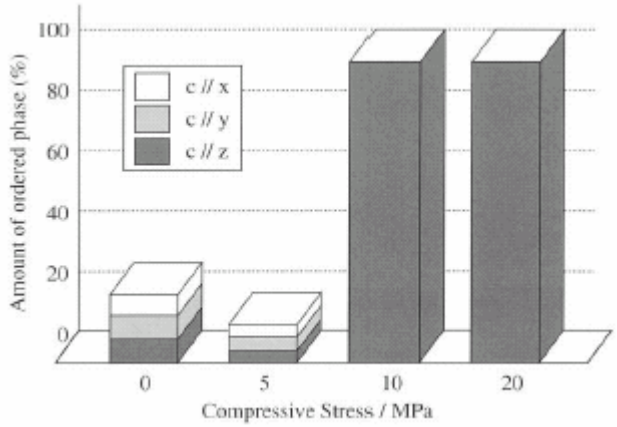

Figure 16: Volume fractions of the three variants of the ordered phase after slow cooling under different compressive stresses. The residual material is disordered.

- Figure 17 shows the results after isothermal annealing for 3.6 Ks. The rate of ordering without applied stress is distinctly different at the two temperatures. The total amount of the ordered phase is larger for the annealing at 723 K than at 873 K in the absence of an applied mechanical stress.

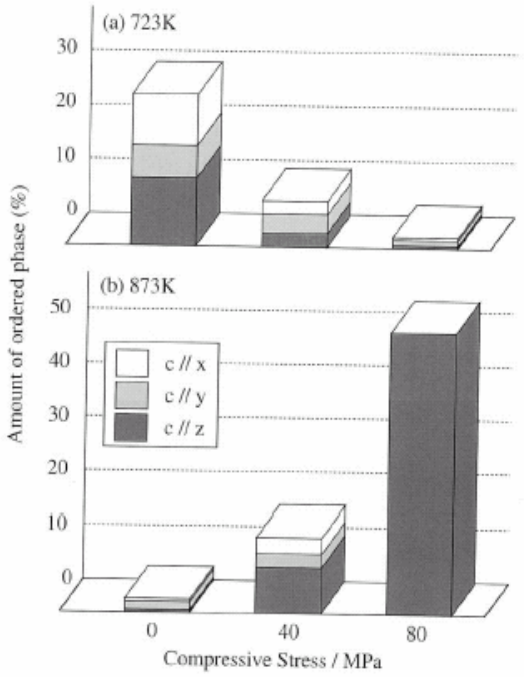

Figure 17: Volume fractions of the three variants after isothermal annealing for 3.6 Ks under different compressive stresses at (a) 723 K and(b) 873 K.

- At 723 K, the application of the stress did not yield preferential formation of particular variants; the total amount of the ordered phase was decreased by the application of stress. In contrast, at 873 K, the stress effect was very pronounced. In addition to the formation of mono-variant structures, the total amount of the ordered phase increased dramatically under the application of the compressive stress.

Tanaka's group also studied the effect of a magnetic field on the transformation and orientation variant selection. Fig 18 shows the magnetic field dependence of the amount of ordered phase annealed at 673, 773 and 793 K. in the absence of a magnetic field, the three variants were formed in almost equal proportions. When the annealing temperature was 673 K, the total amount of the ordered phase increased with the application of a magnetic field. The enhancement was more significant for the z-variant than the other two. The volume fraction of the z-variant increased from about 33% for 0T of applied magnetic field to about 50% under conditions of applied magnetic fields of between 6T to 10T. However, the total amount of the ordered phase was virtually independent of the strength of the magnetic field when the specimens were annealed at 773K. At 793K, the trend was quite different. A very significant magnetic field effect was observed; the ordering was fully completed, with the formation of a nearly mono-variant structure. Hence, it has been shown that monovariant $L1_0$-FePd can be attained by application of an external mechanical stress on the order of 10-20 MPa or a substantial magnetostatic field of about 6T parallel to a cube axis of the disordered phase while isothermally annealing at about 793-873K.

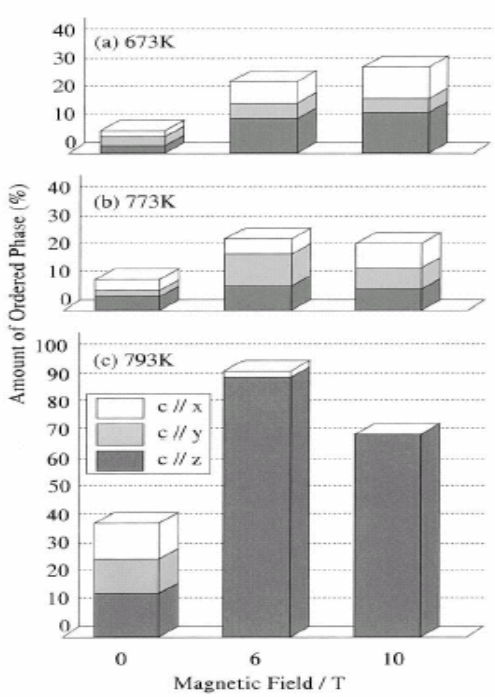

Figure 18: Volume fractions of the three variants after isothermal annealing for 3.6 Ks under the magnetic fields along the z-direction.

5.1.2 Fabrication of equiaxed $L1_0$-FePd polycrystals

Previous studies have shown that changes in the morphology and the scale of the microstructure of ordered $L1_0$-FePd can be accomplished by thermomechanical processing.[57] Typically these thermomechanical processing schemes involve cold-deformation of the metastable FCC-phase followed by annealing at a temperature below T_c, about 923K for FePd. It has been shown that the thermomechanical processing is suitable for suppressing the formation of the polytwinned $L1_0$-ordered state [58]. Cold-working in the disordered state followed by order-annealing at T<Tc involves a combined reaction (CR) in the solid state of concomitant annealing of deformation-induced crystal defects and the ordering transformation[59] [60]. For certain processing conditions

the CR transformation of the microstructure can be used to replace the polytwinned state entirely with an equiaxed microstructure of mono-variant $L1_0$ ordered FePd grains with significantly enhanced magnetic properties.

Polycrystalline non-polytwinned FePd samples can be prepared using the following process:

1. An FePd sample should be prepared from high purity elemental starting materials (Pd 99.95%, and Fe 99.98% purity) using vacuum arc melting in a residual atmosphere of purified argon gas.
2. Sections from the as-cast buttons should be cold rolled to about 50% reduction in thickness.
3. Homogenization treatment at 950^{o}C (1223K) for 6 hours (21.6 Ks) to 24 hours should be performed, followed by quenching into ice-brine. In the as-quenched state, the material consists of stress free grains of the disordered FCC FePd solid solution .
4. Billets of the as-quenched material 36 mm long with square cross-sections of 6x6 mm2 should be cold deformed at room temperature by a single ECAP pass, 120^{o} inner die angle.
5. After the ECAP , isothermal annealing should be performed at temperatures ranging from 673 K to 873 K, well below the critical ordering temperature T_c=923K.
6. A billet 6mm thick (4mmx24mm in width and length) should be cold rolled to 97% reduction in thickness to 180 μm with multiple passes.
7. Isothermal annealing after cold-rolling should be performed at temperatures between 623K and 873K.

These types of morphologically controlled microstructures are better for the detailed study of the mechanical behavior and dislocation behavior, because in this controlled microstructure the {101} polytwins have been eliminated by the thermomechanical process. $L1_0$-ordered FePd alloys free of the polytwinned microstructure will be suitable for the investigation of the fine structure of dislocations after deformation at room temperature and high temperature. This will enable us also to further elucidate the role of the polytwins in the yield strength anomaly that has been reported for FePd previously.

5.1.3 Experimental Methods:

The equiatomic FePd alloy was prepared from high purity elemental starting materials (Pd 99.95% and Fe 99.98%) using vacuum arc melting in a residual atmosphere of purified argon gas. It was cast into a water-cooled copper hearth at The Materials Preparation Center of the Ames Laboratory (Ames, IA). Then it was sectioned from the as cast button to sections that were about 50 mm long with rectangular cross sections of 12 mm by 6 mm. These sections were cold-rolled to 50% reduction in thickness prior to a recrystallization heat treatment at 950˚C for 6 hours under a residual atmosphere of purified argon gas followed by quenching in ice-brine. A cylindrical single crystal of the disordered FCC phase with approximate dimensions of 40 mm in length and 12 mm in diameter was grown subsequently using the Bridgman method. The single crystal growth was performed at the Institute of Applied Physics, Swiss Federal Institute of Technology (ETH) Zurich, Switzerland. Orientations of sections from the single crystal were determined to within 0.5˚ of precision using the Laue back reflection X-ray technique. A parallelepiped of dimensions (6x7x17) mm^3, with the longest edge parallel to [119], was

prepared using a wire saw. A single crystal of the $L1_0$-ordered phase γ_1-FePd was obtained by applying a small compressive uniaxial elastic stress parallel to [119] during heat treatment to induce the ordering phase transformation. The direction [119] was chosen as it is close enough to [001] to select one of the three possible orientational order variants[61]-[62], yet sufficiently far from [001] to favor a single mechanical-twinning system, <112>{111}, under uniaxial compressive deformation[63]. A computer-controlled, modified high-precision universal testing machine of type Zwick 1474, upgraded with gear and electronics of MTS, with high-precision extensometers (with displacement resolution of 1.2 nm), and with controlled atmosphere and elevated temperature capabilities was used for this purpose. Specifically, the [119]-oriented sample was heated to 900˚C (1173 K) and held at this isotherm for 1 hour to dissolve any ordered γ_1-phase nuclei that may have formed upon cooling of the single crystal after growth. A very small compressive load resulting in a stress of 1 MPa was applied to lock the position of the coupon during this solution treatment. The sample was then cooled to 770˚C (≈1043 K) at a rate of about 20 K/min, while maintaining the constant compressive stress of 1 MPa. After reaching the 770˚C (≈1043 K) isotherm, the compressive load was increased to produce a uniaxial stress of 12 MPa. While maintaining the constant stress of 12 MPa, the coupon was then cooled to 530˚C (≈803 K) at a rate of 20 K/min and held at this temperature for 8 hours to facilitate the stress-assisted ordering. Finally, the coupon was cooled to room temperature at a rate of 20 K/min. A first set of elastic property measurements was performed using the single crystal in the microstructural state after this stress-assisted ordering transformation, which is referred to hereafter as set I. After recording data set I from the pulse-echo overlap measurements, the crystal was exposed to an additional isothermal order-annealing treatment at 570˚C (≈843 K) in an atmosphere of purified argon for 9 days (216 h) in order to achieve further improvement in crystal quality. The elastic

properties measured for this second microstructural state of the FePd single crystal are referred to as set II in the following. The elemental composition of the single crystal was determined by a combination of X-ray energy-dispersive spectroscopy (XEDS) of large fields of view using analytical techniques of SEM and TEM as 49.9 atomic percent (at.%) Fe and 50.1 at.% Pd with a maximum statistical uncertainty of ±0.2 at.%. The quality and the lattice parameters of the single crystals were determined by XRD using a Philips X'pert diffractometer. The density, ρ, of the ordered single crystal was determined as $\rho = (9.75 \pm 0.01)$ g/cm^3 using a buoyancy method based on the Archimedes principle. The pulse-echo overlap method was employed to determine the elastic constants of the $L1_0$-ordered γ_1-FePd single crystals using an Ultrasonic Time Intervalometer Pulsing Module 5053A with transmitters V110 and V156 from Parametrics Corp., USA.

5.2 ELASTIC CONSTANTS CALCULATIONS

A large single crystal of $L1_0$ ordered FePd with equiatomic composition was prepared using a modification of the previously described elastic stress assisted solid state method[64]. The pulse-echo overlap technique was used to determine the six independent elastic constants of γ_1-FePd.

The six independent elastic constants of the equiatomic $L1_0$ ordered γ_1 FePd phase were determined in our experiments using the pulse-echo overlap technique for four different crystallographic directions. Two sets of elastic constants are reported from our measurements. Both sets were obtained from crystals of nearly identical dimensions, geometry and crystallographic direction [uvw]. However, the two single crystals used for the two different sets of measurements performed here were in two differently processed states. The first set represents the microstructure state after the initial stress-assisted ordering transformation. The second set was measured after an additional stress-free ordering treatment. The six independent elastic constants of the equiatomic $L1_0$ ordered γ_1 FePd phase determined here are compared with those measured in other studies by other researchers and with those available for TiAl.

The elastic compliances S_{ij} were calculated from the experimental results C_{ij} using the following equations[65]:

$$S_{11} = S_{22} = \frac{1}{2}\left(\frac{C_{33}}{C'} + \frac{1}{C_{11} - C_{12}}\right) \tag{11}$$

$$S_{12} = \frac{1}{2}\left(\frac{C_{33}}{C'} - \frac{1}{C_{11} - C_{12}}\right) \tag{12}$$

$$S_{13} = S_{23} = -\frac{C_{13}}{C'} \tag{13}$$

$$S_{33} = \frac{C_{11} + C_{12}}{C'} \tag{14}$$

$$S_{44} = S_{55} = \frac{1}{C_{44}} \tag{15}$$

$$S_{66} = \frac{1}{C_{66}} \tag{16}$$

$$Where\ C' = C_{33}(C_{11} + C_{12}) - 2C_{13}^2$$

In order to calculate Young's modulus for a tensile stress applied along an arbitrary [hkl] direction, according to He [66], the compliance tensor needs to be transformed. The general transformation is

$$S'_{klst} = S_{mnpr} l_{km} l_{\ln} l_{sp} l_{tr} \tag{17}$$

Where l_{km} are the direction cosines for the X-axes in the new coordinate system referred to the X_m axes in the old coordinate system.

The Young's modulus along the [100] direction is simply $E_1=(S_{11})^{-1}$. As a result the transformation can be simplified. That is why we "ch[o]se the transformation of coordinates in a way that [hkl] direction in the original coordinate system bec[a]me [100] axis in the new system." [67]

So the Young's modulus for a uniaxial stress along the [hkl] direction is $E_1^{'} = \left(S_{1111}^{'}\right)^{-1} = \left(S_{11}^{'}\right)^{-1}$ where $S_{1111}^{'} = S_{mnpr} l_{1m} l_{1n} l_{1p} l_{1r}$ where m, n, p and r running from 1 to 3, $l_{11} = \alpha, l_{12} = \beta, and\, l_{13} = \gamma$ are the direction cosines.

The equation that gives the directional cosine of the $x_1^{'}$ axis with respect to the original x axis is :

$$\alpha = \frac{ha}{\sqrt{h^2a^2 + k^2b^2 + l^2c^2}} \tag{18}$$

Where a, b and c are the lattice constants. The same expression follows for the two other direction cosines, $\beta\, and\, \gamma\, of\, the\, x_1^{'}$ axis, with respect to the Y and Z axes of the original coordinate system.

It is worth mentioning that the relationship between the abbreviated two subscript notations and the full subscript notation is:

$$S_{IJ} = S_{ijkl} \mathrm{X} \begin{cases} 1\ for\ I\ and\ J = 1,2,3 \\ 3\ for\ I\ or\ j = 4,5,6 \\ 4\ for\ I\ and\ J = 4,5,6 \end{cases} \tag{19}$$

where I=1 if (i=1,j=1) , etc; I=4 if (I=2, j=3), or (i=3, j=2).[68]

For tetragonal crystals $S_{11}=S_{22}$, $S_{13}=S_{23}$ and $S_{44}=S_{55}$ and so on:

$$S_{11}^{'} = S_{11}(\alpha^4 + \beta^4) + S_{33}\gamma^4 + 2S_{12}\alpha^2\beta^2 + 2S_{13}(\beta^2\gamma^2 + \alpha^2\gamma^2) + S_{44}(\beta^2\gamma^2 + \alpha^2\gamma^2) + S_{66}\alpha^2\beta^2 \tag{20}$$

With this equation, we can calculate the orientation dependence of a Young's modulus when the tensile direction is rotated on specific planes.

5.2.1 Young's Modulus :

5.2.1.1 YOUNG'S MODULUS FOR A TENSILE AXIS WITHIN THE (001) PLANES If Θ is the angle between [hk0] and [100], then $\alpha = \cos\Theta, \beta = \sin\Theta, and\ \gamma = \cos 90^o = 0$ and

$$S_{11}^{'} = S_{11} - \frac{1}{4}(2S_{11} - 2S_{12} - S_{66})\sin^2 2\Theta \tag{21}$$

5.2.1.2 YOUNG'S MODULUS FOR A TENSILE AXIS WITHIN THE (100) PLANES If θ is the angle between [001] and [0kl], then $\alpha=0$, $\beta= \sin\theta$ and $\gamma= \cos\theta$ and

$$S_{11}^{'} = S_{11}\sin^4\Theta + S_{33}\cos^4\Theta + \frac{1}{4}(2S_{13} + S_{44})\sin^2 2\Theta \tag{22}$$

5.2.1.3 YOUNG'S MODULUS FOR A TENSILE AXIS WITHIN THE (1-10) PLANES If the applied stress is rotated from [001] to [hkl], then $\alpha=\beta= \sin\Theta/\sqrt{2}$, $\gamma= \cos\theta$, and

$$S_{11}^{'} = \frac{1}{4}[2S_{11} + 2S_{12} + S_{66}]\sin^4\Theta + S_{33}\cos^4\Theta + \frac{1}{4}[2S_{13} + S_{44}]\sin^2 2\Theta \tag{23}$$

5.2.2 Shear Modulus :

If we will consider [HKL] is the vector normal to the (hkl) shear plane, a transformation will be made such that the [uvw] and [HKL] directions become the x' and y' axes, respectively, in the new coordinate system. In this case, the shear modulus on the (hkl) shear plane with shear stress applied along the [uvw] direction is given by

$$G = (S_{66}^{'})^{-1} = (4S_{1212}^{'})^{-1} \tag{24}$$

If $\alpha1$,$\beta1$,$\gamma1$,$\alpha2$,$\beta2$ and $\gamma2$ are the direction cosines of the [uvw] and [HKL] directions in the primitive coordinate system, for a tetragonal system, we obtain that

$$\begin{aligned} S_{66}^{'} =& 4S_{11}(\alpha_1^2\alpha_2^2 + \beta_1^2\beta_2^2) + 4S_{33}\gamma_1^2\gamma_2^2 \\ &+ 8S_{12}\alpha_1\alpha_2\beta_1\beta_2 \\ &+ 8S_{13}(\beta_1\beta_2\gamma_1\gamma_2 + \alpha_1\alpha_2\gamma_1\gamma_2) \\ &+ S_{44}[(\beta_1\gamma_2 + \beta_2\gamma_1)^2 + (\alpha_1\gamma_2 + \alpha_2\gamma_1)^2] \\ &+ S_{66}(\alpha_1\beta_2 + \alpha_2\beta_1)^2 \end{aligned} \tag{25}$$

5.2.2.1 SHEAR PLANE (001) WITH THE SHEAR STRESS DIRECTION ROTATED FROM [100] TO [010] The direction cosines are $\alpha1=\cos\theta$, $\beta1=\sin\theta$, $\gamma1=0$, $\alpha2=\beta2=0$ and $\gamma1=1$, where θ is the angle between [100] and the shear direction. By using equation (25):

$$S_{66}^{'} = S_{44}(\sin^2\Theta + \cos^2\Theta) = S_{44} \tag{26}$$

$$\text{so } G = 1/S_{66}^{'} = 1/S_{44} = C_{44} \tag{27}$$

5.2.2.2 SHEAR PLANE (100) WITH THE SHEAR STRESS DIRECTION ROTATED FROM [001] TO [010] Let the direction cosines to be $\alpha_1=0$, $\beta_1=\sin\theta$, $\gamma_1=\cos\theta$, $\alpha_2=1$,$\beta_2=\gamma_2=0$, then

$$S_{66}^{'} = S_{66} + (S_{44} - S_{66})\cos^2\Theta \tag{28}$$

5.2.2.3 SHEAR PLANE (1-10) WITH SHEAR STRESS ROTATED FROM [001] TO [110] In this case, α_1,β_1= $\sin\theta/\sqrt{2}$, γ_1= cos θ, $\alpha_2=1/\sqrt{2}$, $\beta_2=-1/2$ and $\gamma_2=0$, where θ is the angle between [001] and the shear direction. Then

$$S_{66}^{'} = 2(S_{11} - S_{12})\sin^2 2\Theta + S_{44}\cos^2\Theta = G^{-1} \tag{29}$$

5.2.3 Elastic Moduli of polycrystalline FePd , FePt and TiAl

Bulk Modulus B, Shear Modulus G and Young's Modulus E are used to describe the elastic properties of nontextured polycrystalline materials. Using appropriate averages of the Cij and Sij values for a single crystal, the B, G and E values for polycrystalline aggregates can be estimated. In this study, Hill's average was calculated from Reuss and Voigt averages.

The Reuss method averages the elastic compliances, whereas the Voigt method averages the elastic stiffness. Hill showed that these averages represent the greatest lower bound and the least upper bound respectively[69]. Therefore, he suggested that a better representation of the elastic properties of nontextured polycrystals can be obtained by using the arithmetic mean of the values calculated using Voigt and Reuss schemes.

The Voigt averages are given by [70]-[71]:

$$
\begin{aligned}
K_v &= \frac{1}{3}(A+B) \\
G_v &= \frac{1}{5}(A-B+3C) \\
E_v &= \frac{9K_vG_v}{3K_v+G_v} \\
&\textit{where} \\
A &= \frac{1}{3}(C_{11}+C_{22}+C_{33}) \\
B &= \frac{1}{3}(C_{23}+C_{13}+C_{12}) \\
C &= \frac{1}{3}(C_{44}+C_{55}+C_{66})
\end{aligned}
\tag{30}
$$

The Reuss averages are given by

$$
\begin{aligned}
K_R &= \frac{1}{3a+6b} \\
G_R &= \frac{5}{4a-4b+3c} \\
E_R &= \frac{9K_RG_R}{3K_R+G_R} \\
&\textit{where} \\
a &= \frac{1}{3}(S_{11}+S_{22}+S_{33}) \\
b &= \frac{1}{3}(S_{23}+S_{13}+S_{12}) \\
c &= \frac{1}{3}(S_{44}+S_{55}+S_{66})
\end{aligned}
\tag{31}
$$

Hill's averages are

$$K_H = \frac{1}{2}\left(K_V + K_R\right) \tag{32}$$

$$G_H = \frac{1}{2}\left(G_V + G_R\right) \tag{33}$$

$$E_H = \frac{9K_H G_H}{3K_H + G_H} \tag{34}$$

5.3 COMPRESSION TESTS

Room temperature compression tests were performed for $L1_0$-FePd single crystal samples for two different loading directions. The two samples were oriented for compression parallel to nominally [110] and [-119], respectively. The dimensions of the [110]-compression coupon were length x, width x, depth = (5.85x3.34x3.12) mm^3 and those for the [-119] -compression coupon were (6.62x3.18x2.62)mm^3.

The compression tests were performed using an electromechanical Instron Universal testing machine. Figure 19 shows schematically the set up for the compression tests. The sample was sandwiched between parallel-sided SiC disks to reduce lateral frictional forces and was placed between compression platens mounted via adapters and fixtures to the cross-bar and base of the test frame of the Instron Universal testing machine. In the absence of strain gages, the software of the computerized control system used the displacement from the electrical stepper motor as the signal to monitor the relative displacement and displacement rate of the cross-bar. The load or force was measured from the signal obtained from the load-cell of the Instron

machine. The measurements performed here should be treated with great care in any attempt to extract quantitative data from these preliminary tests, especially regarding strain. Using the original length of the sample, L_0, and a rectangular cross-sectional area of the sample, we calculated the stress and the strain and the strain rate. For example, the stress was calculated using the following equation

$$\sigma=F/A \tag{35}$$

where σ is the stress

F is the force

A is the cross-sectional area based on assumption of a rectangular cross-section.

The strain rate was obtained from the displacement rate supplied by the electrical stepper motor. The displacement rate is given by

$$dx/dt \tag{36}$$

where dx is the nominal change in the displacement of the Cross Bar and dt is the change in time. The nominal strain rate was obtained by dividing the displacement rate by the original sample length, L_0:

$$(dx/L_0)/dt \tag{37}$$

In the absence of a direct strain measurement for the sample, this approach appears reasonable for small plastic strains (L0-L/ L0 <2%). Furthermore, compression tests performed for Al-2024 coupons showed very good agreement between the displacement of the cross-heads and the actual length change of the sample (see Appendix A). The compression tests performed here cannot provide accurate experimental measures of the moduli because they are not sufficiently accurate and include all the effects of the testing frame, platens and machine in

addition to those of the small samples. Only when the dimensional changes of the sample are directly measured on the sample using strain sensors would it appear possible to obtain true stress versus true strain plots, to provide truly accurate experimental data on the elastic modulus and details of the evolution of the plastic flow stress at even larger strains. While the displacement measurements do not allow us to deduce quantitative information regarding the elastic properties of the FePd samples, these tests do provide accurate measurements of the forces resulting from the compressive loading via the load cell. Assuming that frictional forces at the interfaces between the compression coupons and the SiC disks can be neglected and that the cross-sectional dimensions of the coupons remain constant up to the onset of yielding, which appears reasonable, the tests should provide yield stress measurements. The determination of the yield stress and application of small amounts of plastic deformation were the main goals of these first compression tests. Thus, it might be possible to confirm the activity of the most highly stressed slip systems in the single crystals for the two different tests, possibly allowing estimates for the critical resolved shear stresses. Furthermore, the deformed single crystals would provide deformed microstructures, containing dislocations suitable for a first TEM study.

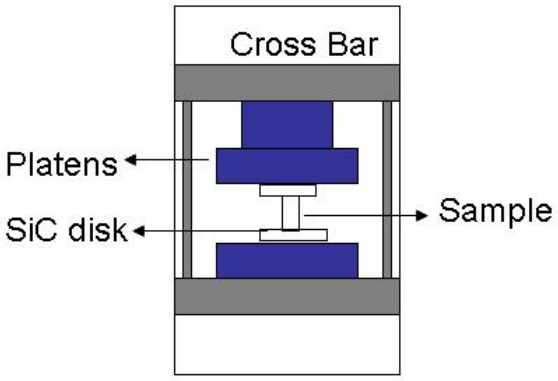

Figure 19 Schematic Draw for the Compression Test

5.4 DISLOCATION TEM IMAGE SIMULATION:

The dynamical theory of electron diffraction has been used to explain and interpret Transmissions Electrons micrographs of crystals[72] . Howie and Whelan [73] created the theory as a system of coupled first order differential equations which has shown to be useful to the calculation of diffraction contrast image of crystal defects under strong bean conditions.

This theory has been implemented in several computer programs. For example, Head[74] (1973) introduced programs for the computation of complete micrographs of dislocations and planar defects in elastically anisotropic media. These programs use the two beam theory of electron diffraction, the column approximation (CA) and linear anisotropic elasticity theory. [75]

Cu-Four is a many beam diffraction contrast simulation program that was introduced by Schaublin and Stadelmann in 1993[76]. The program is a derivative of Head [77] type program Fourdis and it has been applied for DFWB simulations. Cu Four program uses the Howie-Whelan equations[78] together with the column approximation (CA) and the generalized cross section to compute the image.

Cu Four software can image 1 to 4 dislocations and 1 to 4 associated planar faults. The simulation of two different materials in the same sample is possible via this software. Linear differential equation system describing the propagation of the electrons in the sample was developed; it allows simulating images using more than two beams. Although about 90% of the total intensity was contained in the first two beams, but the need of many beam calculation may arise in weak beam conditions when the Ewaled sphere intersects diffracted spots that are far from the transmitted spot.

To calculate the propagation of electrons in a faulted crystal, the dynamical theory [79]of contrast will be used.

The crystal at a point r is described by a faulted potential V(r) that can be written as a Fourier series :

$$V(r) = \frac{h^2}{2m_e} \sum [U_g \exp(-2\pi i\, g\, R(r)] \exp(2\pi i g r) \qquad (38)$$

Where g is the reciprocal lattice vector

M_e is the electron mass

h Planck constant

R(r) describes the displacement field around the lattice defect.

The Schrödinger's wave equation is:

$$\nabla^2\Psi(r)+\left(\frac{8\pi^2 m_e}{h^2}\right)\left[E+V(r)\right]\Psi(r)=0 \tag{39}$$

$\Psi(r)$ is the function associated to the electron wave that move through the faulted crystal. The proposed solution to the Schrödinger equation is :

$$\Psi(r)=\sum_g \varphi_g \exp(2\pi i(\chi+g+s_g)r) \tag{40}$$

Where $\varphi_g(r)$ function are associated with the beam that come out of the sample including the transmitted beam (beam 0) and the diffracted beam (beam1 to n).

The contrast intensity I recorded on the micrographs for a g image is

$$I=\varphi_g(r)\overline{\varphi_g(r)}. \tag{41}$$

χ is the direction of the transmitted beam.

g is the reciprocal lattice vector

s_g is the diviation parameter.

(χ +g + s_g) is the direction of the beam with index g. η_g is a co-ordinate along this direction.

When substituting V(r) and $\Psi(r)$ in the Schrödinger equation, a system of n differential equation of the first order with n unknown $\varphi_g(r)$ results

$$\frac{\partial\varphi_g(r)}{\partial\eta_g}\cong\sum_h\frac{\pi i}{\xi_{g-h}}\varphi_h(r)\exp(2\pi i(h-g)R(r)+2\pi i(s_h-s_g)r) \tag{42}$$

The equations are to be integrated alone the proper beam direction η_g. This is difficult to solve analytically. To simplify, the column approximation that allows to make the integration along the same direction for all beams is used. The column approximation means that we consider the direction of the transmitted beam to make the integration, so

$$\frac{\partial}{\partial \eta_g} \equiv \frac{\partial}{\partial z} \tag{43}$$

Then the equation system can be written under matrix form :

$$\frac{\partial \varphi(r)}{\partial z} = M \qquad where\ \varphi(r) = \begin{bmatrix} \varphi_0 \\ \varphi_1 \\ .. \\ ... \\ \varphi_n \end{bmatrix} \tag{44}$$

The matrix M is symmetrical and has the following expression

$$\begin{vmatrix} A & A_1 & ... & A_i & ... & A_n \\ A_1 & B_1 & & & & \\ ... & & & C_{ii} & & \\ A_i & & B_i & & & \\ & C_{ii} & & & & \\ A_n & & & & & B_n \end{vmatrix}$$

Where the coefficients are

$$A = \frac{-\xi_1}{\xi'_0}$$

$$A_i = i\xi_1 \left(\frac{1}{\xi_i} + \frac{i}{\xi'_i}\right)$$

$$B_i = \left[\frac{-\xi_1}{\xi'_0} + 2i\, s_i \xi_1 + 2\pi \frac{\partial}{\partial z}(g_i R(r))\right]$$

$$C_{ij} = i\xi_1\left(\frac{1}{\xi_{i-j}} + \frac{i}{\xi'_{i-j}}\right) \tag{45}$$

ξ_i Defines the extinction distance which becomes large if the beam I gets far from the transmitted beam, ξ_i' is proportional to ξ_1. ξ_1 is scaling factor that was originally introduced by Head to avoid convergence problems and save calculation time in the integrations.

Then $\frac{\partial\varphi_0(r)}{\partial z}$ can be calculated:

$$\frac{\partial\varphi_0}{\partial z} = -\frac{\xi_1}{\xi'_0}\varphi_0 + \ldots\ldots\ldots\ldots + i\xi_1\left(\frac{1}{\xi_i} + \frac{i}{\xi'_i}\right)\varphi_i + \ldots. + i\xi_1\left(\frac{1}{\xi_n} + \frac{i}{\xi'_n}\right)\varphi_n \tag{46 a}$$

The general equation for $\frac{\partial\varphi_i(r)}{\partial z}$ is

$$\frac{\partial\varphi_k}{\partial z} = i\xi_1\left(\frac{1}{\xi_i} + \frac{i}{\xi'_i}\right)\varphi_0 + \ldots. + i\xi_1\left(\frac{1}{\xi_{i-j}} + \frac{i}{\xi'_{i-j}}\right)\varphi_j + \ldots\ldots + \left(-\frac{\xi_1}{\xi'_0} + 2is_i\xi_1 + 2\pi i\frac{\partial}{\partial z}(g_i\, R(r))\right)\varphi_i + \ldots\ldots\ldots\ldots + i\xi_1\left(\frac{1}{\xi_{i-n}} + \frac{i}{\xi'_{i-n}}\right)\varphi_n \tag{46 b}$$

The above equations 46 show that the derivation of each beam is a linear combination of all the beams. The contribution of each beam in the linear combination is weighted bye the matrix coefficient 45.

The physical meaning of relations 46 is that the contribution of a beam i depends on the associated deviation parameter s_i (diffraction condition), the associated extinction distance ξ_i (material characteristics) and a cross term ξ_{i-j} that has the expression of an extinction distance.

High $|i|$ values correspond to large ξ_i and therefore beam i may have a weak contribution; but when this same beam has a small deviation parameter s_i ; it may have a strong contribution. It appears that the importance of a beam (i) contribution is a balance between s_i , deduced from the observation condition and ξ_i , given by the material characteristics. This had to be taken into account in the choice of the beams included in the calculation.

The general rule is the following. Beams have to be close to the transmitted beam (small ξ_i) and situated close to the Ewald sphere intersections with the systematic row (small s_i).

5.4.1 Image Simulation Parameters:

In order to do an image simulation an experimental conditions should be set. The user should input some parameter in the software in order to obtain a correct simulated image. These parameters can be divided as Materials Data, Geometry Data and Diffraction Condition Data.
The material data parameters are those parameters that specify the material type for the software. The user should input the following:

- Space Group
- Lattice Parameter
- Atomic Positions
- Elastic Constants

The Geometry Data are those parameters that set the experimental condition for the software. The user should input the following:

- Foil Normal FN
- Electron Beam Direction BD.

- Dislocation Line Direction . DD
- Burgers Vector for each dislocation. B
- Fault Plane Normal. FPN
- Lattice Translation vector R.
- Width of the plane.
- Thickness of the thin foil.

Figure (20) shows schematic drawing of the TEM sample with the geometric parameters. Note that the foil normal FN is different than the beam direction if the sample is tilted.

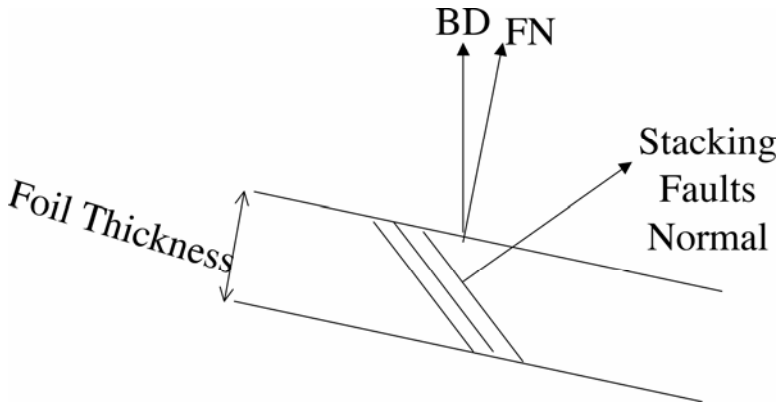

Figure 20 Schematic drawing of TEM sample.

The Diffraction Condition parameters are those related to TEM imaging like the acceleration voltage, bright field BF, dark field DF or weak beam dark field WBDF condition, the diffracted beam g, and center of the Laue circle.

5.4.2 Diffraction Contrast from Stacking Faults

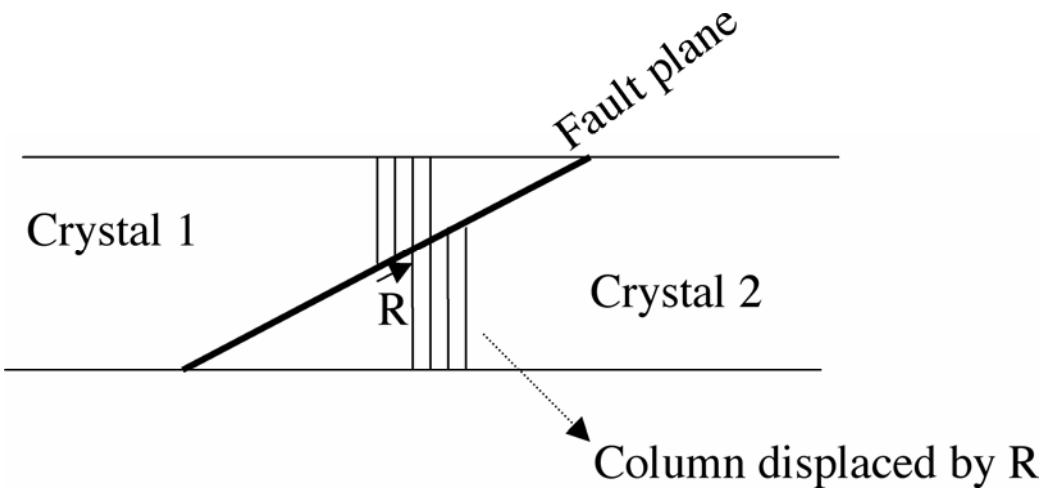

Figure 21 : Schematic draw of stacking faults in TEM foil.

Figure (21) shows a schematic of a stacking fault in a thin foil TEM sample, where the crystal above the fault is the same as that below, but translated by the vector R. The contrast of the fault is determined by the phase factor α [80]

$$\alpha = 2\pi R.g \tag{47}$$

Which changes from α=0 above the fault to $\alpha = 2\pi R.g$ below the fault. If R is a lattice translation vector, for example R=a/2<110>, the fault is invisible for all diffraction since α changes from zero to $2\pi n$ when n is an integer. When R is a partial lattice translation vector, the fault may be visible for certain values of g. The fault contrast is a set of fringes that run parallel to the intersection of the fault plane with the surface of the specimen. The relative direction between g and the fringes provides a means for interpreting the structure of the fault.

An important rule for stacking fault is that in order to a stacking fault to be visible, g.b >1/3.

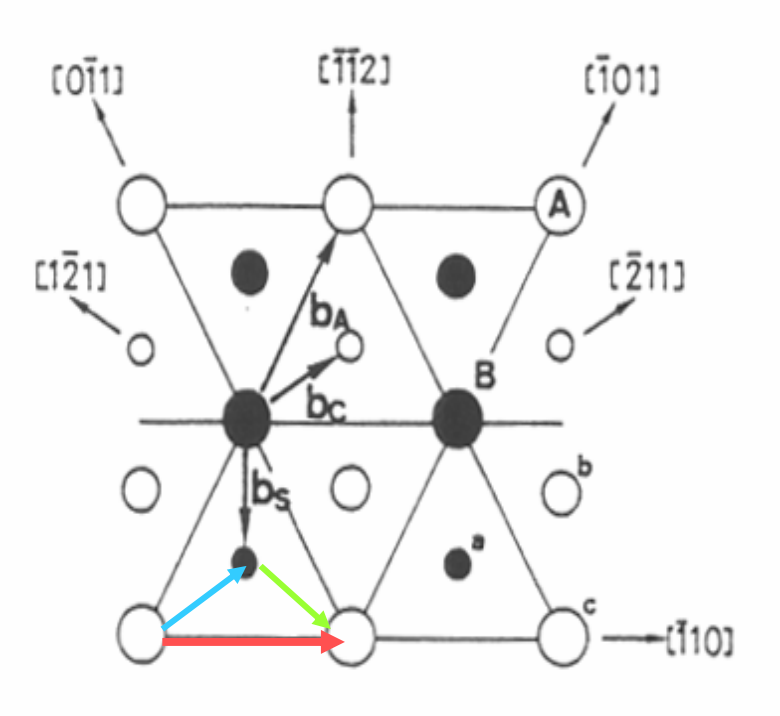

Figure 22 (111) plane in L10 system

Figure 22 shows the (111) plane in $L1_0$ system. The partial dislocations are translations in the plane of the fault, for example, it can cause a horizontal shift in this plane of a B layer into a C layer. On the other hand, atom positions across a fault can occur by a vertical displacement, like removing a B layer. Three types of stacking faults is considered in L10 system, Super intrinsic (extrinsic) Stacking Fault (SISF)(SESF), Antiphase Boundary (APB) and Complex Stacking Fault (CSF). The R vectors for these stacking faults are as the following

$R_{SISF,SESF}$ = 1/6<-1-12>

R_{APB} = ½<10-1>

R_{CSF}= 1/6<-12-1>

Since α is a phase factor, the contrast is invariant if α changes by 2π, so $\alpha = 2\pi R.g$ need to be specified in the range: $-\pi < \alpha < \pi$.

In case of $L1_0$, α can be determined as the following:

- For $R_{SISF,SESF}$ = 1/6 (-1-12), $\alpha = 2\pi \frac{-h-k+2l}{6} = \frac{1}{3}\pi(-h-k+2l)$

  a. SISF and SESF will always have a contrast in TEM images since α is a fraction of π.

- For R_{APB} = ½ [10-1], $\alpha = \pi(h-l)$.

  b. APB fringes are known as π fringes since the only contrast will appear if α have a π value.

- For R_{CSF}= 1/6 [-12-1], $\alpha = \frac{2}{6}\pi(-h+2k-l) = \frac{1}{3}\pi(-h+2k-l)$

  c. CSF fringes will be visible via TEM since a value is α fraction of π.

5.4.3 Weak Beam Dark Field:

The weak beam dark field (WBDF) imaging technique is one of the useful techniques to obtain narrow and high contrast or sharp images of dislocations lines and resolve pairs of narrowly dissociated dislocations. Dissociation separations between partial dislocations in ordered alloys are often too small to be discerned with conventional or strong beam electron microscopy. Conventional strong beam dislocation images often exhibit image peak widths on the order of 10nm to 20nm, while narrow dissociation widths on the order of 1-5nm are quite typical for partial dislocation pairs in intermetallics [81]. Using WBDF microscopy reduces the image peak width of the dislocations down to about 1-2nm enabling the resolution of such narrowly dissociated superpartial dislocations.

In WBDF imaging, the crystal is tilted to a large deviation away from the exact Bragg or diffraction condition for the set of planes {hkl} represented by the diffraction vector g_{hkl} used for imaging. A positive value of the geometric deviation parameter, s_g, is preferred. For such imaging set up the diffraction is weak and the DF image is quite dark or very weak over most of the crystal. Only near the core of the dislocation are the strains large enough to bend or distort the crystal planes sufficiently to produce a small volume of crystal near the dislocation that is satisfying the Bragg or diffraction condition with s~0. The WBDF image shows the diffraction from these severely bent planes near the core of dislocation and correspondingly is narrow and weak in intensity resulting in improved resolution for imaging of the strain fields of the dislocation

The procedure to obtain a WBDF image can be summarized as follows:

a. Orient the specimen in a good two-beam condition and excite an appropriate diffraction vector +g in a systematic row without significant excitation of any other diffractions.

b. Tilt the incident electron beam until the position of the vector +g moves into the position of the transmitted beam. Now the diffraction vector +g becomes weak, so it is called 'the weak beam'. After this tilt of the incident beam, the transmitted beam has moved and the strong diffraction spot is now the 3g spot. This is called g-3g WBDF condition.

c. The DF image is formed by placing the objective aperture around the +g spot.

d. By varying the imaging conditions different WBDF conditions of the type g-ng, where n denotes the intersection of the Ewald Sphere with the systematic row of g, can be realized to optimize the dislocation image contrast. Typically, the larger the magnitude of n is, the larger is the magnitude of the deviation parameter sg for the image forming beam g, which results in a reduced intensity in the image and a concomitant reduction in the image peak width of the dislocation image. Hence, a compromise has to be established experimentally or empirically to establish the best or optimal imaging condition for a given dislocation configuration and imaging geometry.

5.4.3.1 REQUIREMENT OF WEAK BEAM MICROSCOPY Cockayne [82] had established certain criteria which have to be satisfied to obtain high resolution DFWB images of dislocations for 100 KV, these criteria can be summarized as the following:

a. Geometrical deviation $|s_g| > s_{crit} > 0.2\,nm^{-1}$

b. Dynamical Deviation $|w_g| = s_g \xi_g > 5$

c. No other beams near their respective Bragg positions, i.e. no other reflections significantly excited.

d. Use g.b <2

Criterion a controls the fringe spacings and the image width of strain contrast images obtained with the weak diffracted beam g, whereas criterion b should be satisfied in order to minimize the interaction of the weak g beam with the strong transmitted O beam. These two requirements for WB-TEM only apply to the imaging diffracted beam g and the transmitted O-beam, thus they can be regarded essentially as two-beam criteria. Satisfaction of criterion c will prevent the interaction of the weak g-beam with other diffracted systematic and non systematic beams. Criterion c provide the complication of image interpretation by multiple peak from a single dislocation which can occur for larger values of g.b

6.0 RESULTS AND DISCUSSIONS

6.1 PREPARATION AND CHARACTERIZATION TO L10 FEPD SINGLE CRYSTAL

6.1.1 XRD

After the initial stress assisted ordering transformation, XRD confirmed the $L1_0$-ordered crystal structure of the single crystal. The quality of the γ_1-FePd single crystals had improved significantly after the additional isothermal stress free ordering treatment for 216 hours at 570 C [843 K]. The experimentally determined lattice parameters for the tetragonal phase are, $a_o=b_o=0.3847+/- 0.0001$ nm and $c_o= 0.3726 +/-0.0001$ nm. These are in excellent agreement with the values reported in literature.[83] Figure 23 shows the XRD for the FePd sample before the additional heat treatment and after the additional heat treatment. Strong superlattice intensities are observed for the 110 sets of planes from the nominal {110}-type face of the crystal coupon for both processing conditions. However, the stress-free additional heat-treatment resulted in further reduction of internal stress (narrower peaks, e.g doublet from k-α-splitting is discernible) and eliminated the intensity in the 202/022 reflection, which is related to the presence of a residual fraction of the wrong orientation variant L1o-phase after the initial stress-assisted ordering heat treatment.

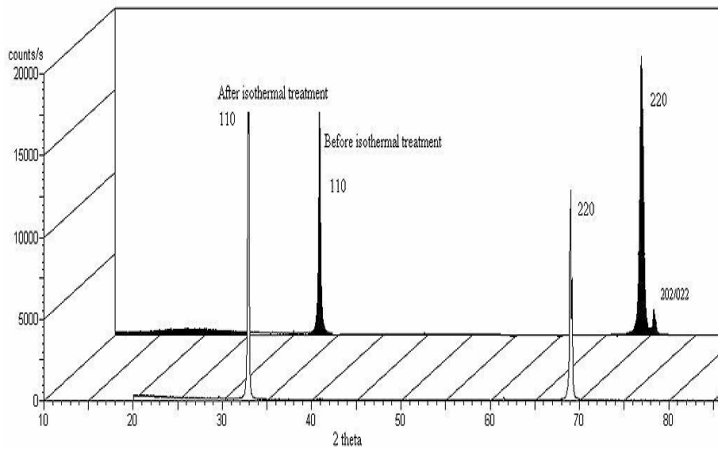

Figure 23 : XRay-diffractograms obtained from the (-110)-surface using Cu-Kα radiation for the single crystal prior to ("Before isothermal treatment") and after ("after isothermal treatment") the additional stress-free order-annealing at 570^{o}C for 216h.

6.1.2 VSM Measurements:

The magnetic properties of the FePd single crystal were measured at room temperature by Vibrating Sample Magnetometry (VSM). The magnetization, M, versus applied magnetic field, H, curves (M-H-curves), were obtained for application of the external magnetic field, H, parallel to different crystallographic directions of the tetragonal $L1_o$-structure with 'easy' magnetization axis parallel to [001]. The M-H-curves for the as received sample are shown in Figure 24.

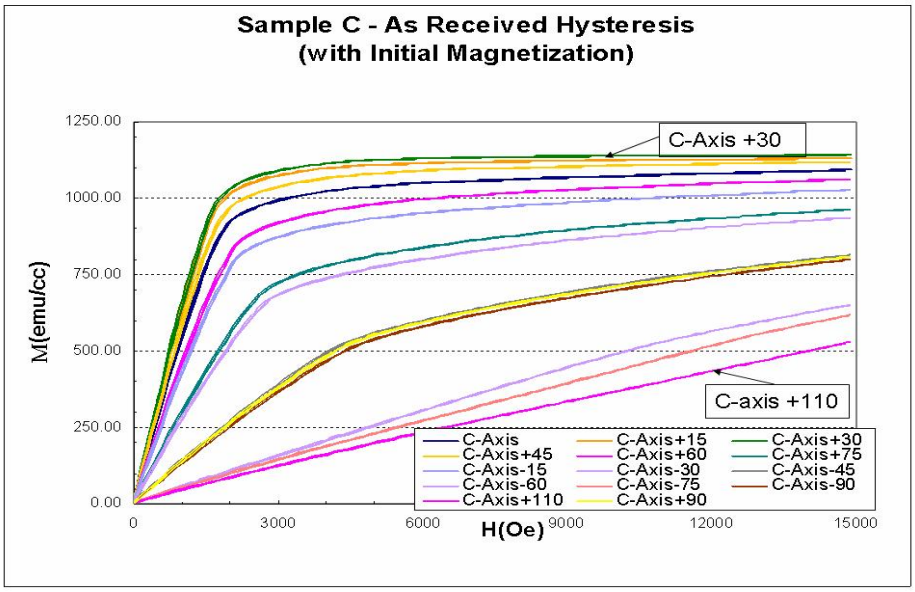

Figure 24 : The M-H-curves for the as received sample

The coercivity, H_C, is no larger than about 20 Oe and the remnant magnetization is neglible. The 'easy direction' of magnetization is shifted by 30° from [001]. A TEM study of this sample revealed the presence of polytwinned bands and mechanical {111} twins. Hence, it was concluded that this sample did not represent a good quality single crystal of $L1_o$-FePd for the measurement of intrinsic magnetic properties. An additional heat treatment was applied to this sample in a stress free condition to eliminate the {101} polytwins, assuming that coarsening of the dominant orientation variant of the $L1_o$-phase would coarsen at the expense of the unwanted orientation variant(s) in the polytwinned bands, which represented the minor volume fraction. Sample B was annealed to 96 hours at temperature T~850 K. The M-H-curves for sample B are shown in Figure 25. It is clear that the 'easy direction' is observed along [001] and that the 'hard direction' is observed at 90° from [001], i.e. along [-110] in the (110)-plane. The coercivity and the remnant magnetization are minimal again.

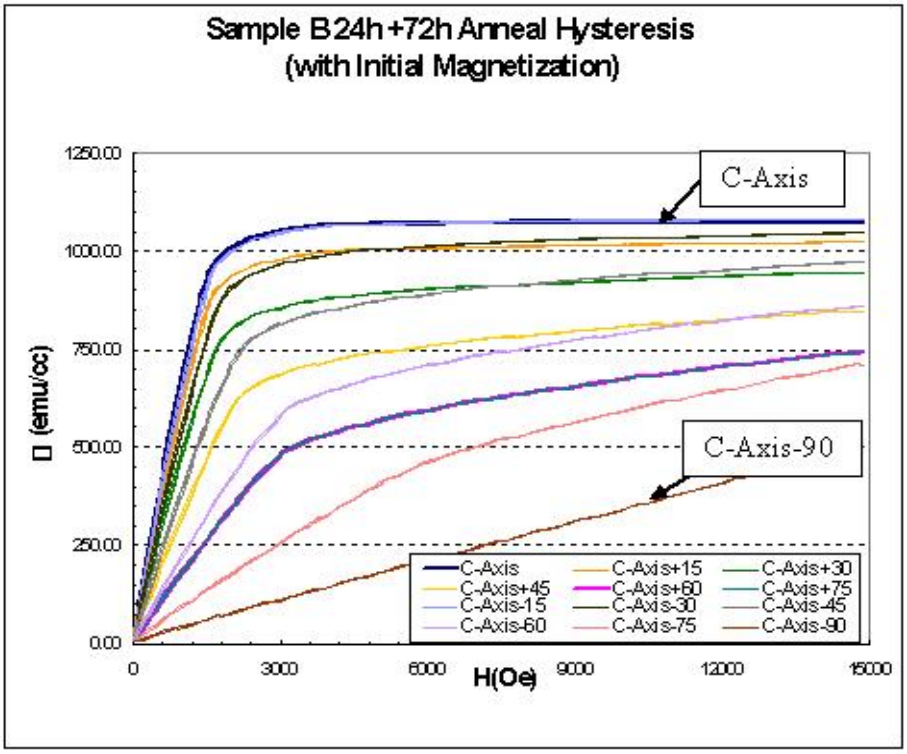

Figure 25: The M-H-curves for sample B

In conclusion, mono-variant single crystals of L1o-FePd have low coercivity and minimal remnant magnetization. The 'easy magnetization' axis is along [001], while the hard axis is 90^{o} from [001]. The presence of polytwinned volume fraction affects the magnetic behavior of the single crystal by changing the effective or apparent easy and hard axes directions. However, the presence of the small amount of polytwinned material did not significantly affect the magnitudes of some important intrinsic properties, such as the anisotropy constant, saturation magnetization and the estimated anisotropy field or switching field H_A.

Shima, Oikawa, et al.[84] previously calculated the anisotropy constant K_u for $L1_0$ FePd as Ku=1.7 x 10^7 ergcm^{-3} at room temperature. Here, the anisotropy constant was determined to be Ku= 1.77 x 10^7 ergcm^{-3}. Table 1 presents the values of anisotropy constant Ku, saturation magnetization M_S and H_A for $L1_0$ equiatomic FePd that were obtained from the present study for

both cases (with the small fraction of polytwins in the microstructure set I, and for the mono-variant set II) and the values obtained in previous work by Shima's group (reference [84]) at a temperature of 4.2 K.

Table 1 Values of Anisotropy constant Ku, Saturation Magnetization Ms and HA.

	Ku $ergcm^{-3}$	Ms $emu\ cm^{-3}$	Ha kOe
FePd (set I) With the polytwins	1.83×10^7	1140	32.2
FePd (set II) Mono-variant	1.77×10^7	1080	32.1
FePd at 4.2 K [85]	2.5×10^7	1190	36

Given the very good quantitative agreement with previous measurements of the VSM measurements performed here, it seems reasonable to conclude that the FePd single crystals prepared for this study were of good quality.

6.2 ELASTIC PROPERTIES OF $L1_0$ FEPD

The Elastic Constants of the tetragonal $L1_0$ phases describe the intrinsic elastic properties of the $L1_o$-FePd. Details of the dislocations fine structure, such as the details of dissociations and decompositions of dislocations and the relevant planar fault energies, are determined by the elastic constants. Also, the elastic constants are required for both the computer image simulations of WBDF TEM images of narrowly dissociated dislocation configurations. This section will discuss and compare the influence of elastic properties on the plastic deformations behavior and the role of possible anisotropy of interatomic bonding of both γ_1 FePd, FePt and γ-TiAl.

A large single crystal of $L1_0$ ordered FePd with equiatomic composition has been prepared by a modification of the previously described elastic stress assisted solid state method[86]. The pulse-echo overlap technique has been used to determine the six independent elastic constants of γ_1-FePd.

Table [2] shows the six independent elastic constants of the equiatomic $L1_0$ ordered γ_1 FePd phase determined here together with previously reported values. The six independent elastic constants are determined from pulse-echo overlap technique for four different crystallographic directions in our experiments. Two sets of elastic constants are reported from our measurements. Both sets were obtained from crystals of nearly identical dimensions, geometry and crystallographic direction [uvw]. However, the two single crystals used for the two different sets of measurements performed here were in two differently processed states. The first set represents the microstructure state after the initial stress assisted ordering transformation. The

second set was measured after additional stress free ordering treatment. Also the six independent elastic constants of the equiatomic $L1_0$ ordered γ_1 FePd phase determined here are compared with those measured in other studies by other researchers and with those available for TiAl.

Table 2 Stiffness constants for FePd, FePt and TiAl .

T≈300K	c_{11} [GPa]	c_{33} [GPa]	c_{12} [GPa]	c_{13} [GPa]	c_{44} [GPa]	c_{66} [GPa]	c_{44}/c_{66}	A_1	A_2	A_2/A_1
γ_1-FePd, I this study, stress-transformed	213.6 ±3	226.5 ±3	143.0 ±3.5	143 ±9	91.5 ±0.7	92.7 ±4	0.99 **±0.05**	2.63	2.38	0.90
γ_1-FePd, II this study, + 216h @ 570˚C	**212.7 ±3**	**224.5 ±3**	**141.6 ±3.5**	**146 ±12**	**91.9 ±0.7**	**98.8 ±4**	**0.93 ±0.05**	**2.78**	**2.53**	**0.91**
γ-(Fe,Pd)[87]	215.0		161.0		83.2			3.08		
γ1-FePd, Average of [88]	222.0	232.5	151.0	152.5	92.2	95.2	0.97	2.68	2.47	0.92
FePt [89]	304.2	242	222.6	197.3	106.5	40.8	2.6	1	2.8	2.8
γ-TiAl,[90]	186.0	176.0	72.0	74.0	101.0	77.0	1.31	1.35	1.89	1.40
γ-TiAl,[91]	183.0	178.0	74.1	74.4	105.0	78.4	1.34	1.44	1.98	1.38

For both microstructural states of the γ_1 FePd crystals studied here, before and after the additional heat treatment, the elastic constants agree within the error margins. It is interesting to

note that error margins are not available for the previously reported data. The absolute differences between the C_{ij}'s measured in the two separate data sets are minimal for C_{44} , 0.4 GPa, and at maximum for C_{66} ,3.1 GPa. The insufficient precision in the measurements of C_{66} limits any further discussion of possible effects of the microstructural changes in the FePd samples after the additional heat treatment on the elastic constants and the tetragonal anisotropy. However, it was noticed that the value of C_{44} remains constant, while that of C_{66} appears to increase after the stress free heat treatment. The deviation of elastic properties from the symmetry of cubic materials can be expressed by the deviation of the ratio (C_{44}/C_{66}) from unity. The ordered γ_1 FePd exhibits no significant deviation of elastic properties from the symmetry of cubic materials, $C_{44}/C_{66} = 0.99 \pm 0.04$ set I , before the additional stress free order annealing. After the additional order-annealing a pronounced non cubic elastic behavior is found $C_{44}/C_{66} = 0.93 \pm 0.04$ for set II. The orientation variants $L1_0$-II and $L1_0$-III and other crystal defects, like twins and APB's, reduce the magnitude of the uniaxially anisotropic elastic properties measured for bulk single crystal of the tetragonal γ_1 FePd phase. This leads to the conclusion that it is important to eliminate even relatively small volume fractions (3.9%) of errand $L1_0$ orientation variants to investigate the uniaxial anisotropic elastic properties of the tetragonal γ_1 FePd accurately.

The microstructural studies showed (e.g XRD Figure 23) that the additional stress free order annealing produced a single crystal of better quality. Hence, dataset II will be used to compare the elastic constants of equiatomic $L1_0$ γ_1 FePd with those reported previously for γ_1 FePd and γ-TiAl. The elastic constants determined here for equiatomic γ_1 FePd using pulse-echo overlap method agree with those deduced from the RPR (RUS) measurements and confirm

the basic conclusion of[92] regarding the deviation of γ_1 FePd from cubic symmetry In FePd, the parameters $C_{11}<C_{33}$ and $C_{44}<C_{66}$. This is in the opposite sense to the case of γ TiAl and is consistent with the (c/a) ratio of the relevant tetragonal unit cell. Also it is in the opposite sense to the case of FePt which has c/a <1 similar to FePd. Hence, based on the theoretically computed elastic constants available for FePt, the FePt acts elastically more like γ-TiAl than FePd, which is surprising. The tetragonal anisotropy parameters $A_1=2C_{66}/(C_{11}-C_{12}) = 2.78 \pm 0.14$ and $A_2=4C_{44}/(C_{11}+C_{33}-2C_{13}) = 2.53 \pm 0.40$ deviate considerably from unity, indicating substantial elastic anisotropy for γ_1-FePd. The magnitude of the elastic anisotropy of some ductile FCC metals (e.g. $A= 2C_{44}/(C_{11}-C_{12}) =2.90$ for Au, A=2.51 for Ni) is similar to the elastic anisotropy of γ_1-FePd. C_{44}/C_{66} is a parameter which describes the elastic tetragonality, in γ_1-FePd $C_{44}/C_{66} = 0.93 \pm 0.04$. This implies that the shear stiffness along [100] is smaller in (001) than in (010).

6.2.1 Comparison of Young's modulus for FePd, FePt and TiAl

The dependence of the Young's, E, and Shear, G, modulus on the crystallographic direction have to be determined in order to compare the elastic properties of γ_1-FePd measured here with the experimentally determined elastic properties reported before for γ TiAl and the theoretically computed elastic constants for FePt .Table [3] shows the values of elastic compliances S_i

Table 3 Compliances, sij, in 10-11 Pa-1for 1-FePd from data set II in Table 2.

	s_{11}	s_{33}	s_{12}	s_{13}	s_{44}	s_{66}
γ_1-FePd	**1.008**	**0.960**	**-0.399**	**-0.396**	**1.088**	**1.002**

According to He[93], the compliance tensor needs to be transformed in order to calculate Young's modulus for a tensile stress applied along an arbitrary [hkl] direction. The details of this transformation are in section 5.2.

6.2.1.1 YOUNG'S MODULUS FOR A TENSILE AXIS WITHIN THE (001) PLANES

The variation of the Young's Modulus in the (001) plane for quadrant of directions [uvw] between [100] , $\Theta = 0$,and [010], $\Theta = 90^o$ is shown in figure 26a.

FePd exhibits a maximum of $E_{[uv0]}$ for [110] where E_{max}=180.2 GPa, and minimum for [100], E_{min}=99.2 GPa

Comparing the Young's modulus values in (001) in FePd and TiAl , both of them exhibit anisotropy but this anisotropy is more pronounced in FePd. The ratios E_{max}/E_{min} are for FePd 1.82 and for TiAl 1.24. Young's modulus values in (001) in FePt are constant in all directions.

6.2.1.2 YOUNG'S MODULUS FOR A TENSILE AXIS WITHIN THE (100) PLANES

The orientation dependence of Young's modulus on the (100) plan is plotted in Figure 26 b. For FePd $E_{[001]}$=104 GPa, $E_{[010]}$=99.2 GPa and $E_{[011]}$=177 GPa. Both FePd ,FePt and TiAl exhibit the same variation of Young's modulus qualitatively. The magnitude of Young's modulus of FePd in (100) plane is systematically smaller than that of TiAl and FePt.

6.2.1.3 YOUNG'S MODULUS FOR A TENSILE AXIS WITHIN THE (1-10) PLANES

The behavior of Young's modulus in (1-10) plane is similar for the quadrant of directions [uuv] between [001] and [110] in both phases with minima of $E_{[uuv]}$ for [001]. For FePd the maximum young's modulus in [1-10] plane is at [111] with $E_{[111]}$=238 GPa, while for TiAl the maximum value of E is at direction very close to [111] but deviating from it toward [001].[94] Young's Modulus values for (1-10) for FePt behave in the same mannar as FePd and TiAl .

From the figure 26c, it is clear that FePd exhibits a larger anisotropy regarding Young's modulus E[uuv] than TiAl and FePt. The hierarchy of Young's modulus as function of direction [uvw] in γ_1-FePd is

$E_{[111]}>E_{[110]}>E_{[011]}>E_{[001]}>E_{[100]}$

This is different from that of FePt and γ-TiAl

$E_{[111]}>E_{[011]}>E_{[110]}>E_{[100]}>E_{[001]}$

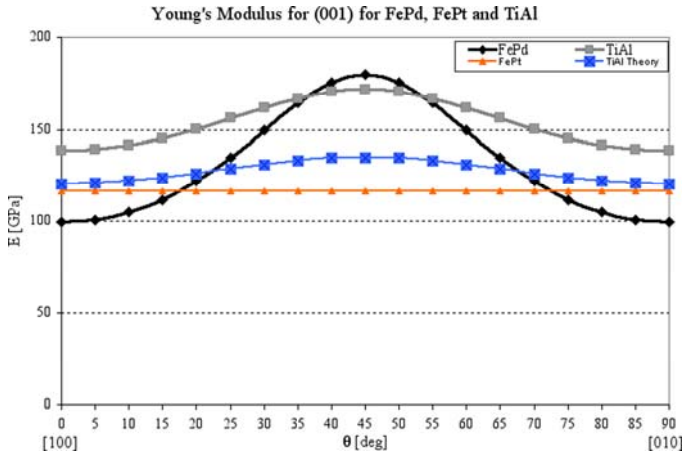

a.

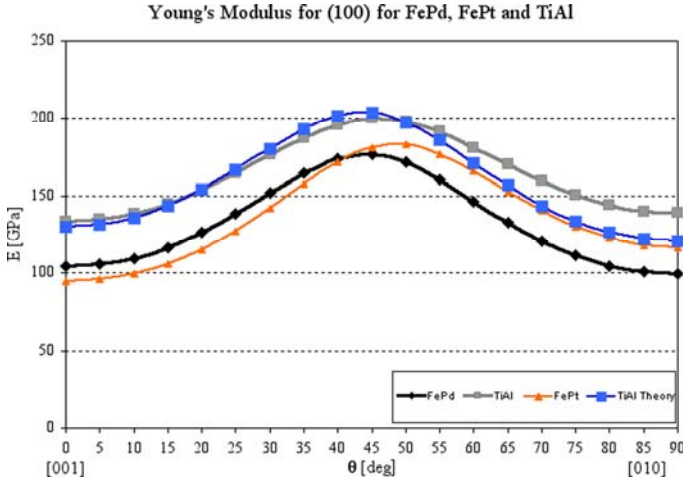

b.

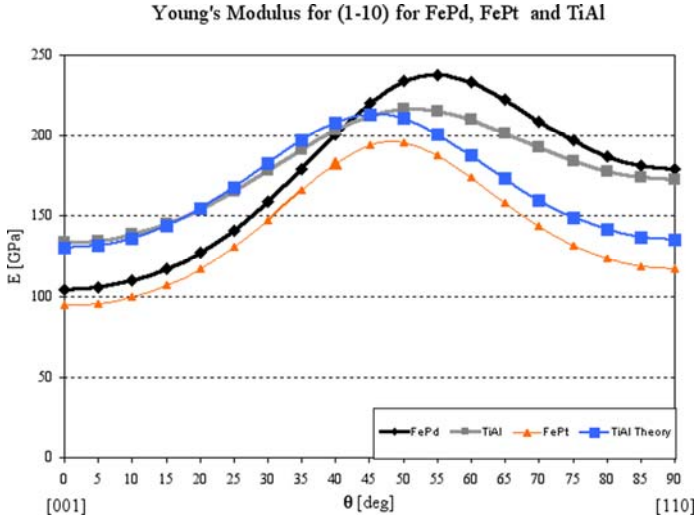

c.

Figure 26 : Plots of Young's modulus, E, for different crystallographic directions and planes in FePd FePt and TiAl E(001) between [100],θ=0^{o}, and [010], θ=90^{o} ; b) E(100) between [001] and [010]; c) E(1-10)) between [001] to [110].

6.2.2 Comparison of Shear Modulus for FePd, FePt and TiAl:

To understand plastic deformation in γ-FePd, it is useful to study the dependence of the shear modulus on stress directions. Similar to the process with Young's modulus, a shear plane (hkl) was chosen and the shear stress direction [uvw] was varied within that plane. The equations that were used to calculate the shear modulus are in section 5.2.2

6.2.2.1 SHEAR PLANE (001) WITH THE SHEAR STRESS DIRECTION ROTATED FROM [100] TO [010] In both TiAl and FePd, the shear modulus in the (001) plane is independent of the shear stress direction [uv0]. The value of the shear modulus for FePd in the (001) plane is G(001)FePd =92 GPa , in FePt G (001) = 106.5 Gpa, and it is 103.5 GPa in TiAl. That means it is easier to shear this plane in FePd as compared to TiAl and FePt. Figure 27a shows the shear modulus G in the (001) for both FePd and TiAl.

6.2.2.2 SHEAR PLANE (100) WITH THE SHEAR STRESS DIRECTION ROTATED FROM [001] TO [010] Figure 27b shows the shear modulus G in the (100) plane. For FePd the maximum shear modulus is about 99.8 GPa along [010] and the minimum is about 91.8 GPa along [001]. For TiAl, the minimum is about 76.5 GPa for [010] and the maximum is about 103.5 GPa for [001]. For FePt , the minimum is about 40.8 GPa for [010] and the maiximum is about 106.5 GPa for [001].

For FePd, the shear modulus varies by about 8% for the directions [0vw] between [001] and [010] while it varies by about 26% in TiAl. The anisotropy is the reverse in FePd and TiAl.

From Figure 27(a) it is clear that FePd is harder to shear along [011] in (100) than TiAl, which may have implications for SD's with Burgers vectors parallel to [011].

6.2.2.3 Shear plane (1-10) with shear stress rotated from [001] to [110] Figure 27 c plots the variation of the shear stress in the (1-10) plane for both TiAl and FePd. Both phases behave qualitatively the same regarding the variation of the shear modulus with directions in the dodecahedral plane (1-10) but with quantitatively symmetrically smaller values for FePd. That means it is easier to shear FePd in the (1-10) plane than TiAl.

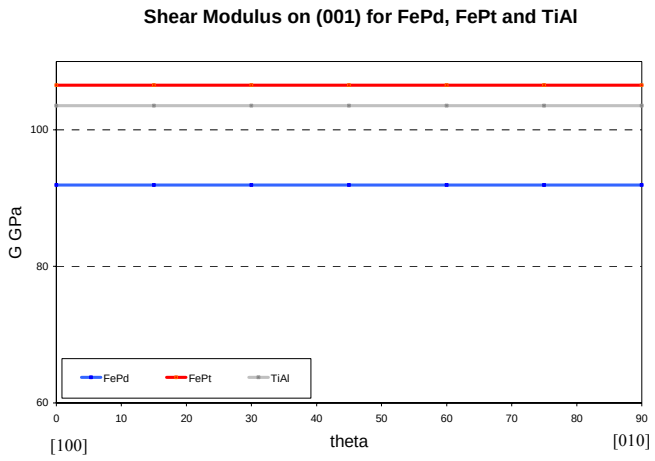

a.

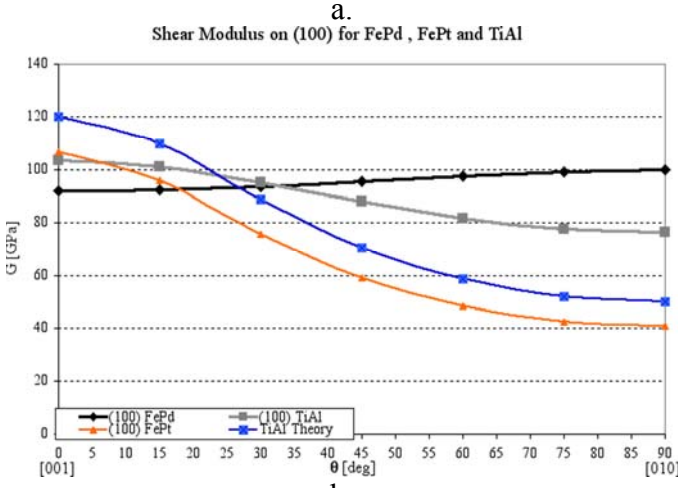

b.

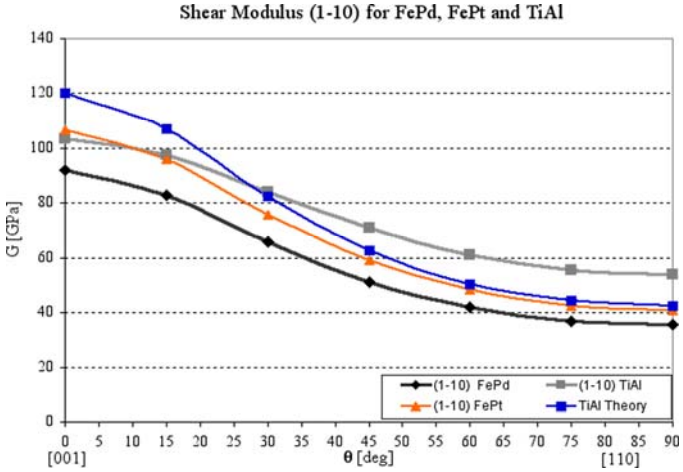

C

Figure 27 Shear modulus, G, as function of direction in various planes for FePd and TiAl. a) G(001) from [100], $\theta=0^{o}$,to [010] ,$\theta=90^{o}$, b) G(100) from [001],$\theta=0^{o}$,to [010]] ,$\theta=90^{o}$, and c) G(1-10) from [001] ,$\theta=0^{o}$ to [110] ,$\theta=90^{o}$.

6.2.2.4 SHEAR PLANE (111) The plastic deformation in both FePd, FePt and TiAl is achieved by the glide of dislocations and/or mechanical twinning in {111}, the octahedral plane. Perfect dislocations with three different types of Burgers vectors can be distinguished in the L1o-structure. In $L1_0$ structure perfect dislocations in {111} can be ordinary dislocations with a Burger vector b=1/2<110>, super dislocations with a Burgers vector b=<101> and twin dislocations with a Burgers vector b=1/2<112>. Thus, it is useful to study the variation of the shear modulus G(111)[uvw] in the octahedral glide plane (111) for different directions [uvw] between [-110] and [-1-12]. For experimental data sets for TiAl ,FePt and our data from set II for FePd, the dependence of the shear modulus in the octahedral plane for TiAl and FePd is shown in Figure 28, revealing anisotropic behavior of $G_{(111)[uvw]}$ for both. This anisotropic behavior is in opposition. For TiAl and FePt, the minimum shear modulus is observed along [-1-12] and the maximum along [-110], while for FePd a minimum appears for [-110] and the maximum for [-1-12]. Also the magnitudes of the corresponding shear moduli $G_{(111)[uvw]}$ are systematically smaller for FePd than for TiAl .

This means that it is harder to shear TiAl in the (111) plane along each of the four directions, [-110], [-211] , [10-1] and [11-2] than FePd. For FePd in the (111) plane, it is easier to shear along the direction [-110] and increasingly more difficult as the shear direction tends towards [-1-12], i.e., $G_{(111)[-110]}<G_{(111)[-101]}<G_{(111)[-1-12]}$ for FePd. For TiAl and FePt, the opposite is true – it becomes increasingly more difficult to shear as the direction moves the opposite way: $G_{(111)[-110]}>G_{(111)[-101]}>G_{(111)[-1-12]}$. However, while this might imply for FePd that octahedral OD glide is favored over glide by an SD, and in particular a full perfect TD, it must be noted that the overall anisotropy of the shear modulus in the (111) plane is not very large. For TiAl, the absolute value

of the anisotropy is not very large either. The critical resolved shear stress of a dislocation in the (111) plane is approximately proportional to the product of the shear modulus in the direction of the Burgers vector and the magnitude of the Burgers vector. Given the relatively small magnitude of the anisotropy of $G_{(111)[uvw]}$, the differences in magnitude of the Burgers vector for OD's, SD's and TD's, would appear to be dominant when considering relative critical resolved shear stresses that may be expected for the three different possible octahedral glide systems. For FePd, OD's have the shortest Burgers vector of the three units or perfect dislocations considered here and the smallest shear modulus in the close-packed planes is associated with their Burgers vector directions. Hence, it seems reasonable to predict that for FePd, octahedral glide of OD's is associated with a smaller critical resolved shear stress than either glide of SD's or TD's, which would be consistent with the experimental observations of easily activated OD glide in polycrystalline FePd. However, effects from the core structure and dislocation dissociation fine structure seem to be very important when attempting to analyze critical resolved shear stresses and glide behavior of the three different perfect dislocation glide systems in $L1_0$-phases in attempts to rationalize plastic behavior. Comparing the values of $G_{(111)[uvw]}$ of TiAl and FePd for identical directions corresponding to shears of possible OD's, SD's and TD's in the (111) plane, it is noted that $G_{[-110]\text{-TiAl}} \approx 1.43\ G_{[-110]\text{-FePd}}$, $G_{[-101]\text{-TiAl}} \approx 1.32\ G_{[-101]\text{-FePd}}$ and $G_{[-1-12]\text{-TiAl}} \approx 1.29\ G_{[-1-12]\text{-FePd}}$. Clearly, TiAl is significantly harder to shear in (111) along each of these directions than FePd, particularly for [-110].

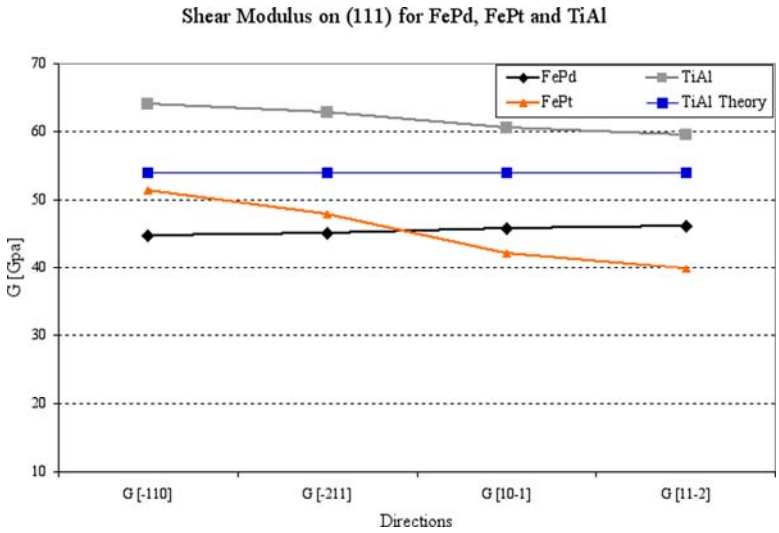

Figure 28 Shear modulus, G, in the octahedral plane (111) for directions between [-110] and [-1-12] for FePd and TiAl.

6.2.3 Elastic Moduli of polycrystalline FePd and TiAl

Bulk Modulus B, Shear Modulus G and Young's Modulus E are used to describe the elastic properties of nontextured polycrystalline materials. By appropriate averages of the C_{ij} and S_{ij} values, for the single crystal, the B, G and E values for polycrystalline aggregate can be estimated.

Poisson's ratio, ν_H, is simply $E_H/2G_H$-1. Table [4] shows the values of Hill's averages of the bulk (B_H), shear (G_H) and Young's (E_H) modulus and Poisson's ratio, ν, for γ_1-FePd (from data set II in Table [2]) and for FePd ,FePt and TiAl from previous reports. All data are for the $L1_0$-phase at room temperature.

Table 4 Hill's averages of the bulk (BH), shear (GH) and Young's (EH) modulus and Poisson's ratio, , for FePd, FePt and TiAl

Material; reference	B_H [GPa]	G_H [GPa]	E_H [GPa]	Poisson's ratio, ν
γ_1-FePd, this work	**168.15**	**63.68**	**169.6**	**0.33**
γ_1-FePd [95]	178.0	65.1	174.0	0.337
γ_1-FePd [[96]	172.0	63.3	169.0	0.336
FePt [97]	227.7	59.2	163	0.38
γ-TiAl, [98]	110.0	74.0	181.5	0.23
γ-TiAl, [99]	111.2	75.1	183.90	0.22
γ-TiAl [100]	110.2	74.53	182.46	0.22

Non-textured polycrystalline γ_1-FePd exhibits a Poisson's ratio ν=0.33, which compares well with the Poisson's ratio for some similarly elastically anisotropic and ductile FCC metals, e.g. Al (0.34), Cu (0.34) and Ni (0.31) [Kelly and Groves] while polycrystals of γ-TiAl exhibit a much smaller Poisson's number, ν=0.22. This would appear to be in agreement with the apparently better ductility of FePd compared with single phase TiAl. While the shear anisotropy parameters, A_1 and A_2, are smaller for TiAl than for FePd, the relative deviation from behavior that may be expected for an equivalently elastically anisotropic crystal with cubic symmetry as expressed by the deviation from unity of the ratios of c_{44}/c_{66} and (A_2/A_1) is larger for TiAl. This apparently less 'cubic' behavior of TiAl correlates with the frequently reported lack of ductility and limited fracture toughness of polycrystalline TiAl.

6.3 COMPRESSION TESTS

6.3.1 Sample I

This sample dimension of (5.85x3.34x3.12 mm) and orientation are shown in Figure 30. The compression test was performed at room temperature with an apparent or nominal strain rate of 0.0017/s.

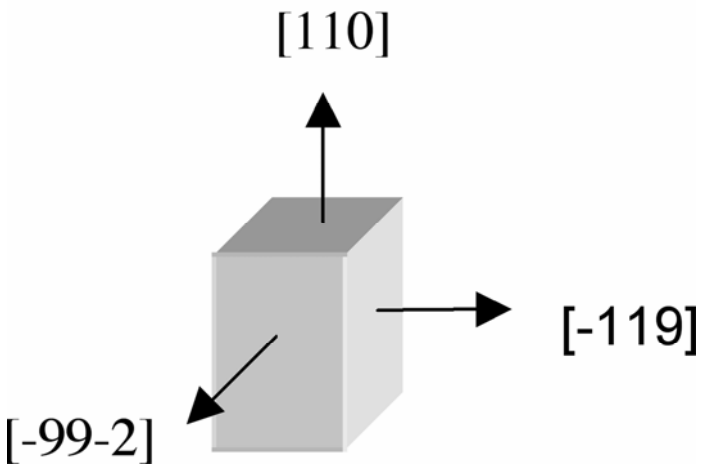

Figure 29 Sketch of FePd Single Crystal coupon

For this sample a first loading was performed as test [A], where a maximum load was applied to reach a maximum nominal stress of up to 375 MPa. The test was stopped at his maximum nominal stress, since a change of the slope of the loading curve was observed for nominal stress

just larger than 150 MPa. This was interpreted initially as plastic yielding and that significant plastic flow occurred up to the maximum stress of 375MPa (e.g. Fig 30). Measuring the length of the sample after unloading revealed that it was 5.85 mm, i.e., there was no change in the sample length, indicating that the sample did not plastically deform significantly enough to have reached its yield stress value. Thus, this first test actually represented only elastic loading of the sample despite the discernible slope change. This may be attributed to realignments in the machine-sample assembly (Fig. 31).

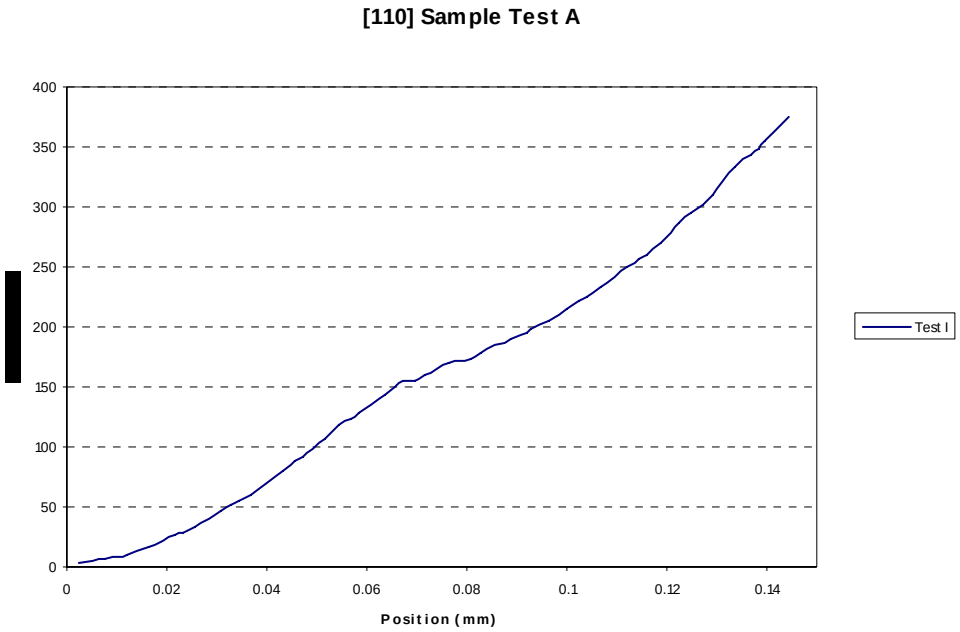

Figure 30 Stress vs. Position curve for test A

One could raise the argument that the length of the sample could have been changed by a small amount, too small to be measured by the micrometer. However, this is unlikely, since the total displacement measured between the apparent yielding at about 0.065mm and the end of the test at a displacement of 0.145mm of about 0.080mm=80 microns is well within the accuracy of the

length measurement using the micrometer. Nevertheless, assuming that a micro-yielding event occurred, the yield strength at 0.2% offset is determined by finding the intersection of the stress-strain curve with a line parallel to the initial slope of the curve and which intercepts the x- axis. The following procedure was used to attempt determination of the 0.2% yield stress value:

- Drawing a line that has the average approximate slope of the Stress vs. dx/L0 curve in the elastic region and in (Line 1 in figure 32). The line 1 intercept with the x-axis defines the actual origin for measurement of possible permanent length changes of the sample.
- Drawing another line parallel to line 1 but displaced to the right by the appropriate strain, change in x-position, delta x, divided by the initial sample length, L_0, of value 0.002. This second line, line 2, should intercept the x-axis at a value equal to 0.002, larger than the x-axis intercept of line 1.
- The intersection of line 2 with the Stress-curve is the 0.2% yield stress.

Hence, as is depicted for the Stress vs delta x/L_0 curve shown in figure 32, there is no intersection between line 2 and the stress-curve, indicating that insufficient permanent plastic deformation occurred during test A for the [110]-compression coupon.

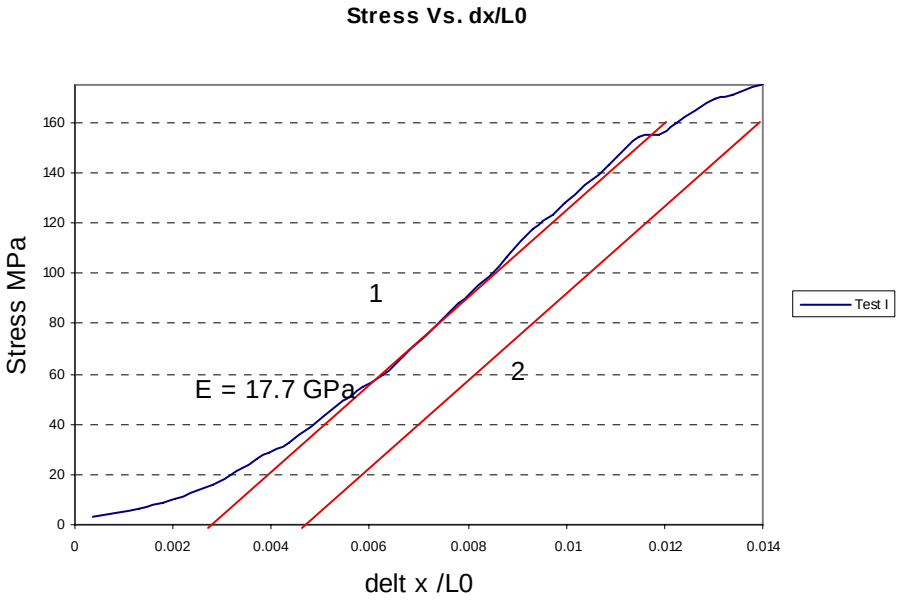

Figure 31 Stress vs. deltax/Lo in test A

The sample was reloaded (test B) with the same strain rate and the resulting stress vs. delta x/L_0 curve is shown in Figure 32.

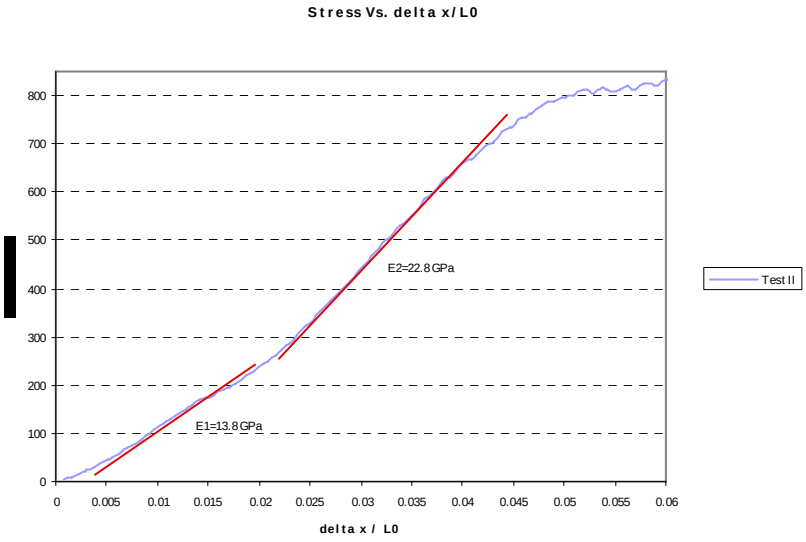

Figure 32 Stress vs. delta x/Lo for sample 1 Test B

Two approximately linearly sloped regions can be distinguished in Fig. 33; Region 1, with a slope of 13.8 GPa and region 2, with a steeper slope of 22.8 GPa. Region 1 of the curve essentially retraces test A with a first minor but detectable slope change at a stress of about 150 MPa. Hence, it seems reasonable to conclude that Region 1 in both test B (Figure 33) and test A (fig. 31) are presumably associated with small realignments of the entire assembly and thus are artifacts of the experimental set up. The positive slope change between Region 1 and 2 in Fig. 33 would be consistent with Region 2 indicating further elastic loading of the sample after the initial realignments. The negative slope changes in Figure 33, which associated with the beginning of yielding, can be discerned for stresses above 600 MPa. Thus, the curve of figure 33 implies a very high yield stress value.

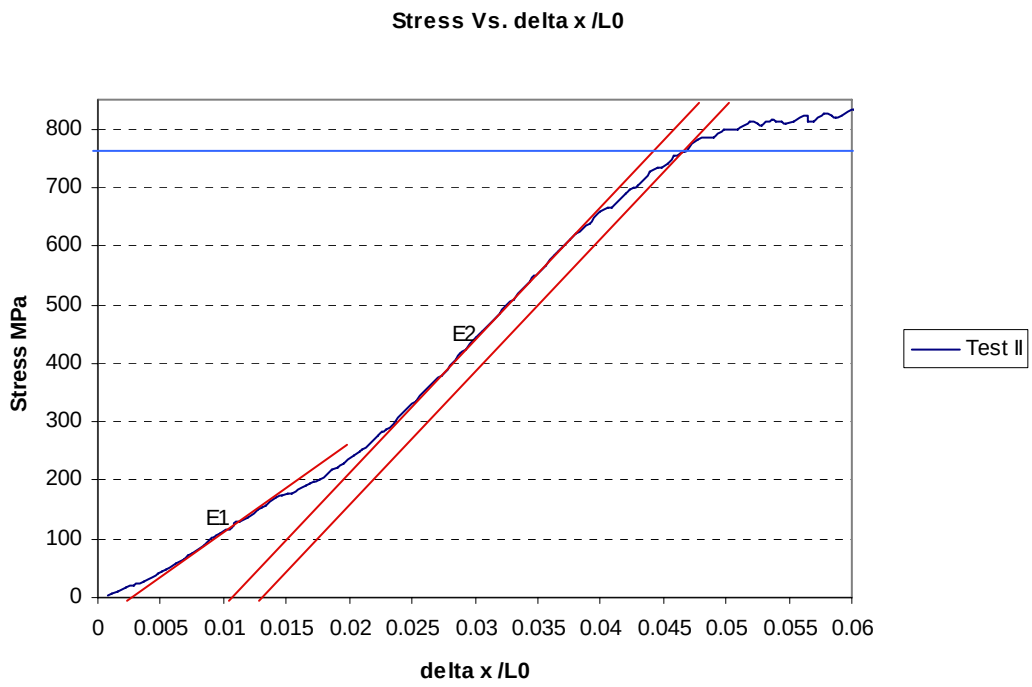

Figure 33 Stress vs. delta x/L0 for test B

Using Region 2 as the relevant elastic slope prior to yielding, the 0.2% proof stress or yield stress was found in Test B (Figure 34) to be 760 MPa.

From Figure 34, the following results were obtained:

i. E1= 13.5 GPa and E2= 22.8 GPa

ii. The 0.2% Yield Stress of E2= 760 MPa

iii. According to the experimentally measured Stress vs. Position graph, the change of the length of the sample is 0.0869 mm.

iv. According to the measurement by micrometer prior to and after the compression test of the coupon, the change in length of the sample was (0.095+/-0.005) mm,

Table 5 shows Schmid Factors for the 16 different slip systems possible in $L1_0$-FePd for the nominal loading axis of compression parallel to [110]. The table indicates that the only active dislocations will be superdislocations with Burgers vectors <101> and twin dislocation with Burgers vectors parallel to <112>. Ordinary dislocations will not be active in this compression test because their Schmid factors are zero. The most highly stressed systems involve the twining dislocations on (111) and (11-1) with Schmid factors of 0.47, close to the maximum magnitude of 0.5. The superdislocations of type <101> in the (111) and the (11-1) planes experience identical resolved shear stresses of also relatively large magnitude, with Schmid factors of 0.41. Which of these two different types of slip systems is active at the beginning of plastic deformation depends on the magnitude of the critical resolved shear stresses for the twinning dislocation systems and superdislocation systems.

Table 5 Schmid Factor's Table for [110] direction compression test

Plane	Direction	Magnitude of Schmid Factor
(111)	[-110]	0
	[10-1]	0.408
	[0-11]	0.408
	[11-2]	**0.47**
(11-1)	[-110]	0
	[011]	0.408
	[101]	0.408
	[112]	**0.47**
(-1-11)	[-101]	0
	[0-11]	0
	[110]	0
	[-1-1-2]	0
(1-11)	[011]	0
	[110]	0
	[10-1]	0
	[1-1-2]	0

Assuming that yield stress is 760 MPa and also assuming that the slip/deformation systems (mechanical twining, TD, and/or superdislocations, SD) with largest Schmid factors are the primary slip systems (PSS), then the apparent critical resolved shear stress can be estimated as follows:

$$\tau_{crss}=\text{Yield stress x Schmid factor} \quad (51)$$

Thus, if the TD or mechanical twinning is considered active as PSS, then

$\tau_{<112>\{111\}}$ =760 x 0.47 = 357.2 MPa.

If the superdislocations, SD, are considered as active PSS, then

$\tau_{<101>\{111\}}$ =760 x 0.41 = 311.6 MPa.

These are very large values for the critical resolved shear stresses required for activation of the SD and TD slip systems in $L1_0$-FePd when compared to values of critical resolved shear stresses of pure metals. Also, compared with the values of the yield stresses reported for the polytwinned polycrystalline $L1_0$-FePd (Rao and Soffa 1995), which for room temperature were on the order of 480MPa to 600MPa and implies at maximum critical resolved shear stresses on the order of

between 240MPa to 300MPa (i.e. for maximum Schmid factor of 0.5), the values of the critical resolved shear stresses that can be deduced from the experimental compression test data seem high.

6.3.1.1 SLIP TRACE ANALYSIS Figure 34 shows a schematic drawing of the compression coupon sample with the active slip planes expected for loading parallel to [110]. According to the Schmid factor calculations, the only active slip planes should be (111) and (11-1). The traces of the (111) plane make an angle of about 35 degrees with those of the (110) plane on the face of the compression coupon with nominal surface normal parallel to [-99-2]. The traces of the (111) and (11-1) intersect in the (-99-2), enclosing an angle of about 70 degrees, while they should be parallel to each other in the (-119) surface of the [110]-compression coupon.

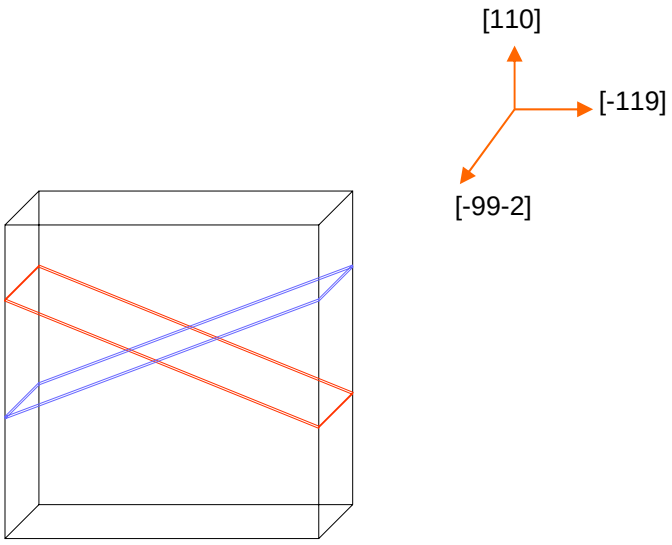

Figure 34 Schematic drawing of the sample with slip planes

Figures 35-37 show optical microscope and scanning electron microscope images of the slip lines in the single crystal [110]-compression coupon. Two of the {111} planes are active in this orientation. Six possible active systems with non zero Schmid factor exist.

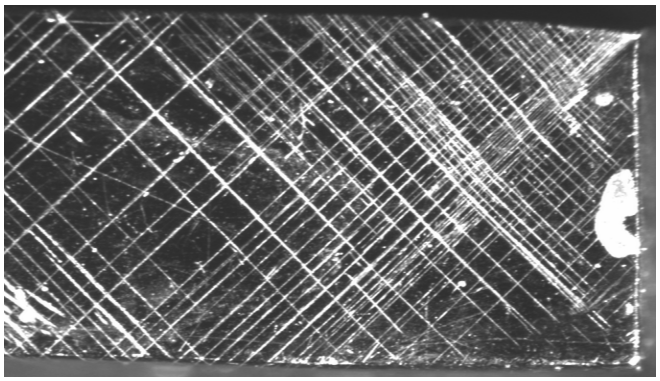

Figure 35 Optical micrograph showing traces of slip planes of (111) and (11-1) in the (-99-2) surface of the [110]-compression coupon.

Figure 34 shows the traces of two {111} planes in the (-99-2) face of the compression coupon. The angle that was measured between the traces is 70 degrees, which agrees with theoretical considerations (e.g. Table 5 and Fig. 35).

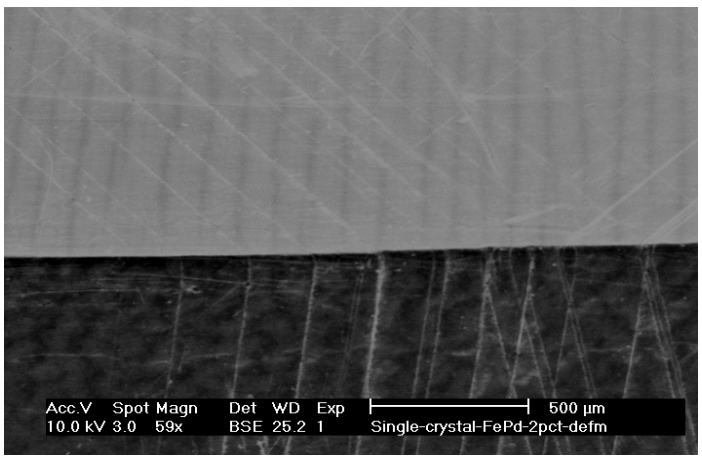

Figure 36 : SEM image of the slip lines on the surfaces of the [110]-compression coupon

Figure 36 shows an SEM micrograph of the slip lines of the two slip planes, including the intersection along the edge between the (-99-2) and (-119) surfaces for the compression coupon. The slip traces of the slip systems involving the respective (111) and (11-1) planes continue in the two side surfaces approximately parallel to (-99-2) and (-119).

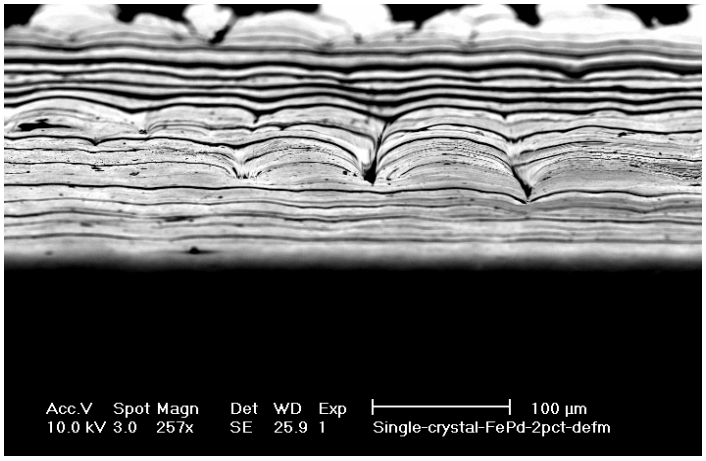

Figure 37 SEM image of the slip lines on the (-119) side surface of the [110]-compression coupon as viewed along approximately [110] from the top.

Figure 37 shows a top view of the slightly inclined slip steps on the (-119) side surface of the compression coupon as seen approximately parallel to the [110] direction from the top of the sample. The slip steps are progressive and appear approximately parallel to each other.

Thus, the slip trace analysis for sample I compressed nominally parallel to [110] confirms slip activity onto slip planes (111) and (11-1), which contain the most highly stressed TD and SD deformation or slip systems (Table 5). Slip on the symmetrically stressed slip planes (111) and

(11-1) was responsible for the plastic strain accommodation. The total linear strain,~ $L\text{-}L_0/L_0$, introduced during compression test I parallel to [110] axis was about 1.5%. Hence, plastic deformation should have been sufficient to have produced activity of all six highly stressed deformation systems. It might be noted that single slip or easy glide is not expected for this high-symmetry loading axis of [110], and multiple slip system activity and the onset of work-hardening is expected once macroscopic yielding is accomplished. Hence, interpretation of Region 2 of the compression test data, represented in figures 29 and 30 as plastic flow regime, appears to be consistent with both geometric considerations based on Schmid factor analysis and the slip trace pattern and macroscopic shape change observed for the [110]-compression coupon.

6.3.1.2 TEM RESULTS FOR SAMPLE I

Sample I was loaded in compression close to the [110] direction, and therefore is expected to have two highly stressed active slip planes, (111) and (11-1). The Schmid factor analysis indicates that the most highly stressed active slip systems on the respective (111) and (11-1) planes involve the respective twinning dislocations, b= [11-2] and [112], with Schmid factors of 0.47. The slip system with the next highest Schmid factor, 0.41, involve the superdislocations with b = <101> and b=<011>. Hence, glide activity of twinning dislocations (deformation or mechanical twinning) and superdislocations on the two slip planes is expected to occur at small plastic strains.

The analysis of preliminary TEM data for sample I support these predictions based on the Schmid factors. For instance, the two-beam bright field TEM micrograph (figure 38) displays twinning dislocation activity on two slip systems (mechanical or deformation twinning), labeled by traces X and Y in the figure. The active deformation twinning systems involve the (111) and

(11-1) planes. The active g vector, 111, in figure 38 is perpendicular to the trace of the nearly edge-on oriented (111) plane (trace X), while the trace labeled Y is consistent with the trace of the (11-1) plane in the image plane. The arrays of contrast lobes associated with the edge-on (111)-planes are consistent with nearly end-on dislocation arrays contained in the active slip plane (L in fig. 39). A few individual dislocations, often with curved line morphology, which are not associated with the deformation twinning systems, can also be discerned (e.g. D in fig. 38).

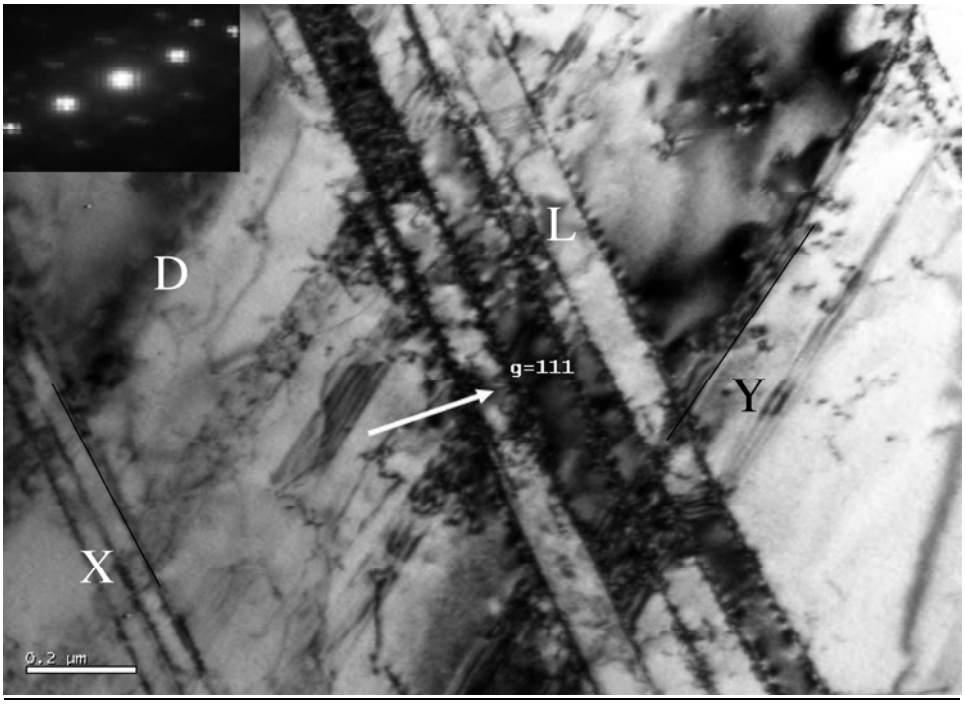

Figure 38 TEM Bright Field micrograph for active g=111 near [10-1] zone axis (ZA)

While the Burgers vector of these dislocations was not determined in these preliminary experiments, given their visibility with g=111, we can preclude them from having a Burgers vector, b, for which g.b=0. Also, their line morphology suggests that they may be contained primarily in the (11-1) plane. Considering only unit dislocations, this would limit the possible Burgers vectors to being either [101], [011] or ½[112], namely possibly active glide dislocations in slip plane (11-1), which is inclined to the viewing direction in figure 39.

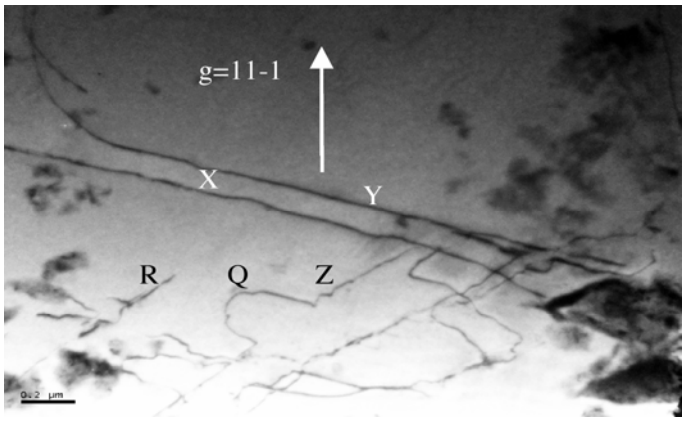

Figure 39 TEM Micrograph off the zone axis [101] with active g= 11-1

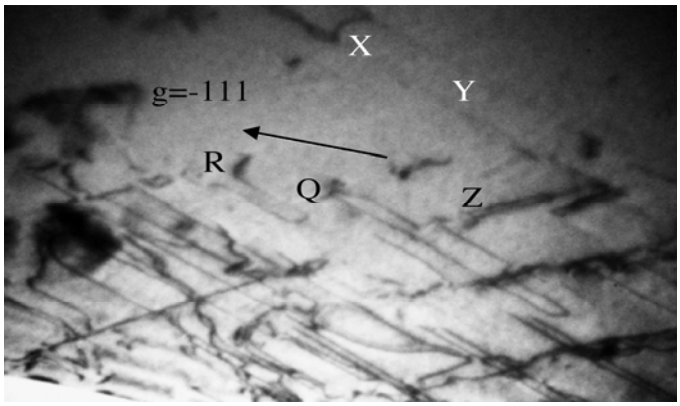

Figure 40 TEM Micrograph off the zone axis [101] with active g= -111

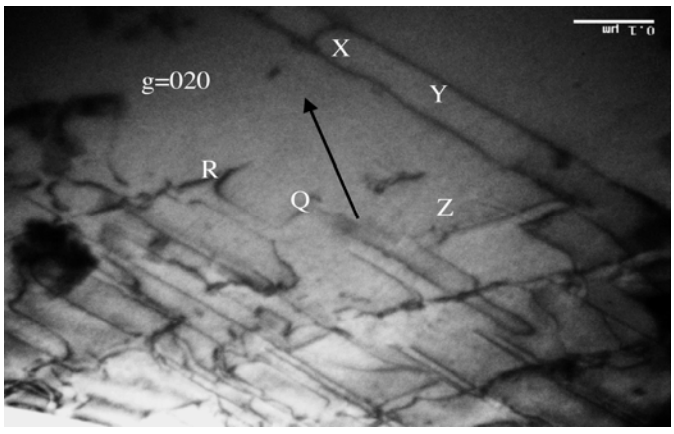

Figure 41 TEM Micrograph off the zone axis [101] with active g=020

Figures 39-41 show TEM Micrographs for the same area with different active g vectors. The dislocations X,Y,Z,Q, and R are labeled to exam their visibility with the different active g vectors in figures 39-41. The g.b rule states the following: “If the Burgers vector of the dislocation is perpendicular to the active diffraction vector, i.e g.b=0, there is no diffraction contrast from the dislocation the dislocation is invisible.”. Table 6 shows the visibility according to the g.b-rule for the possible unit dislocations in (111) and (11-1) and the different active g vectors used in figures35-37. V stands for visible while IV stands for invisible.

Table 6 g.b -rule visibility or invisibility for unit dislocations in (111) and (11-1) for the three active g vectors used in figures. 35-37. V is visible, IV is invisible. Assuming that the beamdirections were close to the respective ZA [101] and ZA [111].

b ↓ | g →	11-1	-111	020
10-1	V	V	IV
01-1	V	IV	V
11-2	V	V	V
101	IV	IV	IV
011	IV	V	V
112	IV	V	V

The dislocations labeled X and Q are invisible when the active g vector is 11-1, indicating that g.b is zero ((x1,x2,x3).(1,1,-1) = 0) ((q1,q2,q3).(1,1,-1)=0). The same dislocations are visible with active g = -111 and g =020. Consulting table 6 for a suitable Burgers vector of dislocation that is visible for both g = -111 and 020 and invisible g = 11-1, we find that dislocation X and Q have Burgers vectors parallel to [112]. Thus, they would be consistent with glide dislocations of the twinning type with b=1/2[112] for the (11-1).

Dislocations labeled Y, Z and R exhibit different contrast behavior than the dislocations X and Q, which means they have different Burgers vectors. The dislocations, Y,Z and R are visible with active g vector 11-1, invisible with active g vector (-111), and they are visible with active g vector (020). Again consulting table 6 for suitable Burgers vector matches, one can conclude that dislocations Y,Z and R have Burgers vectors parallel to [0-11], i.e. they are superdislocations with b=±[0-11], presumably gliding in the (111) plane. Table 7 summarizes the contrast behavior of the dislocations for the different g-vectors used in figures35-37.

Table 7 The visibility of different type of dislocations with different active g.

Dis	[11-1]	[-111]	[020]	Dislocation type
X	IV	V	V	[112]
Y	V	IV	V	[01-1]
Z	V	IV	V	[01-1]
Q	IV	V	V	[112]
R	V	IV	V	[01-1]

Thus, it is concluded that the only active glide dislocations observed in sample I with loading direction close to [110] are those with Burgers vectors parallel to [112] and [01-1]. This is consistent with the Schmid factor analysis, where 1/2[112] type twinning dislocations have the highest Schmid factor of 0.47, and [01-1] superdislocations have the next highest Schmid factor of 0.41. Hence, the results of the preliminary TEM analysis of the glide dislocations activated in FePd for loading parallel to [110] is consistent with the theoretical expectation based on the highest resolved stresses on the octahedral plane slip systems and also with the slip trace analysis performed here for the [110]-orientation loaded sample.

6.2.3 Sample II

A second compression test was performed at room temperature for a sample with a compression direction parallel to [-119]. The sample had a dimension of (6.62x3.18x2.62) mm^3. This sample was annealed at 590˚C for about 30 hours after the initial stress-assisted transformation. It was expected that this additional stress-free order-annealing treatment would be suitable to improve the quality of the single crystal further by coarsening the dominant orientation variant in favor of the other two variants that may have been present in the material in minor fractions. Unfortunately, our expectations were not met and, instead, the additional order-annealing degraded the quality of the single-crystal coupon considerably. X-ray diffraction scans prior to and after the additional heat treatment provided evidence for the presence of more than one variant of the three possible $L1_0$-orientaion variants in this sample, which was no longer a single crystal. Hence, only for one of the three possible orientation variants was the loading axis in this compression test parallel to [-119].

6.2.3.1 Stress Vs. Position Curve

The stress vs. strain curve for this test is shown in figure 43. The strain rate was nominally 0.0017/sec and the total magnitude of deformation was 1.6% of the initial length, L0=6.62mm.

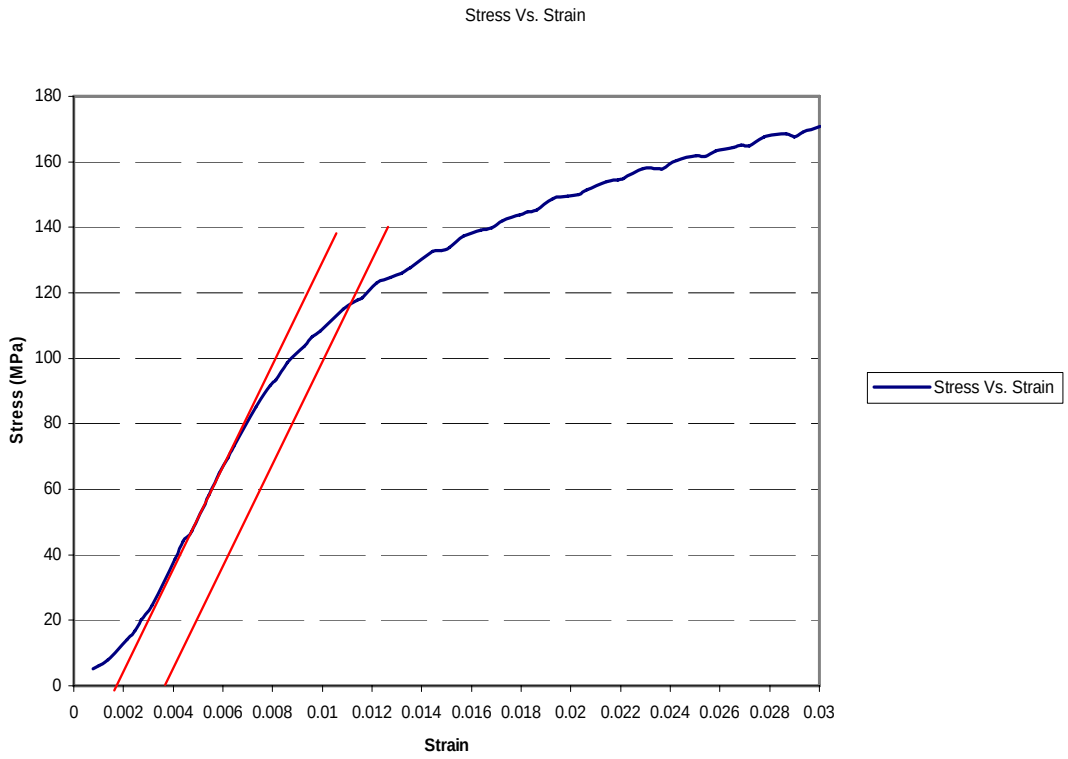

Figure 42 Stress vs. Strain curve for Sample II

Following identical procedures as described previously for the other compression tests, from the curve above, we find the following:

- Young's Modulus =14.52 GPa
- 0.2% Yield stress =119MPa

The value of the yield stress is significantly lower than for test I and work-hardening, typically associated with multiple slip system activity, is observed from the onset of plastic deformation.

This type of behavior would be expected for a polycrystalline sample and for loading of a single crystal sample for a highly symmetric loading axis.

6.2.3.2 SLIP TRACE ANALYSIS Figures 44 and 45 are optical micrographs of sample II after the compression test.Figure 43 is a sketch of the sample with the expected {111} plane traces. The slip trace pattern observed on the (110) surface of the compression coupon of sample II is very complex and involves many discontinuous traces that are not consistent with prediction based on the Schmid factor analysis of a single crystal compressed parallel to [-119]. The trace of the (-99-2) surface runs horizontal in figures 44 and 45, while that of the surface normal to the nominal compression axis runs vertical.

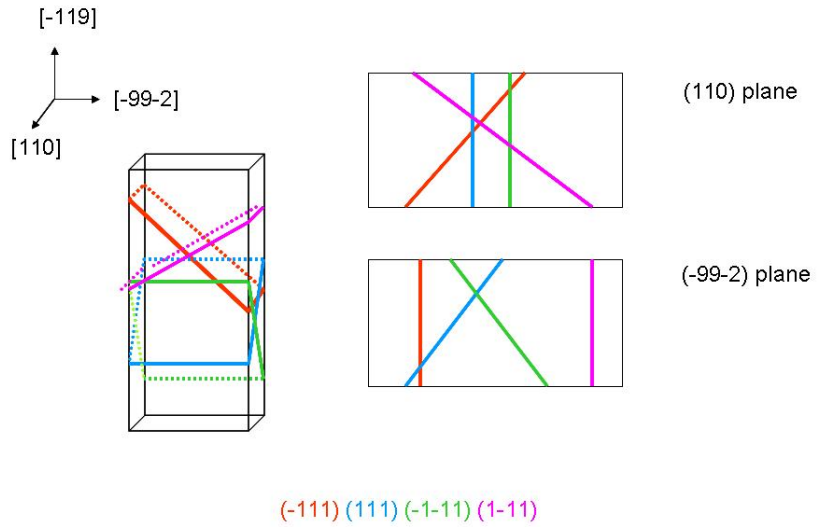

Figure 43 Sketch of sample II with the active {111} planes traces.

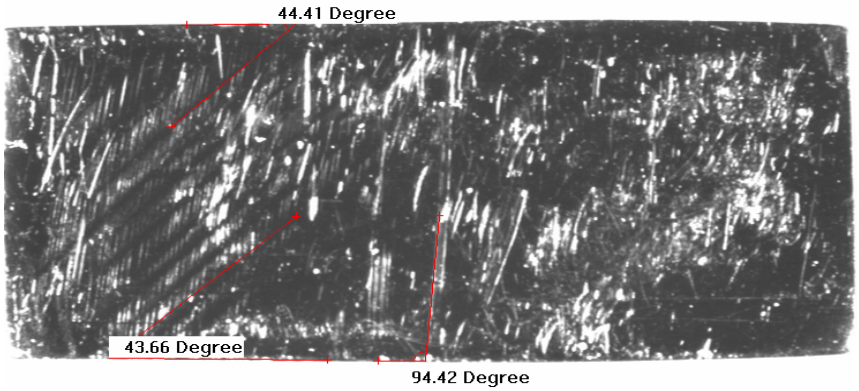

Figure 44 Complex pattern of slip traces on the (110) plane surface of sample II.

Slip traces of (-111) make an angle of about 44˚ with the (-99-2) plane trace. Slip traces of (111) and (-1-11) make an angle of about 94˚ with the (-99-2) plane traces. Slip traces of (1-11) make an angle of 153˚ with the (-99-2) trace in the (110) surface. Some slip traces discernible on the relevant surface of the sample II coupons after compression (figure 45) are apparently approximately parallel to these expected traces. However, if sample II were a single crystal, they would be expected to be continuous, as in the sketch, which evidently is not the case. Numerous other traces observed experimentally (see figure 45 are not consistent with the crystallographic prediction (e.g. sketch in figure 43), indicating that sample II was not a single crystal but probably consisted of more than one variant of the three orientation variants of the $L1_0$-Phase that form upon ordering in the solid state from the FCC phase.

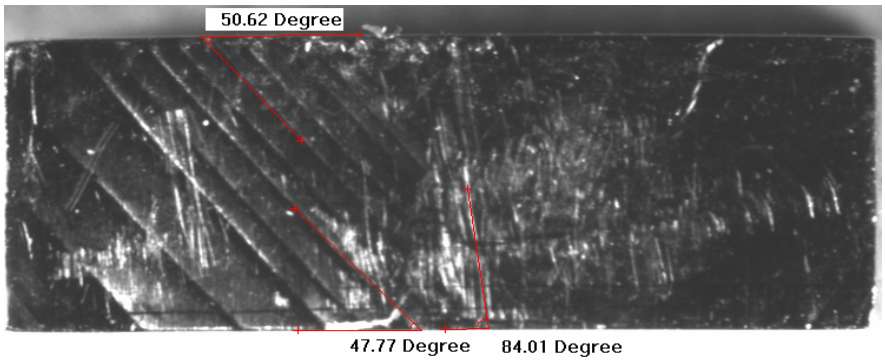

Figure 45 : (99-2) of the sample

Figure 45 shows slip traces on the (-99-2) plane. The trace of the (110) surface plane runs horizontally across the micrograph. The expected trace line pattern expected for the (-99-2) surface for the relevant four different {111) planes is shown in the sketch in Figure 40. The slip traces of (-111) and (1-11) planes enclose an angle of about 90 degrees with the (110) plane traces. Again, significant discrepancies and many discontinuities of the slip line traces are observed for the (-99-2) surface of the compression sample II. Hence, unlike for the sample I [110]-compression coupon, the slip lines are not particularly well visible for the sample compressed nominally along the [-119] direction. This would be consistent with reversion to a multiple orientation variant polycrystalline sample during the additional 30h stress-free heat treatment. Thus, this sample is expected not to be a single variant $L1_0$-FePd crystal.

The yield stress values for test 1 and 2 were different. The difference cannot be attributed to differences in Schmid factors alone since the magnitudes were not significantly different enough to account for the about six-fold lower yield stress in sample II relative to sample I. Since both XRD (not shown here for brevity) and the slip trace analysis for sample II indicate that the [-119] coupon did not constitute a single crystal, conclusions regarding the critical resolved shear stresses, τ_{CRSS} or CRSS, of the SD and TD system cannot be drawn from this test data.

However, the coupon was deformed in compression to a controlled value of about 1.6% of total linear strain at a reasonable rate at room temperature. Hence, while little can be concluded regarding the critical resolved shear stresses of the various types of slip systems available to L10-FePd from this test, it clearly exhibits slip line patterns and presumably consists of large domains of the possible orientation variants. Hence, it should contain deformation induced dislocation structures suitable for TEM investigations. These TEM studies can elucidate details of the dislocation fine structure of the dislocations activated during room temperature loading and will enable determination to the actual microstructure of sample II, which is required to develop a clearer understanding of the complex slip line patterns observed by optical and SEM imaging.

6.4 DISLOCATIONS TEM IMAGE SIMULATION

6.4.1 The Image Simulation of Ordinary Dislocations

OD's may dissociate into Shockley partials bounding a CSF ribbon:

$$\frac{1}{2}[\bar{1}10] \rightarrow \frac{1}{6}[\bar{2}11] + CSF + \frac{1}{6}[\bar{1}2\bar{1}] \tag{52}$$

The simulated images for this case are illustrated in Figures 47-52. The images were simulated for systematic raw g = 020, Foil Normal FN [10,0, 11], Beam Direction BD [101] with the above Shockley partials and the dislocations direction DD was -110 (screw type).

Figure 47 illustrates the dissociated OD with a width of 0nm of CSF (no CSF) (compact OD) while Figure 48 shows the dissociated OD with a width of 0.5 nm of CSF (very narrow). Figure 49 illustrates the same thing but with a width of 1 nm of CSF. Figure 50 illustrates the same thing with a width of 2nm CSF, and finally Figure 51 shows the dissociated OD with a width of 10 nm of CSF.

A contrast change can be observed from the top and the bottom of the dislocations lines, where in the top the contrast changes from dark to bright while in the bottom the contrast changes from bright to dark in both FePd and FePt. The CSF fringes develop in FePd from a small width, about 2nm, while in the case of FePt, CSF fringes develop from a width of 3nm. In FePt, the simulated image of the dissociated OD with a width of CSF that is less than 3nm will look like a single thick dislocation, as shown in Figure 47b, 48b, 49b and 50 b.,

Figure 52 illustrates the dissociated Ordinary Dislocation with CSF width of 10 nm. In this figure, it is clear that the CSF fringes are fully developed and the fringes contrast changes in the same manner in both FePd and FePt.

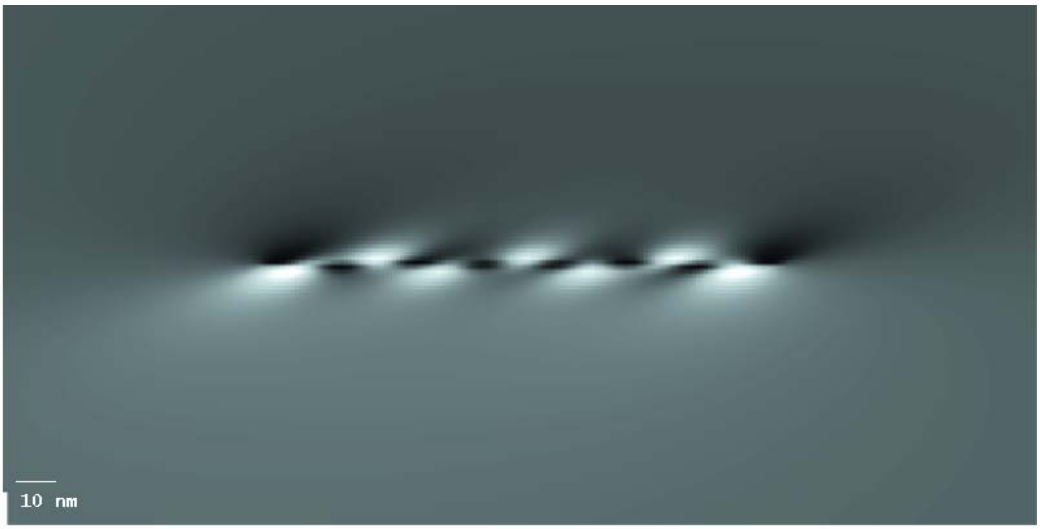

a.FePd , Dissociated OD with CSF = 0 nm

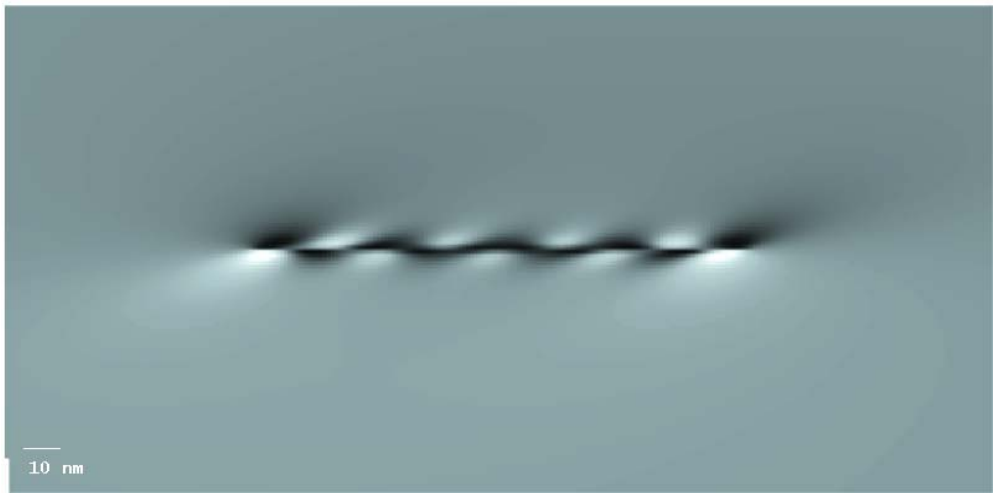

b. FePt, Dissociated OD with CSF = 0 nm

Figure 46 Dissociated OD with CSF 0 nm a. FePd , b. FePt

Figure 46 shows the Ordinary dislocation in both FePd and FePt . The g.b =1 in this case since it is a compact Ordinary Dislocation. It is clear that Ordinary dislocation contrast is the same in FePd and FePt.

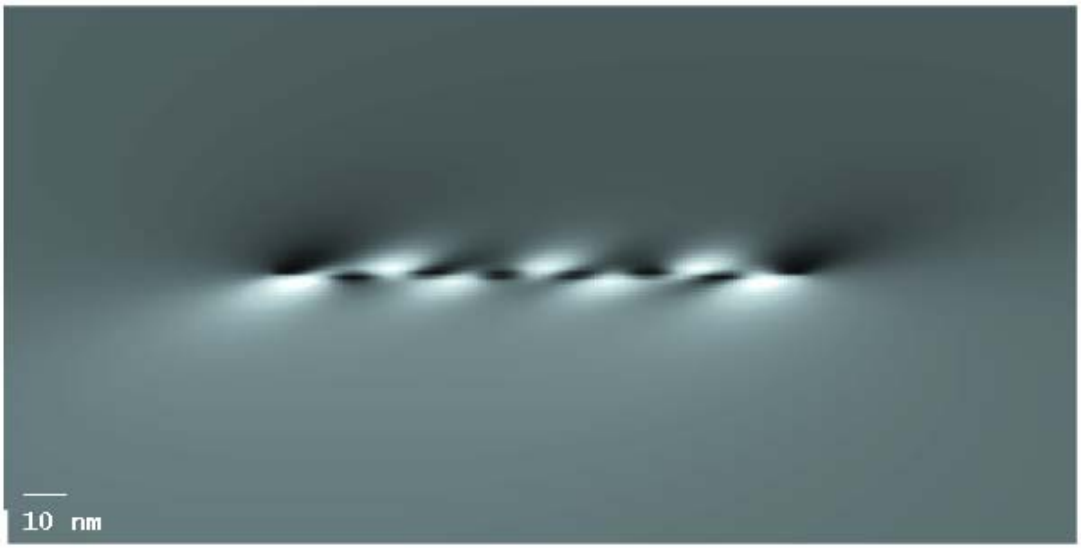

a. FePd ,Dissociated OD with CSF 0.5nm

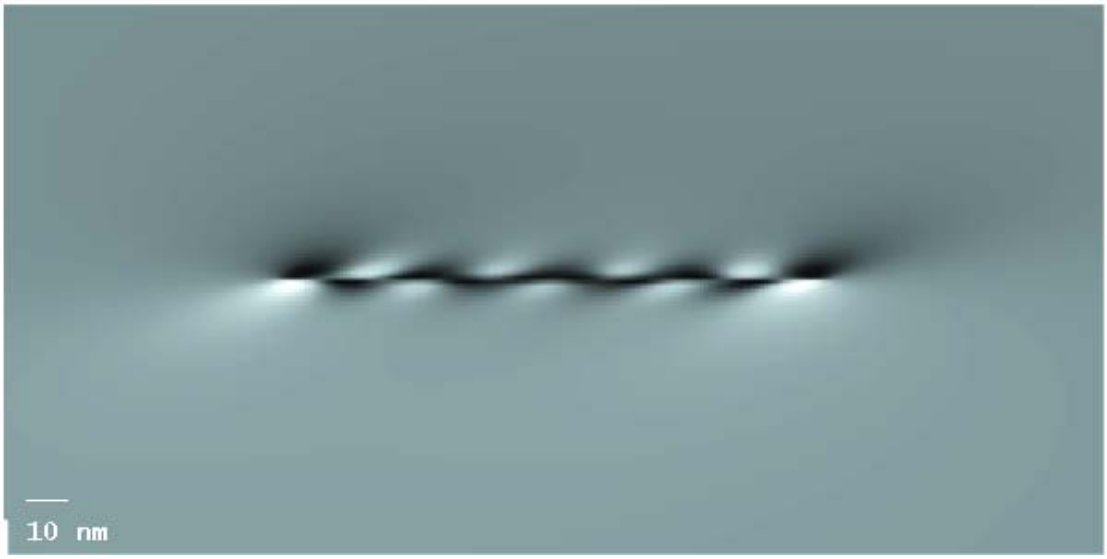

b.FePt, Dissociated Od with CSF 0.5 nm

Figure 47 Dissociated OD with CSF 0.5 nm a. FePd , b. FePt

Figure 47 shows dissociated Ordinary Dislocatoin with Complex Stacking faults that have a width of 0.5 nm. From the Figure above it is clear that 0.5 nm is a small faults width to be resolved.

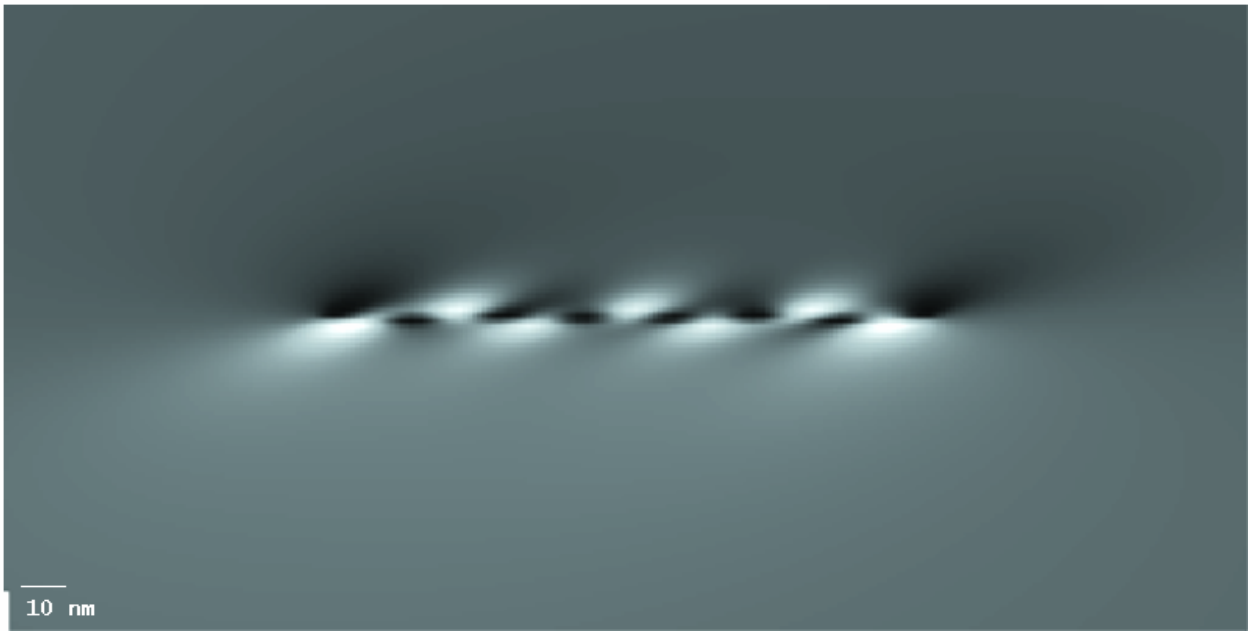

a.FePd Dissociated OD with CSF 1 nm

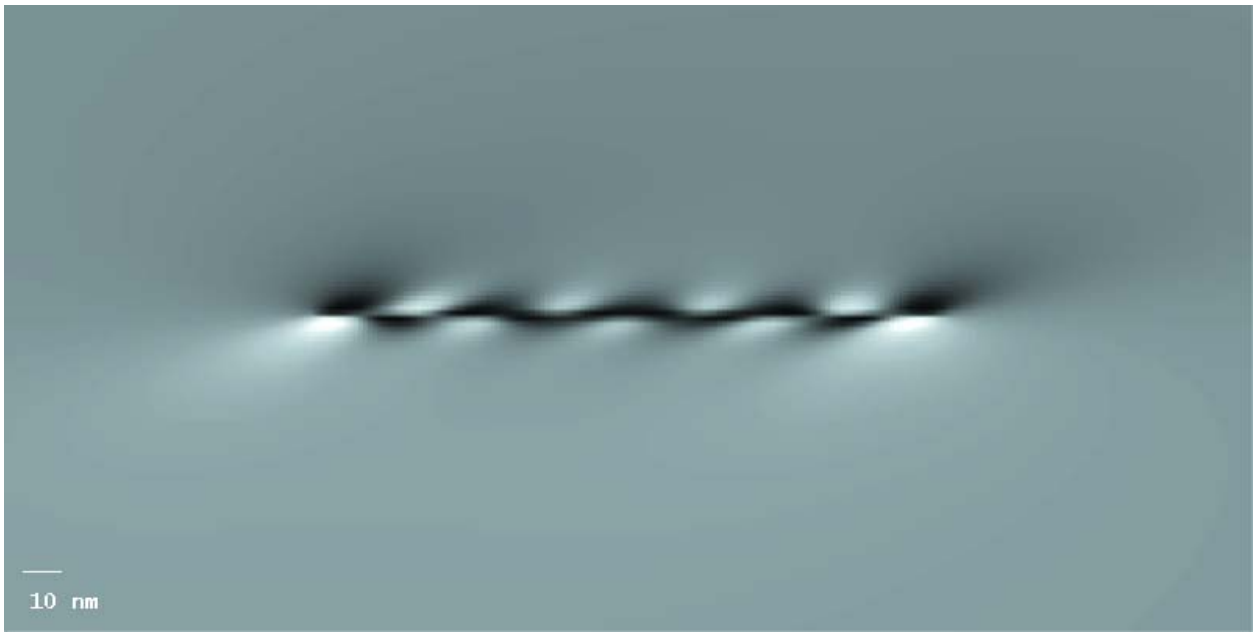

b. FePd Dissociated OD with CSF 1 nm

Figure 48 Dissociated OD with CSF 1 nm a. FePd , b. FePt

Figure 48 shows dissociated OD with CSF width 1nm. This width is still so small to resolved.

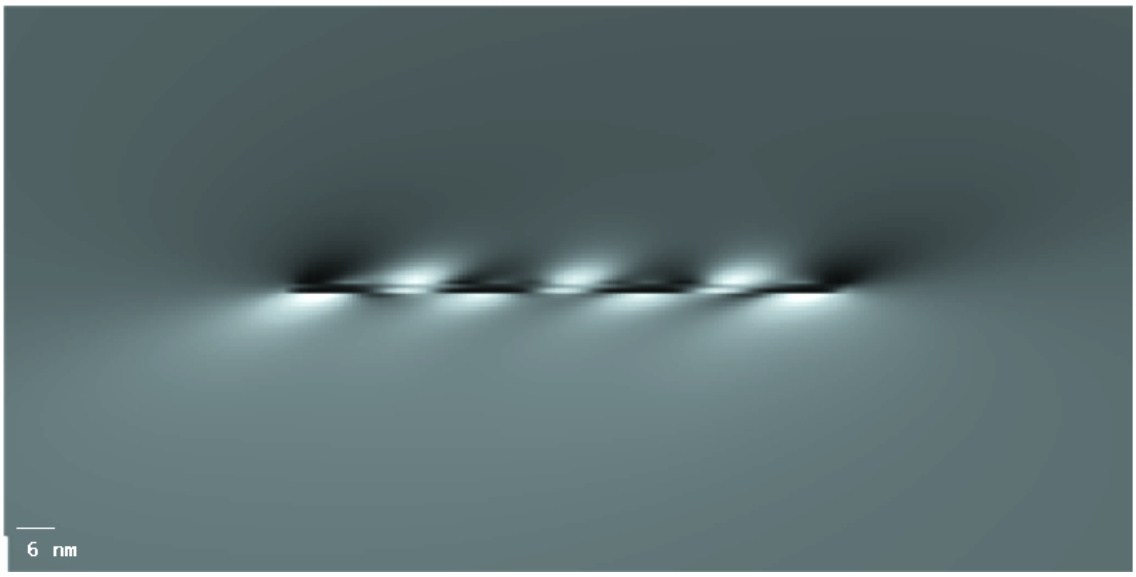

a. FePd, Dissociated OD with CSF = 2 nm

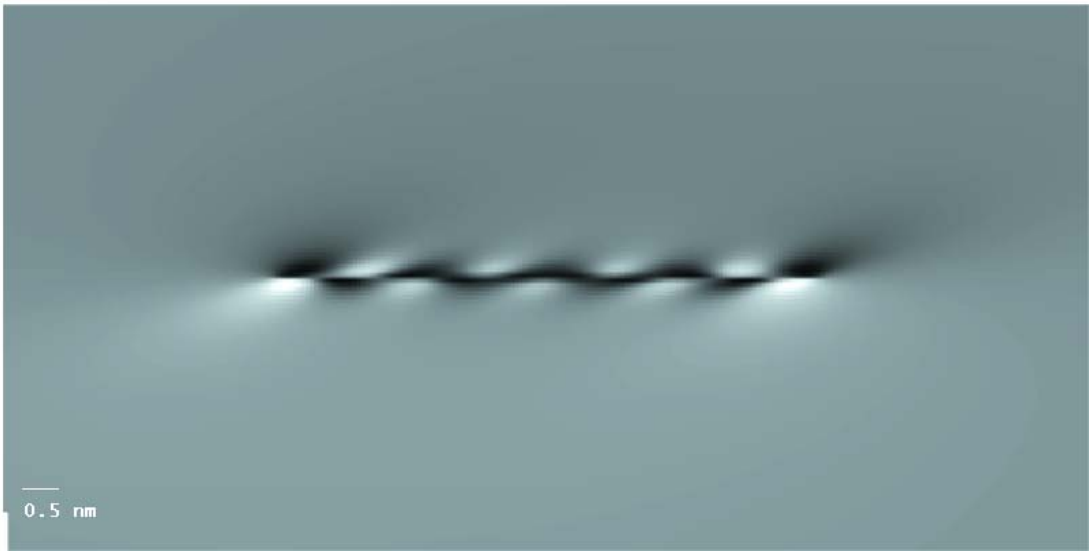

b. FePt, Dissociated OD with CSF = 2 nm

Figure 49 Dissociated OD with CSF 2 nm a. FePd , b. FePt

Figure 49 shows dissociated OD with CSF width 2 nm. In FePd, the CSF fringes are resolved and visible. In FePt, the CSF fringes are not resolved.

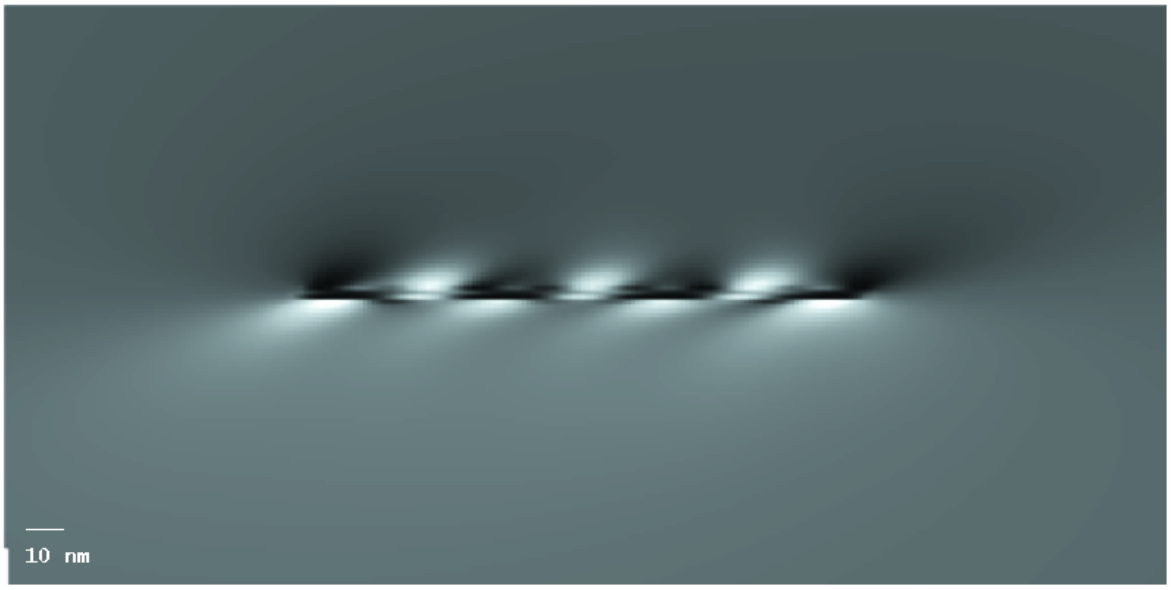

a. FePd, Dissociated OD with CSF = 3 nm.

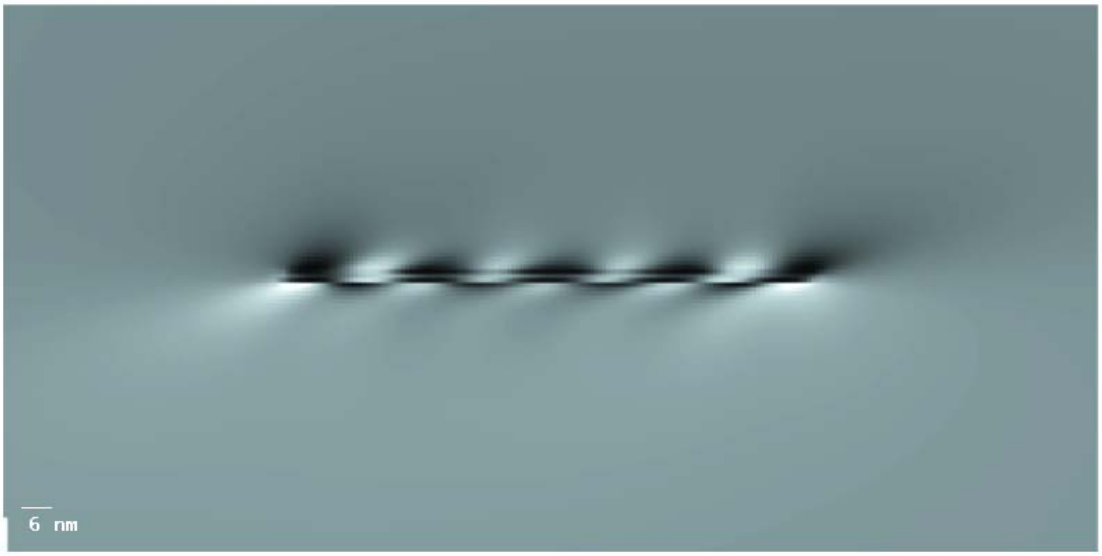

b. FePt Dissociated OD with CSF = 3 nm

Figure 50 Dissociated OD with CSF 3 nm a. FePd , b. FePt

Figure 50 shows the Dissociated OD with CSF width 3 nm. CSF fringes are resolved in both FePd and FePt. Both simulated images look similar to each other.

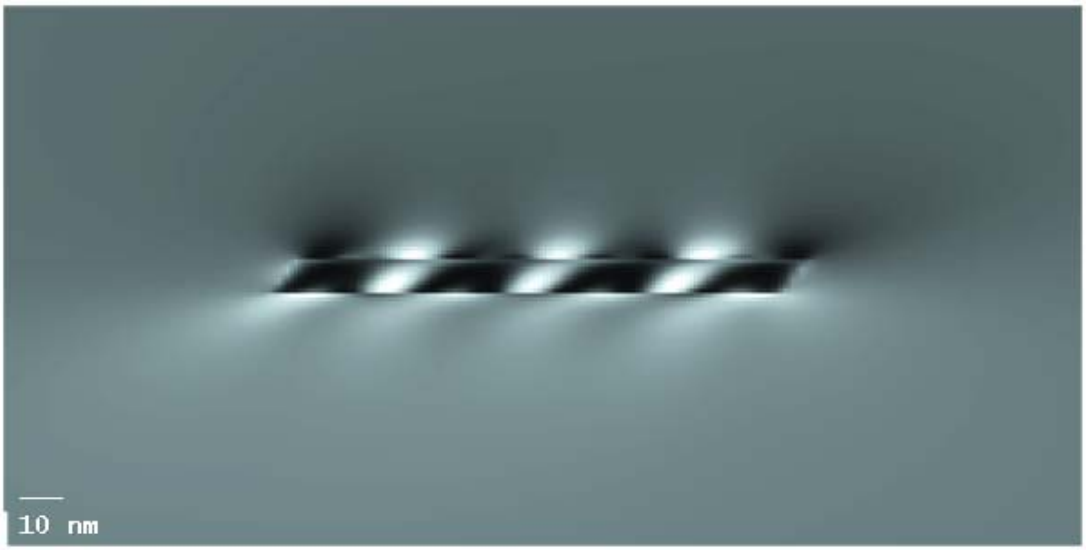

a. FePd, Dissociated OD with CSF = 10 nm

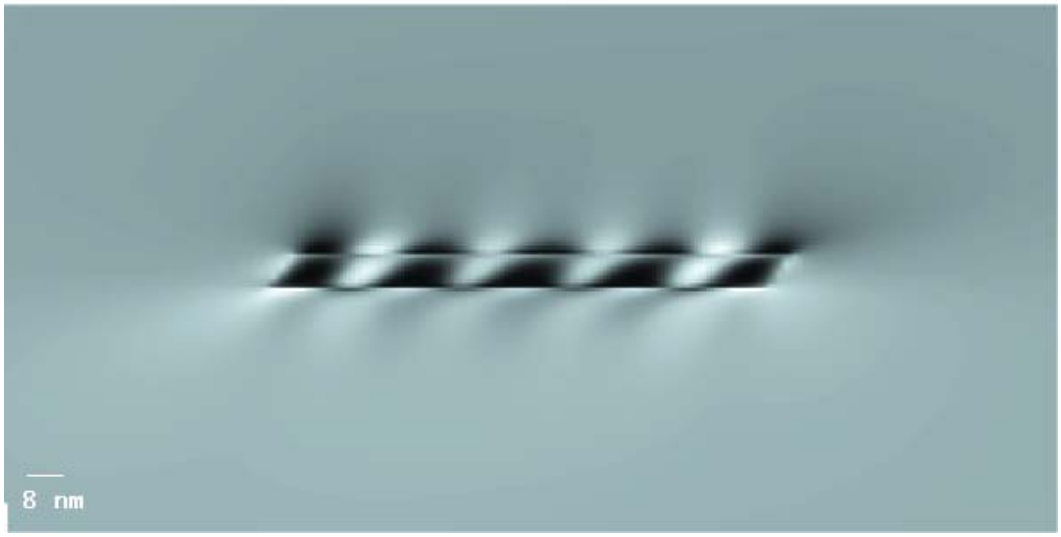

b. FePt, Dissociated OD with CSF 10 nm

Figure 51 Dissociated OD with CSF 10 nm a. FePd , b. FePt

Figure 51 shows the dissociated ordinary dislocation with CSF width 10 nm. In this case CSF fringes are visible and resolved. The TEM Ordinary Dislocation image simulation looks similar in both FePd and FePt.

6.4.2 Twin Dislocations Image Simulation

The three-fold dissociation of ½ [11-2] twin dislocations involves two stacking faults:

$$\frac{1}{2}\left[1\,1\bar{2}\right] \rightarrow \frac{1}{6}\left[1\,1\bar{2}\right] + SESF + \frac{1}{6}\left[1\,1\bar{2}\right] + SISF + \frac{1}{6}\left[1\,1\bar{2}\right] \tag{53}$$

The image simulation of this dissociated dislocation of the two Shockley's partials have direction DD [-110], edge direction, foil normal FN (10,0,11), the beam direction BD [101] and the systematic row is g 020 .

Figure 53 shows the image simulation of a dissociated twin dislocation in FePd and FePt. The contrast changes in the same manner in both FePd and FePt. The SESF fringes and SISF fringes are more visible in FePd than in FePt.

a. Dissociated TD in FePd.

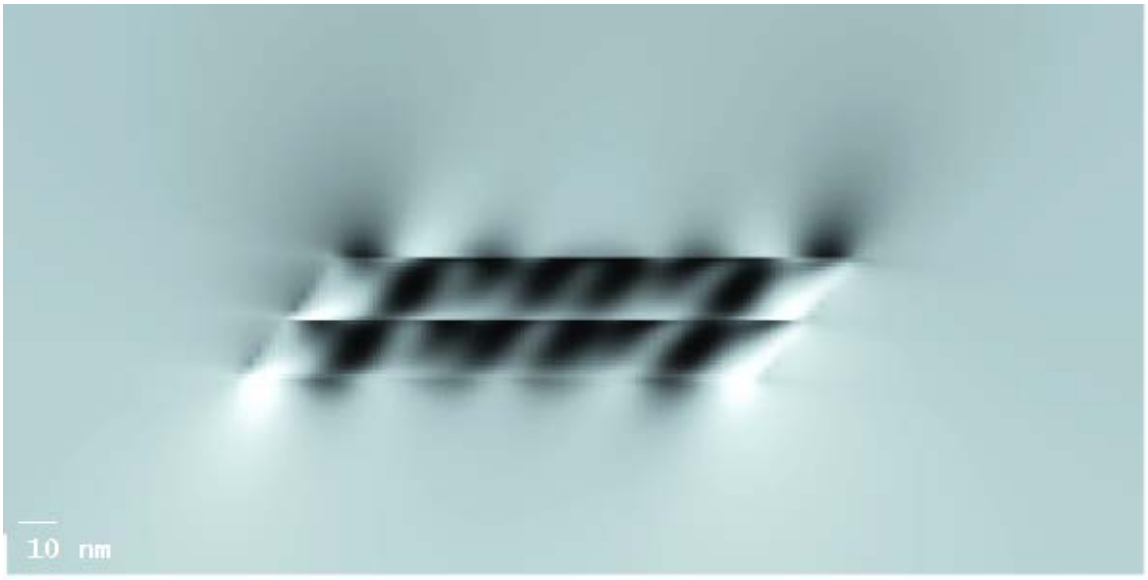

b. Dissociated TD in FePt.

Figure 52 Dissociated Twin Dilocation in a. FePd , b. FePt

Figure 52 shows the dissociated twin dislocation in FePd and FePt. There is a clear similarities in the contrast in both FePd and FePt image, but in FePd the contrast is more complex than in FePt.

6.4.3 Image Simulation for Super Dislocations:

6.4.3.1 TWO FOLD DISSOCIATION OF SUPER DISLOCATION In an $L1_0$ system, the superdislocation can dissociate in two folds with an Anti Phase Boundary stacking fault as the following equation:

$$[01\bar{1}] \rightarrow 1/2[01\bar{1}] + APB + 1/2[01\bar{1}] \tag{54}$$

In order to simulate the TEM images for this dissociation, experimental conditions should be set. Conditions have been chosen as follows:

- FN of [10, 0, 11]
- BD [1, 0, 1]
- B1 = ½[01-1], B2 ½[01-1]
- Dislocation direction [0-11] (screw direction)
- Planar fault normal is (1, 1, 1) since the planar fault is in (1, 1, 1).
- RAPB ½(10-1)
- Systematic Row g (020)
- Foil Thickness 3ξ.
- Width of the APB 25,50,100

In this situation, the g.b = -1, so the dissociated superdislcation will be visible, and g.R =0, which means the APB will be invisible in this case.

Figures 54-56 show the simulated images for active g 020 for the two fold dissociated super dislocations in both FePd and FePt.

Other systematic rows were used to simulate this dissociated dislocation. Figure 56 illustrates the same dislocation but with g 20-2 . The APB width is 25 nm. Figure 57 illustrates also the same dislocations but with g 11-1 and APB width of 25 nm.

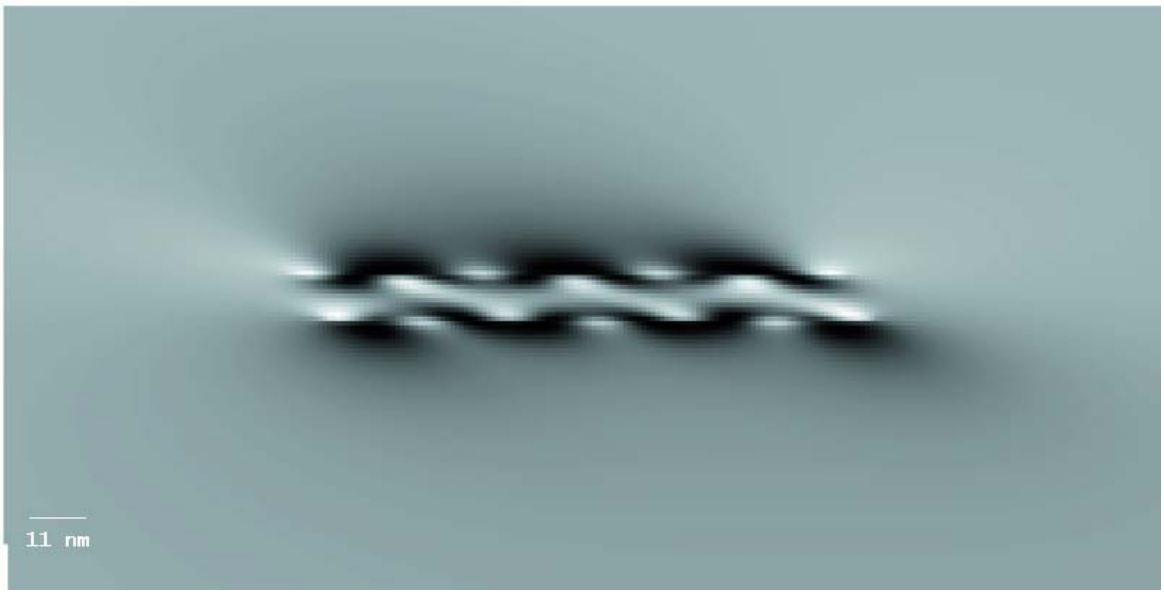

a. FePd APB=10 nm g 020

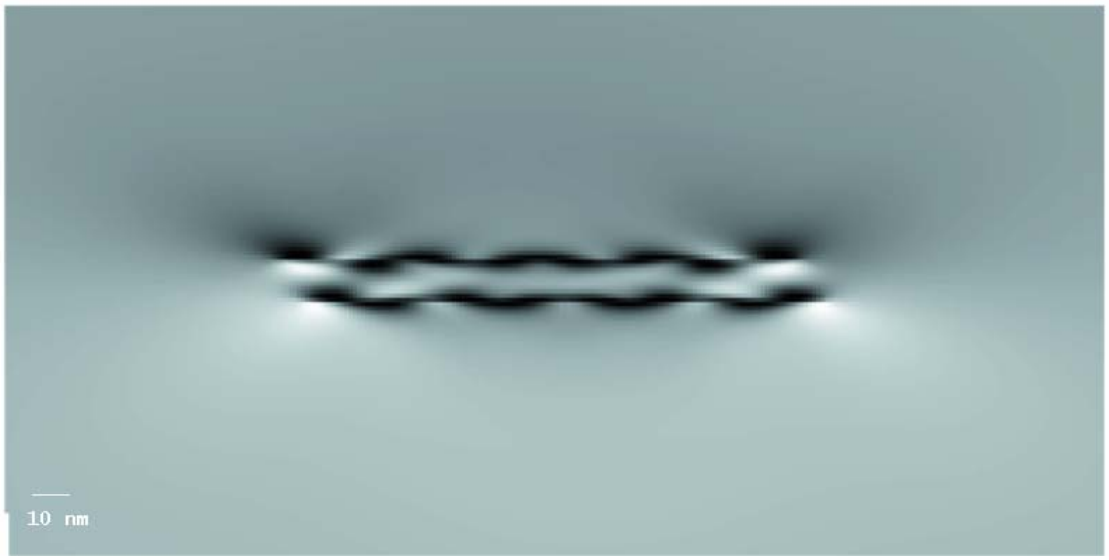

b. FePt APB = 10 nm g 020

Figure 53 two fold dissociated SD with APB width = 10 nm , g 020

Figure 53 shows the contrast intensity is different in FePd than in FePt. In FePd contrast changes from bright to dark for the upper superpartial while for FePt the contrast changes from dark to bright.

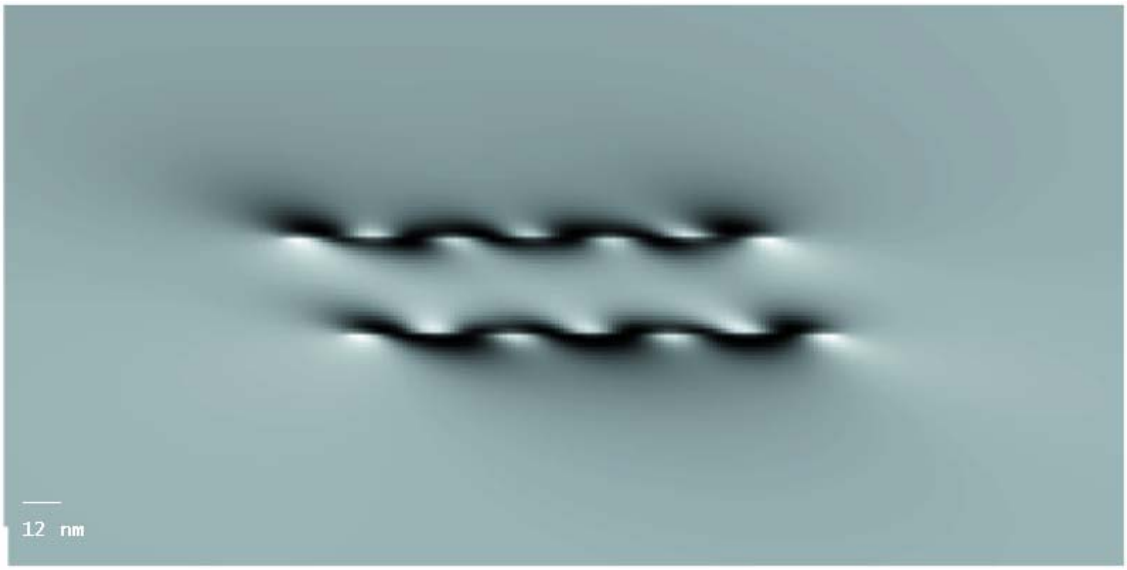

a.FePd APB 25 nm

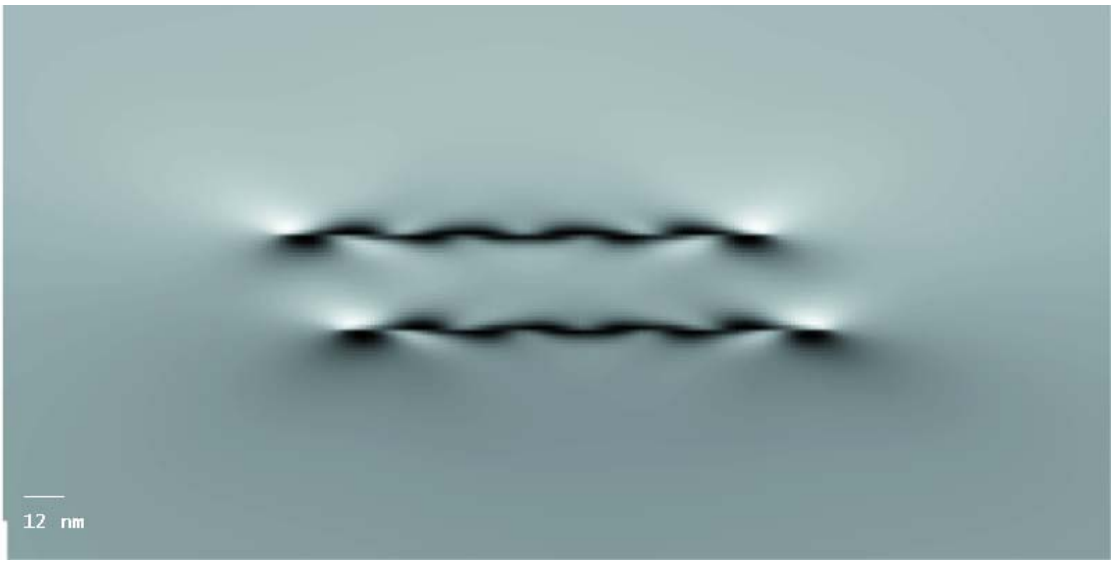

b. FePt APB 25 nm

Figure 54 Two fold dissociated SD with APB width = 25 nm, g 020

In Figure 54, the APB width is 25 nm, the super partials contrast is the opposite for FePd and FePt. In FePd, the contrast changes from dark to bright, while in FePt the contrast changes from bright to dark.

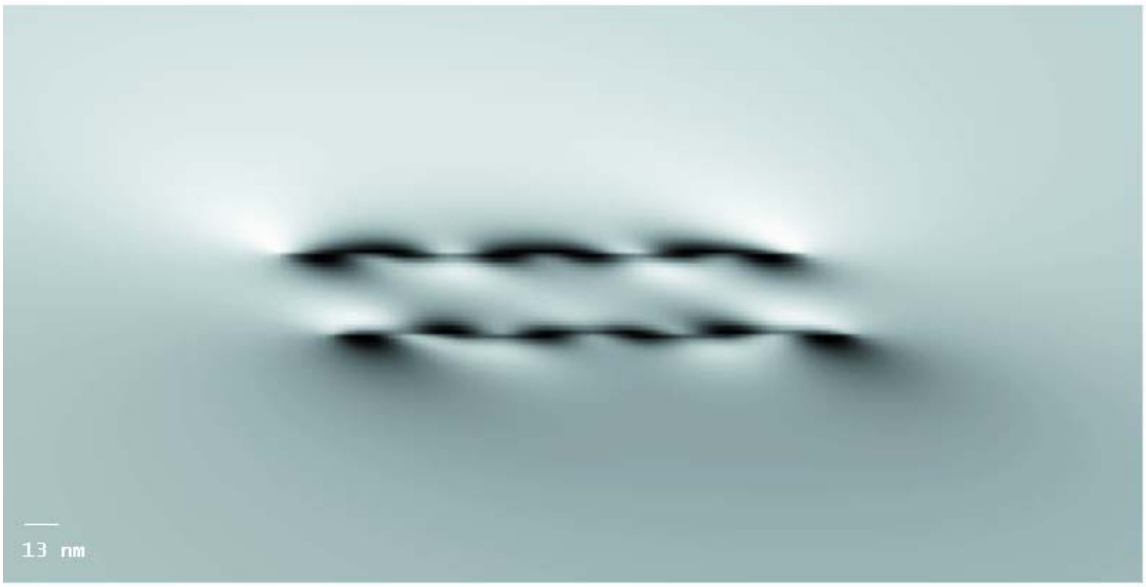

a.FePd APB 25 g 20-2

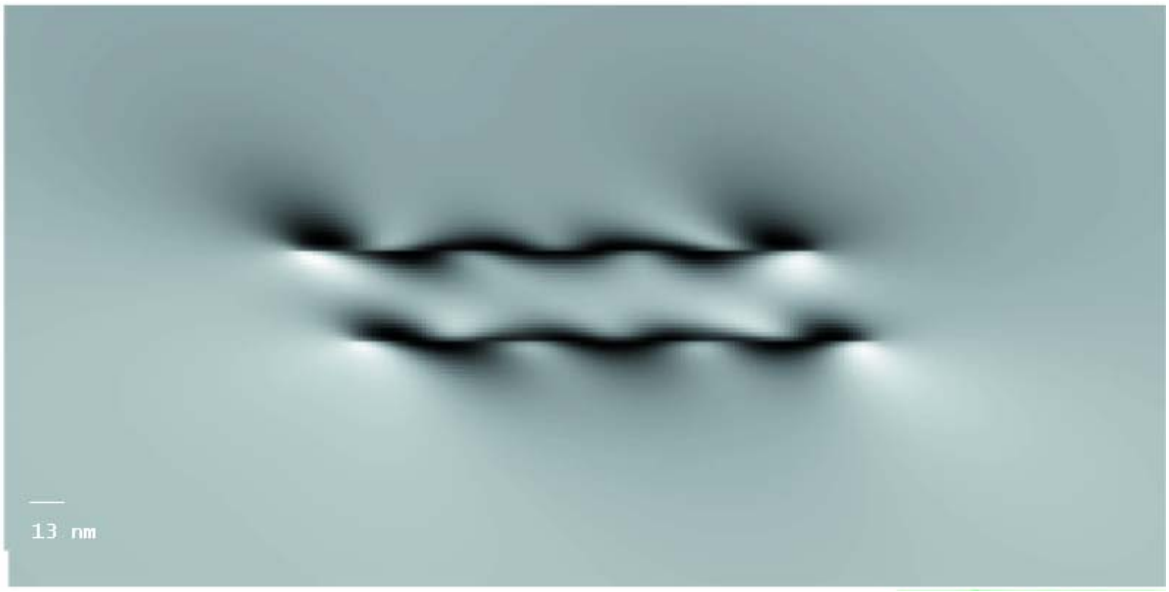

b. FePt APB 25 g 20-2

Figure 55 Two fold dissociated SD with APB width = 25 nm, g 20-2

In figure 55, the active systematic raw is 20-2. Iin this situation the contrast changes in the same sense in both FePd and FePt, but the intensity is more pronounced in the FePt image.

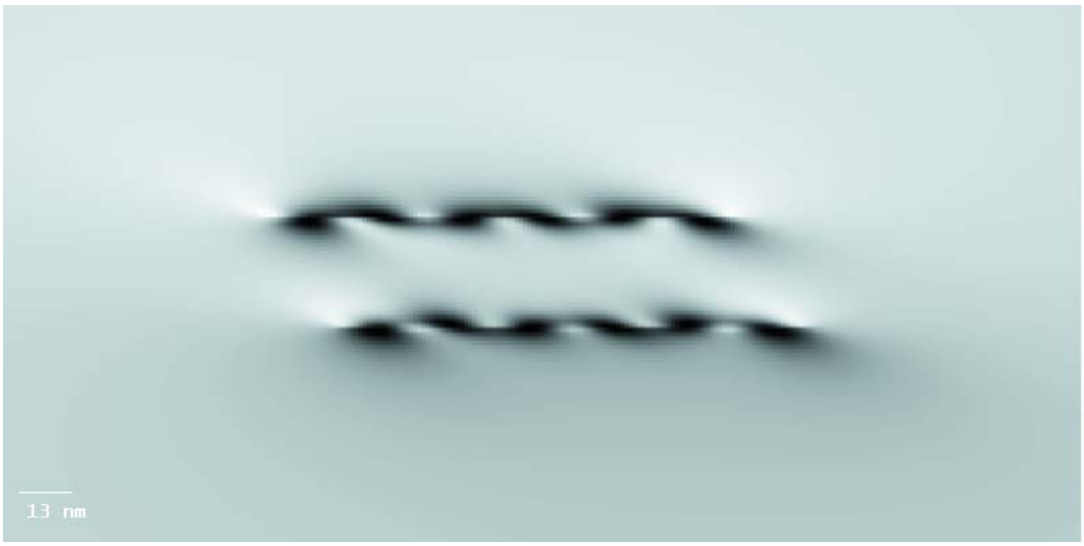

a. FePdt APB 25 g 11-1

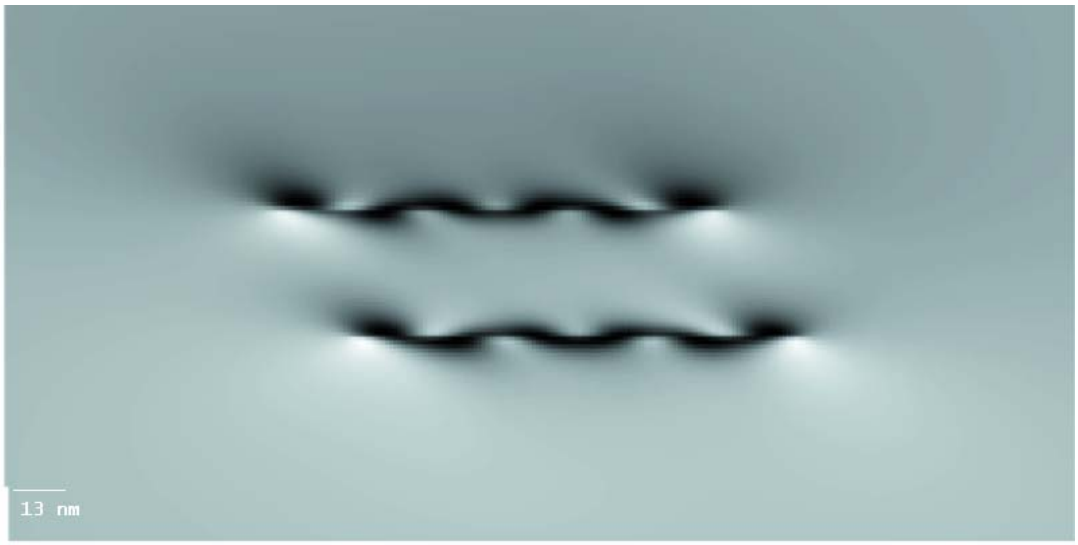

b. FePt APB 25 nm g 11-1

Figure 56 Two fold dissociated SD with APB width = 25 nm g 11-1

In figure 56, the active systematic raw is g=11-1, and the contrast changes in the opposite way of FePd and FePt. In FePd, the contrast of superpartials change from bright to dark while for FePt the contrast changes from dark to bright.

5.4.3.1.1 Π Fringes in TEM

In order to illustrate π fringes of the APB, another zone axis was chosen to use for another systematic row. The systematic row was chosen to be 110 with foil normal FN [10,-11, 0], Beam Direction BD [1,-1,0] and a dislocation direction of [1-10] screw dislocation. The translation vector R of the APB was ½[10-1]. The stacking fault contrast is expressed by 2π g.R = 2 π (110).1/2(10-1) = π.

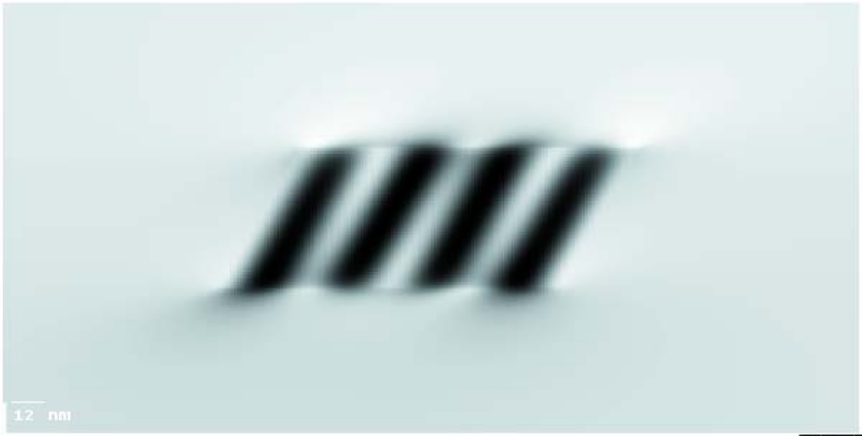

a.FePd APB 50 nm g 110

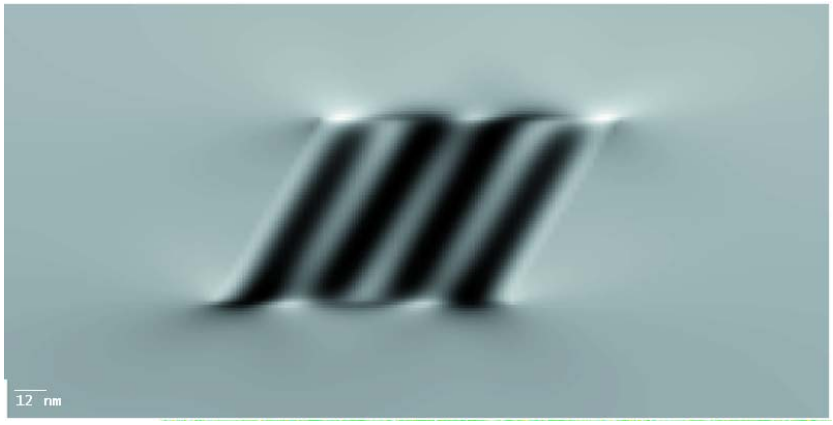

b. FePt APB 50 nm g 110

Figure 57 Π Fringes in APB with g = 110

6.4.3.2 FOUR FOLD DISSOCIATION OF THE SUPER DISLOCATION

Super dislocation can be dissociated in a four fold as follows

$$[0\bar{1}\bar{1}] \rightarrow \frac{1}{6}\left[1\,1\bar{2}\right] + SISF + \frac{1}{6}\left[\bar{1}2\bar{1}\right] + APB + \frac{1}{6}\left[1\,1\bar{2}\right] + CSF + \frac{1}{6}\left[\bar{1}2\bar{1}\right] \tag{55}$$

This dissociation has three stacking faults: SuperInterensic (extrinsic) Stacking Faults, AntiPhase Boundaries (APB) and Complex Stacking Faults.

The following images are the simulated images of the four fold dissociation in FePd and FePt. The simulated images were taken with a systematic row of g 020, beam direction [101] , Foil Normal FN [10,0,11] and Dislocation Direction in the screw direction [01-1].

For g 020, the Complex Stacking Faults (CSF) and Super IntrinsicStacking Faults (SISF) are always visible while the APB is invisible in the simulated images. The following figures show the images with varied stacking widths for SISF and fixed APB and CSF widths. Figure 59 shows the four fold dissociation of the super dislocation with 5mn as a width of the SISF and 1nm as a width of the APB and 0.5 nm as a width of the CSF. Figure 60 also shows the four fold dissociation of the super dislocation but with a different SISF width: SISF = 10 nm. Figure 61 shows the dissociation in the case of SISF = 30 nm , APB 1 nm and CSF = 0.5 nm.

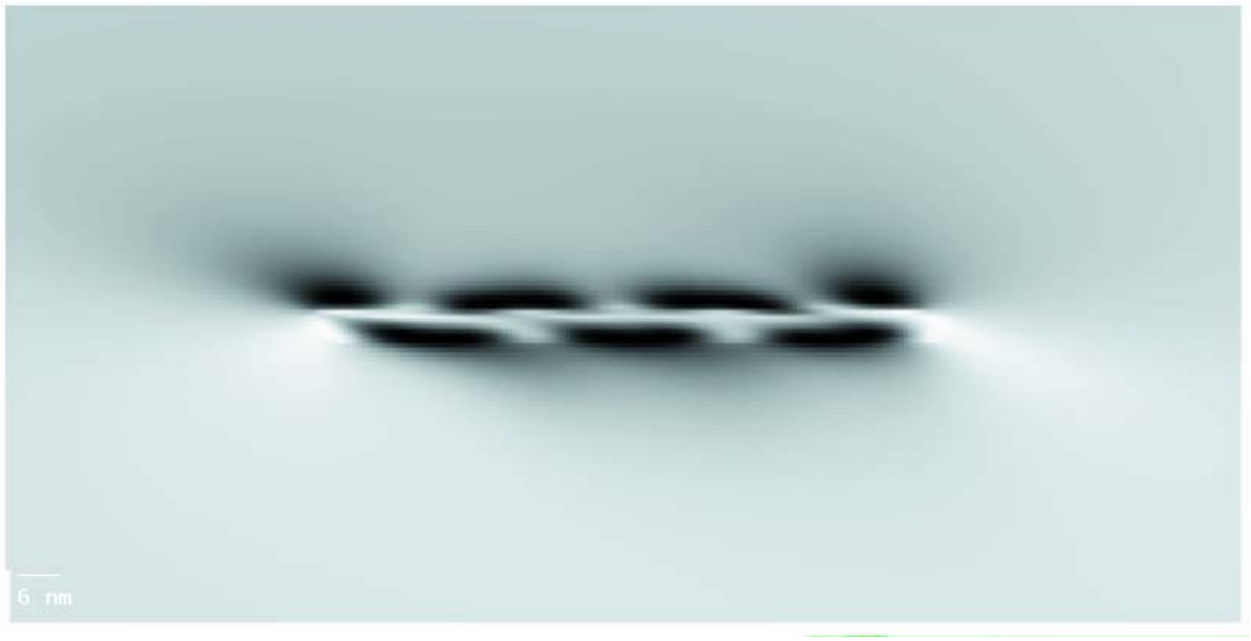

a.FePd SISF 5 , APB 1 , CSF 0.5 nm

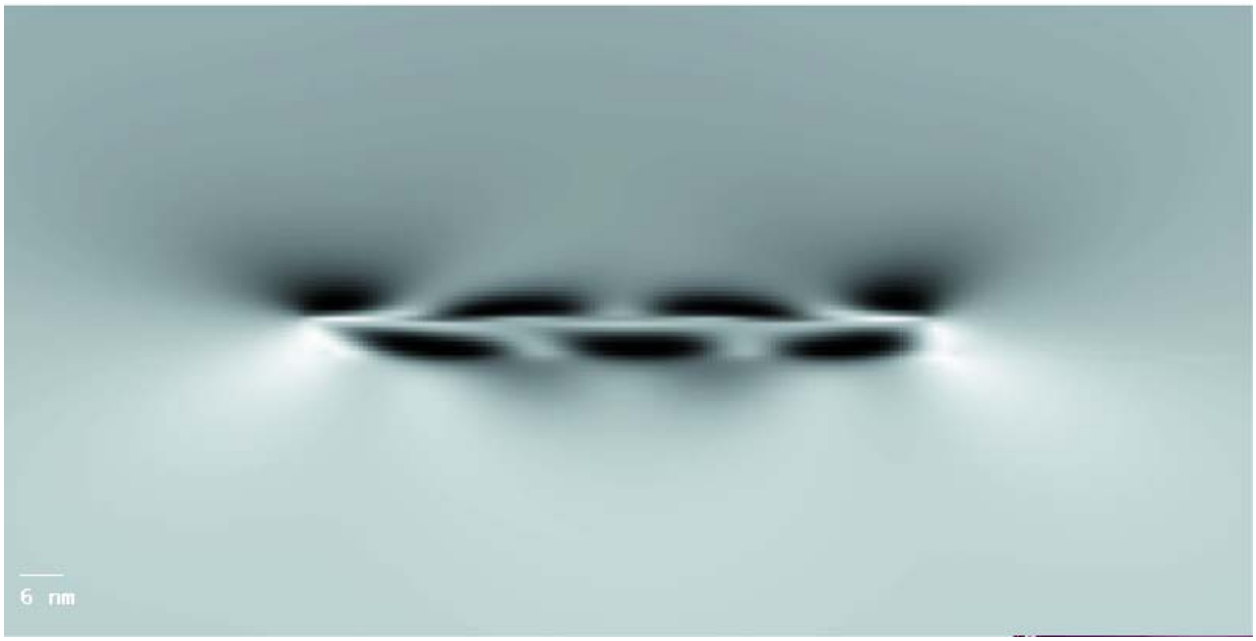

FePt SISF 5, APB 1, CSF 0.5 nm

Figure 58 Four Fold Dissociation of Super Dislocation with SISF 5 nm a. FePd , b. FePt

a.FePd SISF 10, APB 1, CSF 0.5 nm

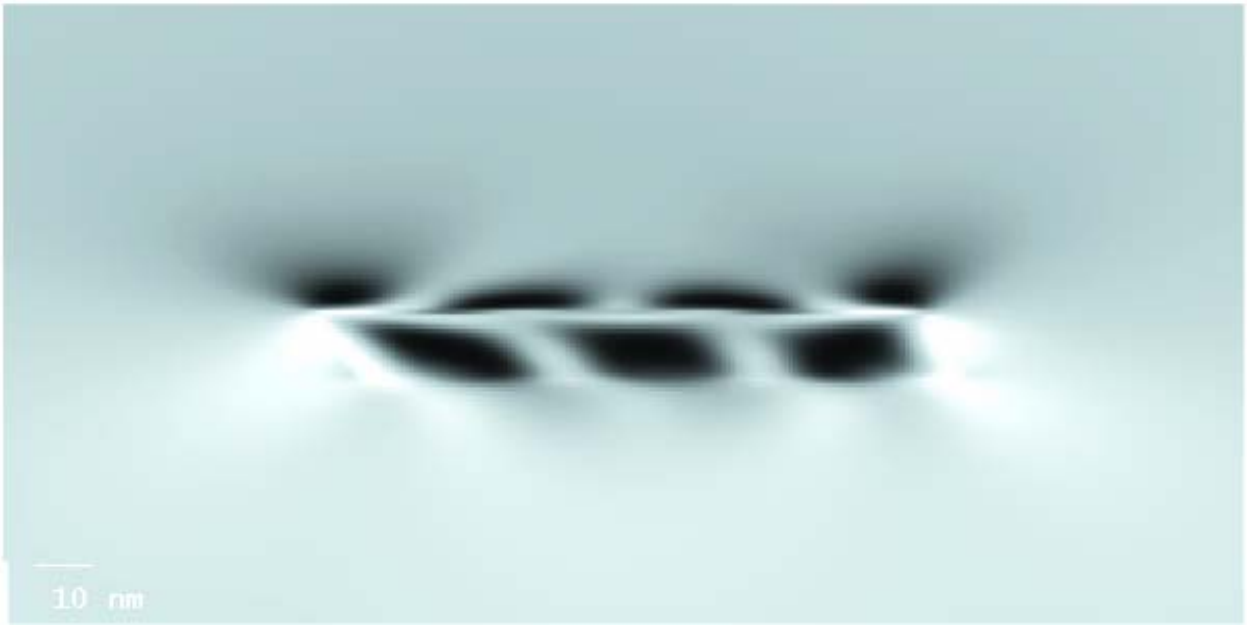

b. FePt SISF 10, APB 1, CSF 0.5 nm

Figure 59 Four Fold Dissociation of Super Dislocation with SISF 10 nm a. FePd ,b. FePt

a.FePd SISF 30, APB 1, CSF 0.5 nm

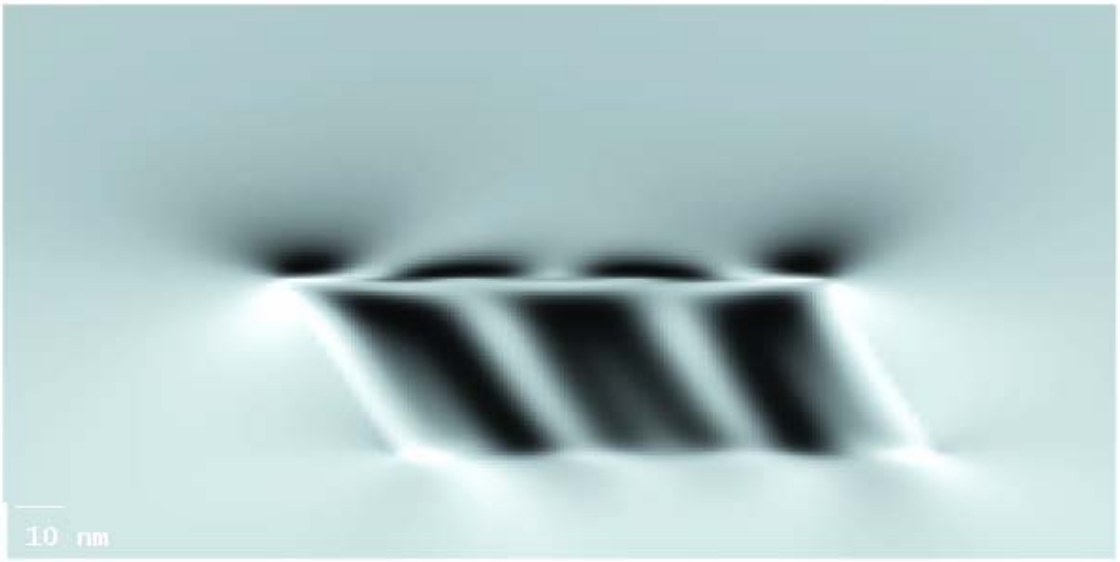

B. FePt SISF 30, APB 1, CSF 0.5 nm

Figure 60 : Four Fold Dissociation of Super Dislocation with SISF 30 nm a. FePd ,b. FePt

In figures 58, 59 and 60, the four fold dissociation of the super dislocation is illustrated using 020 as the active systematic raw. The contrast changes in the same manner in both FePd and FePt. The width of the stacking faults of SISF and CSF looks larger in FePt than FePd.

6.4.4. Weak Beam Dark Field Image Simulation

The four fold association of the superdislocation was simulated using the Cu-Four software. Figures 62-64 illustrate the weak beam dark field image simulation.

Figure 62 shows the four fold dissociation of superdislocation in WBDF with g-2g condition, where g = (020) . The center of the laue circle is (0,2.1,0).

a. FePd SISF 20 nm , APB 15 nm , CSF 5 nm

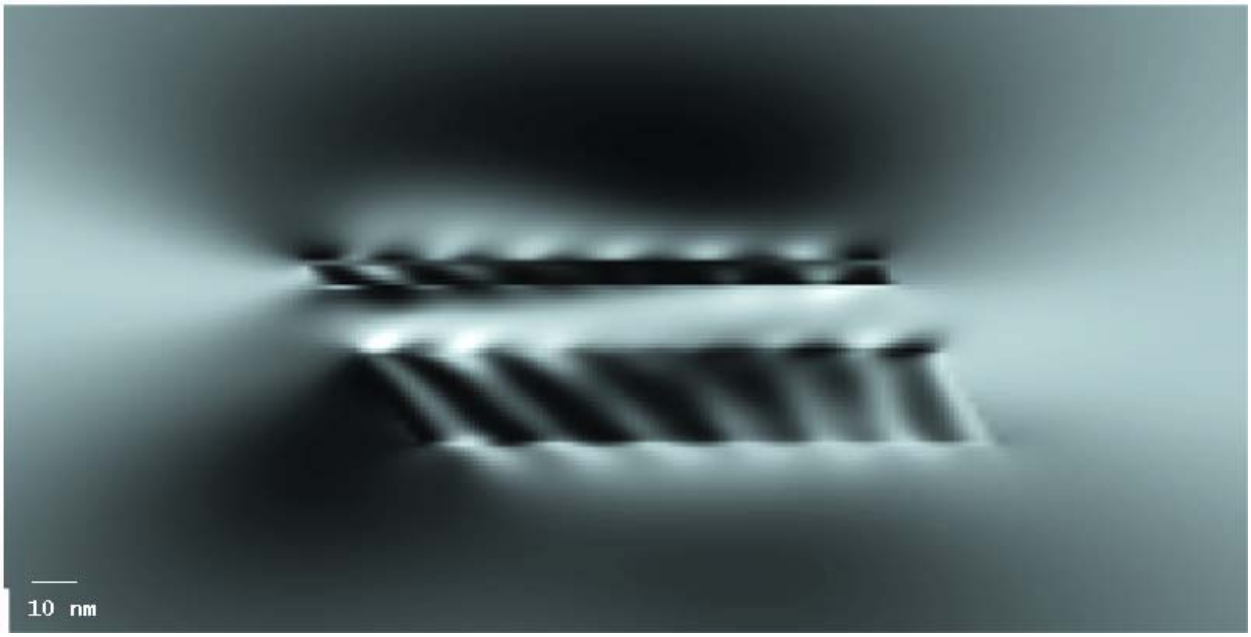

b. FePt SISF 20 nm , APB 15 nm , CSF 5 nm

Figure 61 WBDF of FePd and FePt for (g-2g) where g = (020)

Figure 62 shows the WBDF of the four fold dissociation of the super dislocation in FePd and FePt. The WBDF imaging condition is g-3g where g = (020). The center of the laue circle is (0, 3.2, 0).

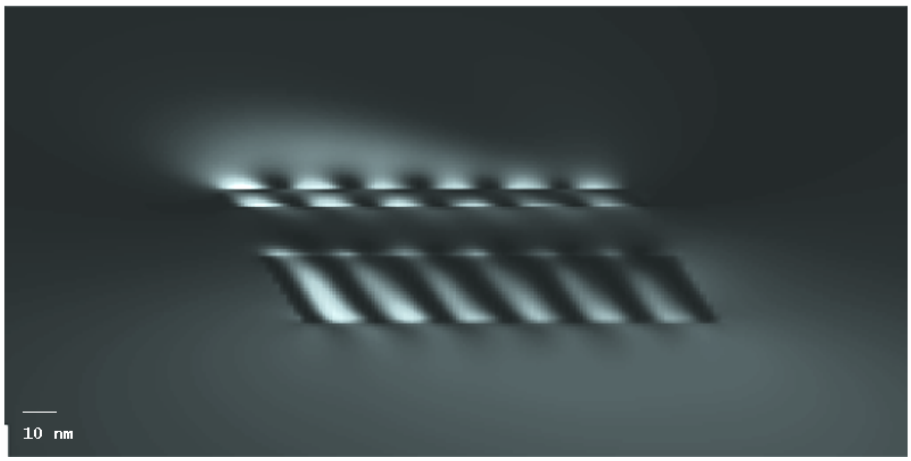

a. FePd SISF 20 nm, APB 15 nm, CSF 5 nm

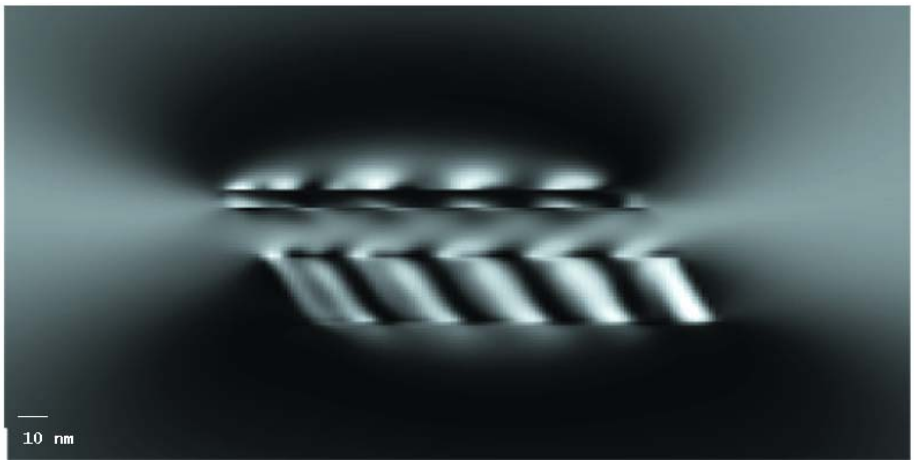

b. FePd SISF 20 nm, APB 15 nm, CSF 5 nm

Figure 62 WBDF of FePd and FePt for (g-3g) where g = (060)

Figure 63 illustrates the WBDF image simulation for two fold dissociation of superdislocation with APB width of 25 nm. The main difference between the FePd simulated image and FePt simulated image is that in FePd, the contrast of the dislocation is larger than that in the FePt case.

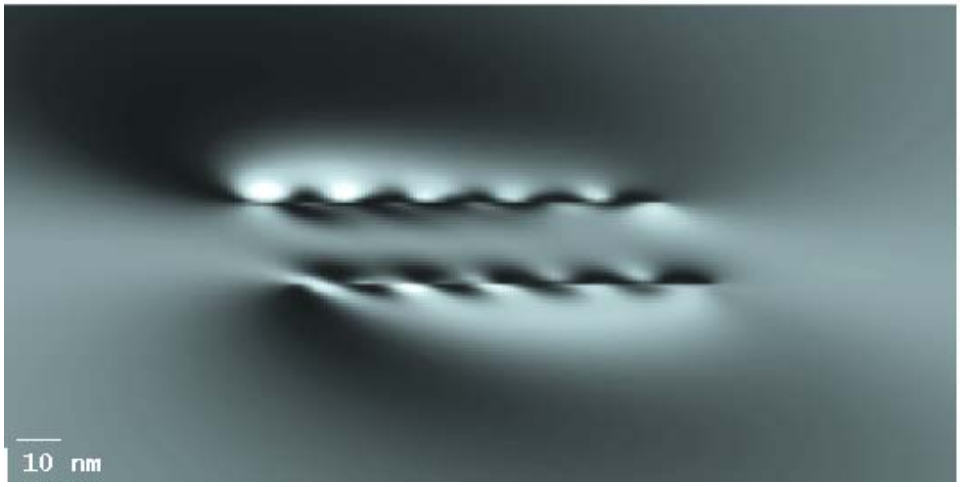

a. FePd 2 fold dissociation of SD with APB width=25 nm

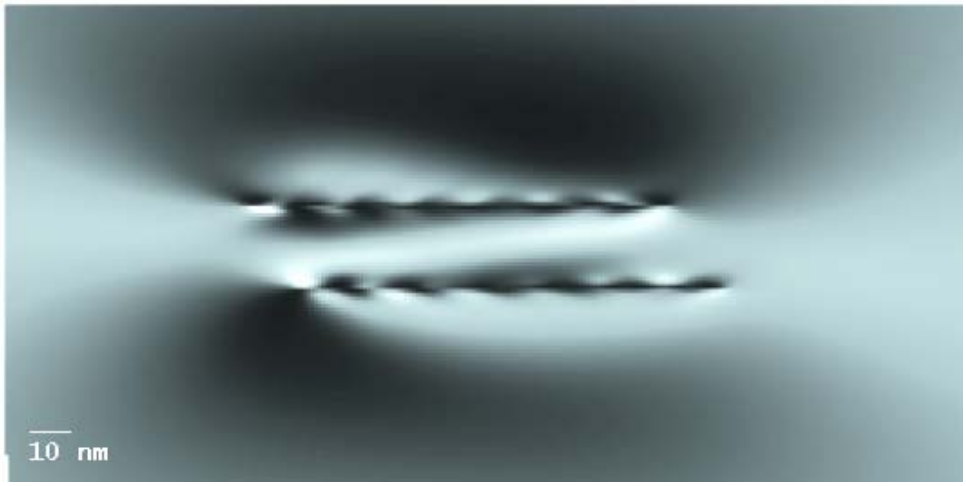

b. FePt 2 Fold Dissocaition of SD with APB width = 25 nm

Figure 63 WBDF of two fold dissociation of superdislocation with APB width =25 nm in a. FePd b.FEPt

WBDF criteria that were founded by Cockyne can be tested in order to find a good imaging condition for FePd and FePt. Cu-Four software provides the values for Geometrical deviation of sg and the extinction distance ξg. Dynamical deviation wg is given as the following equation:

$$W_g = s_g \xi_g \tag{56}$$

Table [8] shows the values for s_g ξg and w_g . When n=2, s_g has a value that is smaller than 0.2 nm^{-1}, which means criterion (a) is not satisfied . Also when n=2, w_g has a value that is greater than 5, which means criteria c is satisfied. Figure 65 shows the image simulation of the g-2g condition for FePd, which shows a reasonable contrast from the stacking faults.

Table 8 sg g and wg

N	G	S_g	ξ_g	w_g
2	040	0.061005	51.46	3.139
3	060	0.193237	107.382	20.75

It can be concluded that WBDF criteria is obeyed just for 100 KV electron microscopes and is not valid for our case with FePd.

There are some noticeable differences in the four fold dissociation of superdislocations in FePd and FePt in WBDF. These differences are in the contrast of the stacking faults fringes and the contrast of the lobes that are away from the dislocations. Differences in elastic stiffness values C_{ij} should result in different contrasts in dislocation TEM images. It seems that differences are more pronounced in WBDF than in BF.

7. 0 CONCLUSIONS AND OUTLOOK

7.1 CONCLUSIONS

Based on the results and analysis of this study, the following conclusions can be drawn:

1. FePd single crystals can be grown.

2. The elastic constants of FePd were measured and they were found to be the reverse of those of TiAl regarding the tetragonal anisotropy which is to be expected since the c/a ratios in both materials are the opposite of each other.

3. The elastic constants of FePt are the reverse of those of FePd. This is unexpected since both materials have an L10 structure with c/a <1.

4. FePt elastic constants vary in a way similar to those for TiAl .

5. The hierarchy of Young's Modulus as a function of direction [uvw] in FePd is:

$E_{[111]}>E_{[110]}>E_{[011]}>E_{[001]}>E_{[100]}$,

which is different than that of TiAl:

$E_{[111]}>E_{[011]}>E_{[110]}>E_{[100]}>E[001]$

6. The hierarchy of Shear Modulus in (111) as a function of direction of FePd is

G(111)[-1-12]>G(111)[-101]>G(111)[-110],

which means that it is easier to shear along the direction [-110] and increasingly more difficult as the shear direction tends towards [-1-12]. This might imply for FePd that octahedral OD glide is favored over glide by DS and, in particular, a full perfect TD. It must be noticed that the overanisotropy of the shear modulus in the (111) plane is not very large.

7. Elastic Moduli of polycrystalline FePd were calculated using Hill's averages. The Poisson's ratio is 0.33, which compares well with the Poisson's ratio for some similarly elastically anisotropic and ductile FCC metals, e.g., Al(0.34),Cu (0.34), while Poisson's ratio for TiAl is 0.22, which is much smaller than that of FePd. This would appear to be in agreement with the apparently better ductility of FePd as compared with single phase TiAl.

8. A compression test was performed for an FePd single crystal, and although the experimental value of Young's Modulus was not determined, the values of the critical shear stress for both TD and SD were determined.

9. The compression test confirmed that in FePd, Schmid's law is obeyed since theoretical active slip systems were experimentally observed via Optical Microscope and SEM.

10. The TEM study for the single crystal sample confirmed the activity of just Superdislcoations and Twin Dislocations in the active slip systems.

11. TEM image simulation was established for FePd dislocations. TEM image simulations of dissociated ordinary dislocation, dissociated twin dislocations and dissociated superdislocations were illustrated in this study.

12. A Weak Beam Dark Field TEM image simulation was also established for FePd, as well as imaging conditions.

7.2 OUTLOOK:

To develop the level of understanding of the YSA in FePd, interested researchers should perform some experiments that will provide an explanation and enrich the field with the required information.

Some of the recommended experiments are:

1- To develop a controlled microstructure non-polytwinned FePd sample with large grains.

2- To do a plastic deformation test at different temperatures and try to obtain the yield stress values at different temperatures.

3- To do a TEM analysis to find the active dislocation systems and try to find out if there is non-plannar configuration for the dislocations (i.e any type of locking).

4- To use the developed simulated image to compare with experimental images and to find the stacking faults energies of the different stacking faults.

APPENDIX A: ELECTROMECHANICAL INSTRON UNIVERSAL TESTING MACHINE

To ensure the accuracy of the electromechanical Instron Universal testing machine, we performed some compression tests using Al 3003-H14 samples.

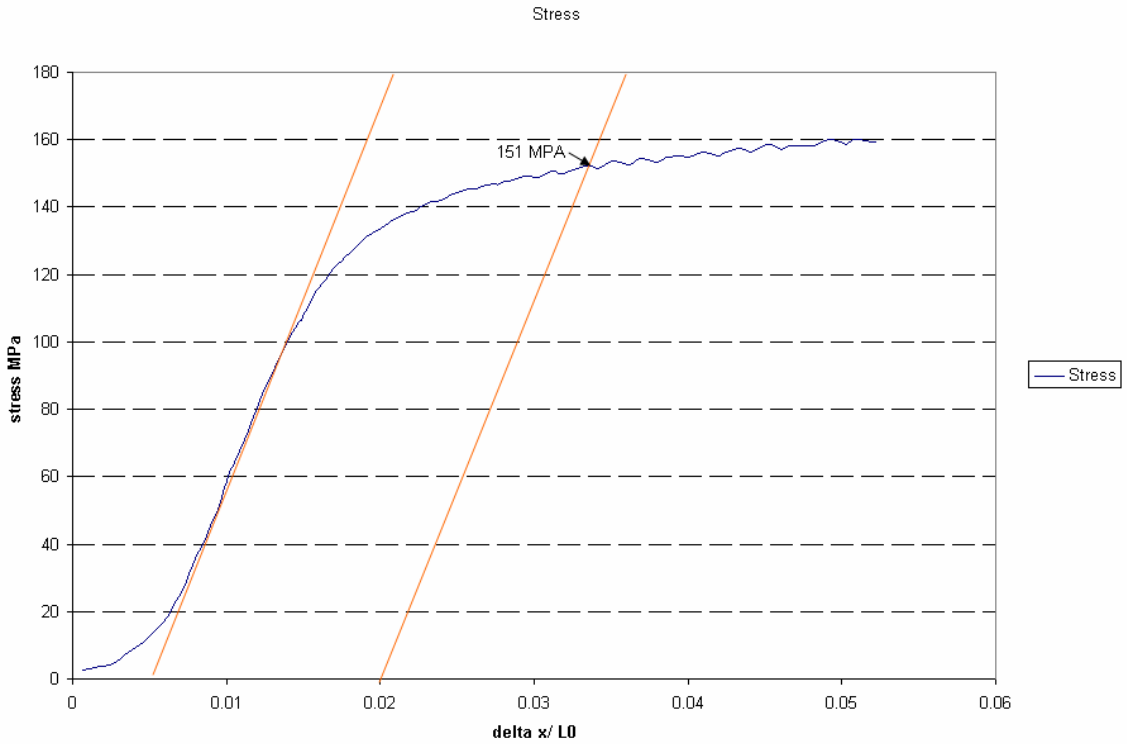

Figure 1

Figure 1 shows the stress vs. delta x/L0 curve. Using the graph, the yield strength was measured to be 151 MPa. Actual yield strength was reported to be 152 MPa[101]. This result shows a good agreement of the actual and measured yield strength.

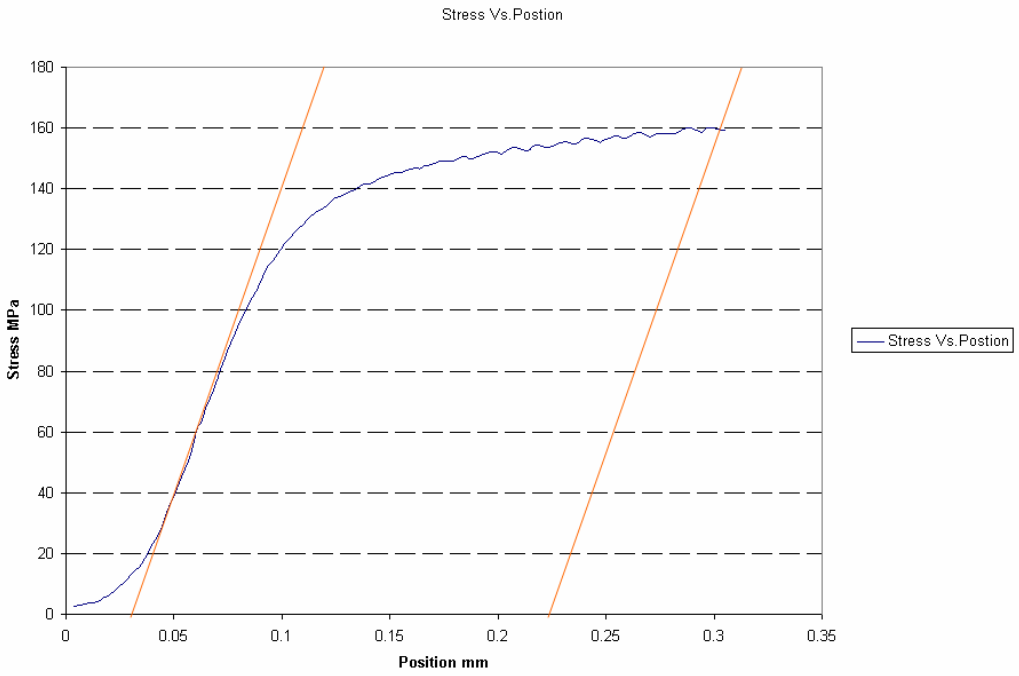

Figure 2

Figure 2 shows the stress vs. position curve for Al-3003-H14. The curve shows that the change in the position is about 0.19 mm. The actual measurement via micrometers shows that delta L =0.21 mm.

From Figure 1, the elastic modulus is calculated to be 11.48 GPa. The elastic modulus value for Al 3003-H14 alloy is reported to be 68.9 GPa. There is a difference between the elastic constant of the Al Alloy and the measured elastic modulus. This is because in our compression test we are measuring the elastic modulus of the whole system, as shown in Figure 25 in the text above.

The two figures above show us the accuracy of the electromechanical Instron Universal testing machine just for the values of the Yield Stress and for the position displacement.

BIBLIOGRAPHY

[1] Rao M. ,Soffa W. (1997) , Scripta Materialia, Vol 36, No.7, 1997, pp. 735-740

[2] Yu. A., Volkov, Greenberg B. A. , etc, (2003) The physics of metals and matellography, 95, No. 4, 2003, pp 355-360.

[3] Caillard D. , Couret A. , in, F.R.N. Nabarro, M.S. Duesberry (Eds.) (1996) Dislocations in Solids, Vol. 10, Elsevier, Amsterdam, 1996, p 69 chapter 50.

[4] Caillard D. , (2001), Mater. Sci. Eng A. 319-321 74-83

[5] Nortman A. , Neuhauser H. ,(1997) Mater. Sci. Eng. A234-236 548.

[6] Kashyap B. P. , Taggart K. , Tangri K. , (1988) Phil. Mag. A57 pg.97.

[7] Regnier P.,. Dupouy J. M , (1970) Phys. Stat. Sol. 39 179

[8] Takasugi T., Tsurisaki K. , Izumi O. , Ono S. , (1990) Phil. Mag. A61 785.

[9] Clement N., Molenat G. , Caillard D. , (1991) Phil. Mag. A64 697

[10] Kuramoto E. , Pope D.P., (1991) Phil. Mag. A64 675.

[11] Pope D.P. , and Liu C.T., (1989) "Superalloys, Supercomposites, and Superceramics," eds. Tien et al., New York, NY: Academic Press.

[12] Pope D.P. , and Liu C.T., (1989) "Superalloys, Supercomposites, and Superceramics," eds. Tien et al., New York, NY: Academic Press.

[13] Paidar V., Yamaguchi M., Pope, and Vitek , (1982), Phil Mag , 45 pg. 883.

[14] Crimp M., (1989)Phil Mag. Lett, 60 , 45-50.

[15] Sun Y.Q. and Hazzledine P., (1992) "Ordered Intermetallics- Physical Metallurgy and Mechanical Behavior,' NATO ASI Series, Vol. 213, pg.177-196 .

[16] Mishima Y., Ochiai S. , Yodagawa Y., (1986)Trans. JIM, 27, pg. 41-50.

[17] Yoo M. H., (1986)Scr. Metall., 20, pg. 915.

[18] Takeuchi S. and Kuramoto E., (1973), Acta Metall, 21 ,pg. 415.

[19] Lall C., Chin S. , and Pope D.,(1979) Metall. Trans., 10A pg.1323.

[20] Paidar V., Pope D.B., and Vitek V., (1984), Acta Metall. 32 pg.435.

[21] Yoo M.H. , Scr. Metall. (1986), 20 ,pg915.

[22] Bumps E.S., Kessler H and Hansen M, Transactions AIME (1952) 194, 609.

[23] Wiezorek J.M.K., C.J. Humphreys. (1995) Scr. Metall. Mater. 33 pg. 451.

[24] Zupan M, Hemker K, (2003)Acta Mater. , 51,pg. 6277-90.

[25] Greenburgh BA, Antonova OV, etc. (1991)Acta Metall Mater , 39: pg 233-42.

[26] Woodward C, MacLaren JM, Dimiduk DM. In :Baaker I , etc ,(1993) High-temperature ordered intermetallic alloys, V228, MRS, , P335-42.

[27] Woodward C., MacLaren (1996) JM. Philos Mag, A, 74, pg. 237-357.

[28] Hemker KJ, Viguier B, Mills MJ, (1993),Mater Sci Eng A, 164, pg 391-4

[29] Wang Z-M, Wie C, Feng Q, etc, (1998) Intermetallics,6, pg. 211-6

[30] Bonnevielle J, Escaig B. (1979) Acta Metall.,27, pg. 1477.

[31] Crimp M., (1989)Phil Mag. Lett, 60 , 45-50.

[32] Bumps E.S., Kessler H and Hansen M, Transactions AIME (1952) 194, 609.

[33] Yoo M, Fu C, (1998) Metall Mater Tras A; 29,pg. 49-63

[34]Zupan M, Hemker K, (2003)Acta Mater. , 51,pg. 6277-90.

[35] Thompson N., (1953)Proc. Phys. Soc. 66B:481

[36]Greenburgh BA, Antonova OV, etc. (1991)Acta Metall Mater , 39: pg 233-42.

[37] Greenburgh BA, Antonova OV, etc. (1991)Acta Metall Mater , 39: pg 233-42.

[38] Gregori F, Veyssiere P. , (2001) Mater Sci Eng A, 309-310,87-91

[39]Zupan M, Hemker K, (2003)Acta Mater. , 51,pg. 6277-90.

[40] Umakoshi Y, Pope DP, Vietick V, (1984) Acta Metall,32,449-56

[41]Greenburgh BA, Antonova OV, etc. (1991)Acta Metall Mater , 39: pg 233-42.

[42] GAo Y.D. ,. Whang S.H, (1995) Matall. Mater. Sci. Trans. A, 26A(1).

[43] Yi-Qun Gao, Zhong-Min Wang etc, (1995) Mat. Sci. Engi A192/19353-58

[44]Yi-Qun Gao, Zhong-Min Wang etc, (1995) Mat. Sci. Engi A192/19353-58

[45]Yi-Qun Gao, Zhong-Min Wang etc, (1995) Mat. Sci. Engi A192/19353-58

[46] Hansson, B., Barnes, R. S. , (1964), Acta. Matall., Vol 12, pp. 315

[47] Magat L. M., Yermolenko A. S.,. Ivanova, etc., Fi z. (1968)Metal. Metalloved., Vol. 26, pp 511-516

[48] Bumps E, . Kessler D. and. Hansen M, (1952),Transaction AIME, 194, p 609.

[49] Marinkowski M. J., ed. (1963),Electron Microscopy and Strength of Crystals, G. Thomas Washburn, J. Interscience publisher, p333.

[50] Marcinkowski M., Brown N. , Fisher R, 1961,, Acta. Mat., Vo. 9, pp 129

[51] Wiezorek J. M. K., Xu H., (2004) Acta Mat. 52 ,pg 395-403

[52] Wiezorek, (2003) Intermetallics vol 11, p9.

[53]Wiezorek J. M. K., Xu H., (2004) Acta Mat. 52 ,pg 395-403

[54] Ye M.,Yermakov,. Maykov, (1990) Phys. Met. Metall. 69 pg.198.

[55] Tanaka K. ,Ichitsubo T., Koiwa M., (2001) Materials Science and Engineering A 312, pg 118-127

[56]Tanaka K. ,Ichitsubo T., Koiwa M., (2001) Materials Science and Engineering A 312, pg 118-127

[57] Klemmer T, Soffa W. , (1994) Solid-Solid phase transformations (TMS, Warrendale)p. 969

[58]Ye M.,Yermakov,. Maykov, (1990) Phys. Met. Metall. 69 pg.198.

[59] Deshpande A, Blachere J, Wiezorek JMK (2006) Scr. Mater. 54 p. 955.

[60] Klemmer T, Hoydick D, Okumura H, Zhang B, Soffa W(1995): Scr. Metall. Mater. ,33, p. 1793

[61] Ichitsubo T, Nakano M, Tanaka K, Koiwa M. (1998) Mater Trans JIM, ,39, p 24.

[62] Ichitubo T, Tanaka K. (2004) J Appl Phys, , 96, p 6220.

[63] Zhang B, Lelovic M, Soffa WA. (1991) Scripta Metall Mater, 25, p 1577

[64] Ichitsubo T, Tanaka K. (2004) J Appl Phys, , 96, p 6220.

[65] A. Kelly and N.H. MacMillan, (1986) Strong Solids, 3rd ed.,Oxford University Press, Oxford, ,p 395.

[66] Y, Schwarz RB, Migliori A, Whang SH. (1995)J. Mater. Res;10:1187.

[67] Umakoshi Y, Yamaguchi M. Progr. Mat. Sci. 1190;34:1.

[68] B.A. Auld, (1973)Acoustic Fields and Waves in Solids (John iley&Sons, New York, Vol. 1 Chap 3.

[69] Hill R.(1952) Proc Phys Soc Lond, 350.

[70] Simmons G. and Wang H., (1971). Single Crystal Elastic Constants and Calculated Aggregated Properties: A Handbook, 2nd ed. (The MIT Press, Cambridge , MA,

[71] Schreiber E., Anderson O.L. and Soga N., (1973), in Elastic Constant and Their Measurement (McGraw-Hill, New York, p 29-31.

[72] P.B. Hirsch, A. Howie, R. B. Nicholson, D.W. Pashley and M. J. Whelan, (1977) Electron Microscopy of Thin Crystals, 2nd ed., Malabar, FL:Krieger Publishing)

[73] A. Howie and M. J. Whelan, (1961) Proc. Roy. Soc. A 263, 217.

[74] A. K. Head, P. Humble, L. M. Clarerough, A. J. Morton and C. T. Forwood, (1973) Computed Electron Micrographs and Defect Identification, Defect in Crystalline Solids 7, (Amsterdam : North Holland.)

[75] M.J. Whelan and A. Howie, (1957) Phil. Mag. 2, 1303.

[76] R. Schaublin, P. Stadelmann, (1993) ' A method for simulating electron microscope dislocation images' , Materials Science and Engineering, A 164 373-378.

[77] A. K. Head, P. Humble, L. M. Clarerough, A. J. Morton and C. T. Forwood, (1973) Computed Electron Micrographs and Defect Identification, Defect in Crystalline Solids 7, (Amsterdam : North Holland.)

[78] M.J. Whelan and A. Howie, (1957) Phil. Mag. 2, 1303

[79] B. Hirsch, A. Howie, R.B. Nicholson, D.W. Pashley and M. J. Whelan, (1969) ' Electron Microscopy of Thin Crystals' , London,.

[80] B. Fultz, J.M. Howe,(2001) Transmission Electron Microscopy and Diffractometry of Materials, Springer-Verlag Berline Heidelberg. p405

[81]Greenburgh BA, Antonova OV, etc. (1991)Acta Metall Mater , 39: pg 233-42.

[82] D.J.H. Cockayne, (1973) J. of Microscopy 98 , pt. 2, 116.

[83] Villars P, Calvert LD, (1991)Pearson's handbook for crystallographic data for intermetallic phases, 2nd ed. Metal Park(OH), ASM.

[84] Shima H., Oikawa K.,etc, (2004) Physical Review B, 70 ,224408-1.

[85] Shima H., Oikawa K.,etc,(2004) Physical Review B, 70, 224408-1.

[86]Ye M.,Yermakov,. Maykov, (1990) Phys. Met. Metall. 69 pg.198.

[87] Zhang B, Lelovic M, Soffa WA. (1991) Scripta Metall Mater, 25, p 1577

[88] Zhang B, Lelovic M, Soffa WA. (1991) Scripta Metall Mater, 25, p 1577

[89] Kim Jae-Song, Koo Yang-Mo Koo, Byeong-Joo Lee, (2006)Journal of Applied Physics 99,053906

[90] He Y, Schwarz RB, Darling T.etc, (1997), Elastic constants and thermal expansion of single crystal TiAl from 300 to 750 K, Materials Science and Engineering , A239-240, 157-163

[91] Tanaka K, Ichitsubo T, Inui H, Yamaguchi M, Koiwa M. , (1998) Mater Trans JIM;39:24.

[92]A. K. Head, P. Humble, L. M. Clarerough, A. J. Morton and C. T. Forwood, (1973) Computed Electron Micrographs and Defect Identification, Defect in Crystalline Solids 7, (Amsterdam : North Holland.)

[93] He Y, Schwarz RB, Darling T.etc, (1997), Elastic constants and thermal expansion of single crystal TiAl from 300 to 750 K, Materials Science and Engineering , A239-240, 157-163

[94] He Y, Schwarz RB, Miigliori A, Whang SH.(1995) J Mater Res;10:1187.

[95]Ichitubo T, Tanaka K. (2004) J Appl Phys, , 96, p 6220

[96] Ichitubo T, Tanaka K. (2004) J Appl Phys, , 96, p 6220

[97] Kim Jae-Song, Koo Yang-Mo Koo, Byeong-Joo Lee, (2006)Journal of Applied Physics 99,053906

[98] He Y, Schwarz RB, Migliori A, Whang SH, (1995)J Mater Res, p 283.

[99]Tanaka K, Ichitsubo T, Inui H, Yamaguchi M, Koiwa M. , (1998) Mater Trans JIM;39:24.

[100] He Y, Schwarz RB, Darling T.etc, (1997), Elastic constants and thermal expansion of single crystal TiAl from 300 to 750 K, Materials Science and Engineering , A239-240, 157-163

101 http://www.matweb.com/search/SpecificMaterial.asp?bassnum=MA3003AH14